Mastering Beam Losses on Small Gap Vacuum Chambers in Synchrotron Light Sources

Application to the European Synchrotron Radiation Facility, ESRF

von

Udo Weinrich

Dem Fachbereich Physik

der Universität Dortmund

zur Erlangung des akademischen Grades

Doktor der Naturwissenschaften (Dr.rer.nat.)

Vorgelegte Dissertation

Grenoble, Dezember 1999

Abstract

To increase at the ESRF the brilliance at high photon energies, Insertion Devices with shorter periods were installed during the last years. Accordingly smaller vertical gap vacuum chambers were installed in the straight sections. The vacuum chamber gap reduction resulted in significant electron losses on the chamber walls - therefore creating radiation problems for the corresponding beam lines and on the roof of the tunnel. After the installation of a beam loss detection system a study of the beam loss origins was carried out. Following this several modifications were applied to the machine operation to reduce the overall losses in the storage ring. Additionally the use of scrapers to intercept the electrons was investigated and optimised. Based on the experience gained an upgrade of the beam loss detection system was done. The results presented in this thesis demonstrate how the ESRF radiation levels were reduced to an acceptable level, even for the smallest gap chambers.

Zusammenfassung

Zur Erhöhung der Brillianz bei hohen Photonenergien wurden an der ESRF während der letzten Jahre Insertion Devices mit kürzeren Perioden genutzt. Im Zuge dessen wurden Vakuumkammern mit kleinerem vertikalen Kammerquerschnitt in die geraden Strecken eingebaut. Die Verminderung des Kammerquerschnittes führte zu erheblichen Elektronenverlusten auf der Kammerwand mit Strahlungsproblemen an der jeweiligen Beamline und auf dem Tunneldach. Nach dem Einbau von Strahlverlustmonitoren wurden die Ursachen der Elektronenverluste untersucht. Daraufhin wurden mehrere Änderungen an dem Speicherringbetrieb vorgenommen, um die Anzahl der Elektronenverluste zu verringern. Zusätzlich wurde die Nutzung von Scrapern zum Auffangen der Elektronen untersucht und optimiert. Aufgrund der gesammelten Erfahrung wurde eine Verbesserung an den Strahlverlustmonitoren durchgeführt. Die in der Dissertation vorgestellten Ergebnisse belegen, daß mit Hilfe der an der ESRF eingeleiteten Maßnahmen zur Verminderung der Elektronenverluste die Strahlungswerte selbst für die Kammern mit dem kleinsten Querschnitt auf ein akzeptables Niveau gesenkt werden konnten.

ABSTRACT 2

ZUSAMMENFASSUNG 2

1. INTRODUCTION 1

2. THE ESRF STORAGE RING 4

2.1 Machine Lattice and Optics 4

2.2 Brilliance considerations 9

2.3 History of Small Gap Vacuum Vessels 10

2.4 Transverse Acceptances 14

2.5 Injection process and horizontal Acceptances 21

2.6 User Service Mode 22

2.7 Radio Frequency and longitudinal beam parameter 25

2.8 Machine Dedicated Time 29

2.9 Radiation Considerations 31

2.10 Summary 32

3. ELECTRON LOSS MECHANISMS 33

3.1 Injection Losses 33

3.2 Lifetime limiting processes 35

3.3 Energy acceptance 48

3.4 Quantification of Losses 58

4. ELECTRON LOSS POSITIONS 61

4.1 General considerations 61

4.2 Phase space scraping of a single vacuum chamber 63

4.3 Loss positions for the different effects 76

5. RADIATION CREATION AND DETECTION 83

5.1 Interactions of electrons with the chamber material 83

5.2 Changes of electron energy and trajectory....90
5.3 Radiation Detection....97
6. BEAM LOSS REDUCTION AND SCRAPER USE....106
6.1 Actions taken to reduce the total amount of beam losses....106
6.2 General scraper strategy....107
6.3 Scraper solutions for different loss mechanisms....110
6.4 Radiation considerations and optimum scraper location....116
6.5 General scraper solution and specification for the ESRF....118
7. CONCLUSION AND OUTLOOK....121
7.1 Conclusion....121
7.2 Outlook....122

1. Introduction

Beam losses in particle accelerators are a long-standing issue. They are important to master for many reasons:

- In linear accelerators to achieve a high transfer efficiency
- In storage rings to achieve a high lifetime and injection efficiency
- In accelerators which use superconducting magnets to avoid quenching
- In all accelerators to limit the radiation damage to material
- In all accelerators to limit the radiation exposure of the personnel
- In some accelerators to limit the radiation background on the experiment

Proton, antiproton or heavy-ion accelerators generally use superconducting magnets. Protection measures against beam losses are therefore used at HERA and TEVATRON. They are also mandatory for the LHC[1]. Quenching due to beam losses might also become a problem for superconducting Insertion Devices in synchrotron light sources especially in the case of small vertical gaps [2].

Radiation problems are common to all particle accelerators. They generally lead for personnel safety reasons to a heavy shielding of the accelerator and forbidden access during the accelerator operation. Apart from this the beam losses create an activation of the material. Radiation problems are also the main motivation for the beam loss studies at the ESRF.

Figure 1-1 ESRF overview

Motivation and scope of the thesis

The **European Synchrotron Radiation Facility (ESRF)** was the first third generation high energy synchrotron radiation source and started operation in 94. The synchrotron light production takes place in more than fifty Insertion Devices distributed over 27 straight sections in a 6 GeV storage ring.

The photon beam brilliance was steadily increased at the ESRF during the last years. This was partly achieved by using smaller period and smaller gap Insertion Devices. To achieve this smaller vertical aperture vacuum vessels had to be installed or in-vacuum undulators to be used. The tendency to go to smaller gaps is now common to all modern synchrotron light sources [3].

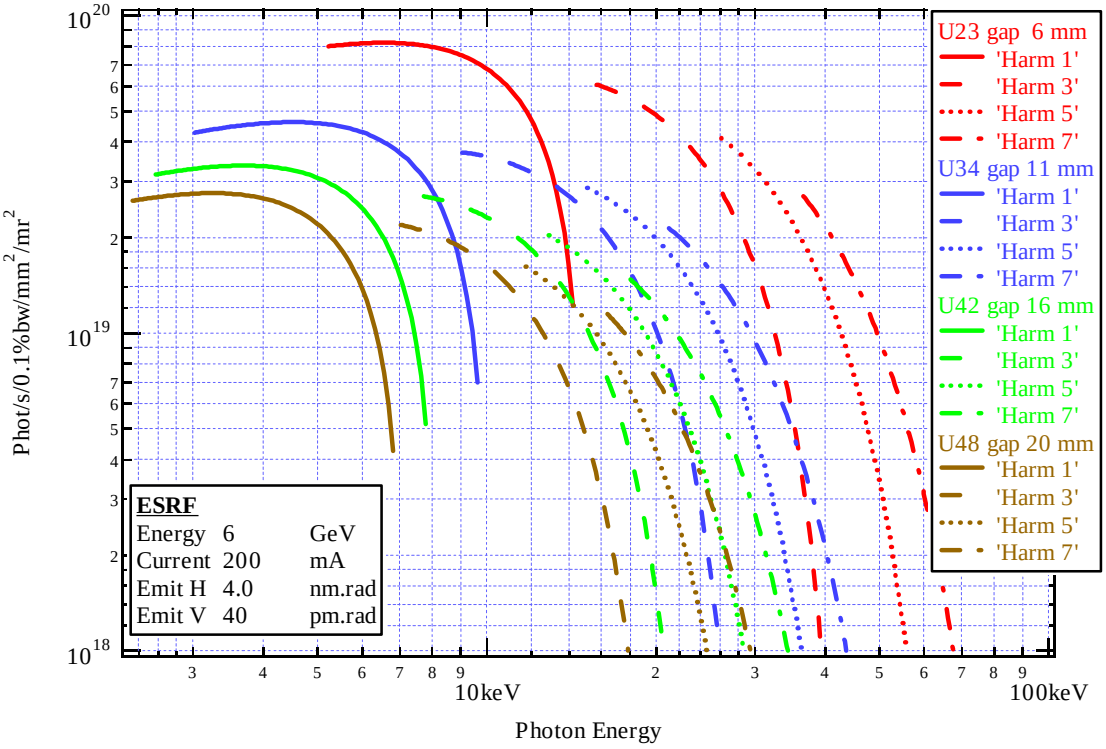

Figure 1-2 Brilliance increase due to smaller period and gap Insertion Devices

Figure 1-2 shows the brilliance from one Insertion Device situated in a low beta straight section. Four different Insertion Devices which represent the evolution towards smaller Insertion Device periods and gaps over the last years at the ESRF are shown. Between an U48 (undulator period 48 mm) at 20 mm and an U23 (undulator period 23 mm) at 6 mm there is a significant brilliance gain especially at higher photons energies. This gain is about a factor 4 at 10 keV and reaches a factor 30 at 30 keV. Looking to the photon energy one can say that the use of undulators instead of wigglers was increased from 30 keV to 70 keV.

The ESRF was the first 3rd generation high energy synchrotron light source, which operated with small gap insertion devices. Following the installation of some smaller gap vacuum vessels in 1995 unusually high radiation levels were measured in the experimental hutch and outside the optics hutch of the corresponding beam line. Additionally the vacuum vessels were found activated.

The thesis work consists in the analysis of the origin of the radiation as well as in the development of adequate counter actions.

How this thesis is organised

In the preparatory chapter 2 the ESRF storage ring is presented. The description is focussed on the main parameter, which are essential for the understanding of the beam loss problem. The ESRF beam parameter and the machine optic are presented first. The motivation for and the history of the small gap Insertion Devices are described afterwards. The way the ESRF is operated will then be shown before finally the radiation protection at the ESRF is presented and discussed.

Chapter 3 is used to present the different beam loss mechanisms. The well-known lifetime limiting effects are specified for the ESRF situation. After that the energy acceptance limiting factors at the ESRF storage ring are discussed. Beam losses, which are linked to the ESRF operation, are shown before the chapter finishes with a quantification of the different beam loss origins.

The link between the beam loss origin and the final collision point of the electron with the vacuum chamber is established in the first part of chapter 4. The interception of electrons by a vacuum chamber as a function of the machine optic will be investigated also.

Then the interaction of the electrons with the vacuum chamber material and the scrapers is discussed in chapter 5. The secondary losses following incident scattering on the chamber wall are demonstrated. The chapter finishes with a presentation of the different beam loss detection systems used.

The different counter actions, which lead to a reduction of beam losses, are presented in chapter 6. These are changes in the machine operation, which were implemented following the beam loss studies. The benefits of the beam loss optimised machine optic are discussed as well as the different upgrades of the refill procedures and the injection limitations during Machine Dedicated Time (MDT). The second part of the chapter is dedicated to the use of scrapers. It is shown how these devices can be used in general to intercept electrons before they hit a vacuum chamber wall for the different beam loss origins. The optimum scraper locations are discussed afterwards. Finally the successful use at the ESRF is demonstrated.

In Chapter 7 a conclusion of the work is presented. This is followed by an outlook to future development. The case of a scaling to lower electron energies, which is important for future light sources, is discussed. Additionally the problems arising from going further down in vacuum chamber gap are presented.

2. The ESRF storage ring

2.1 Machine Lattice and Optics

The ESRF storage ring consists of 32 cells and has a length of 844 m. Most cells are reserved for synchrotron radiation creation. In each cell *n* there is place for one beamline (ID*n*) taking beam from the insertion devices in the straight section and one beam line (D*n*) taking synchrotron radiation from the second dipole of the cell.
In Figure 2-1 an overview of the ESRF cells and the vacuum chamber installation in July 1999 is given.

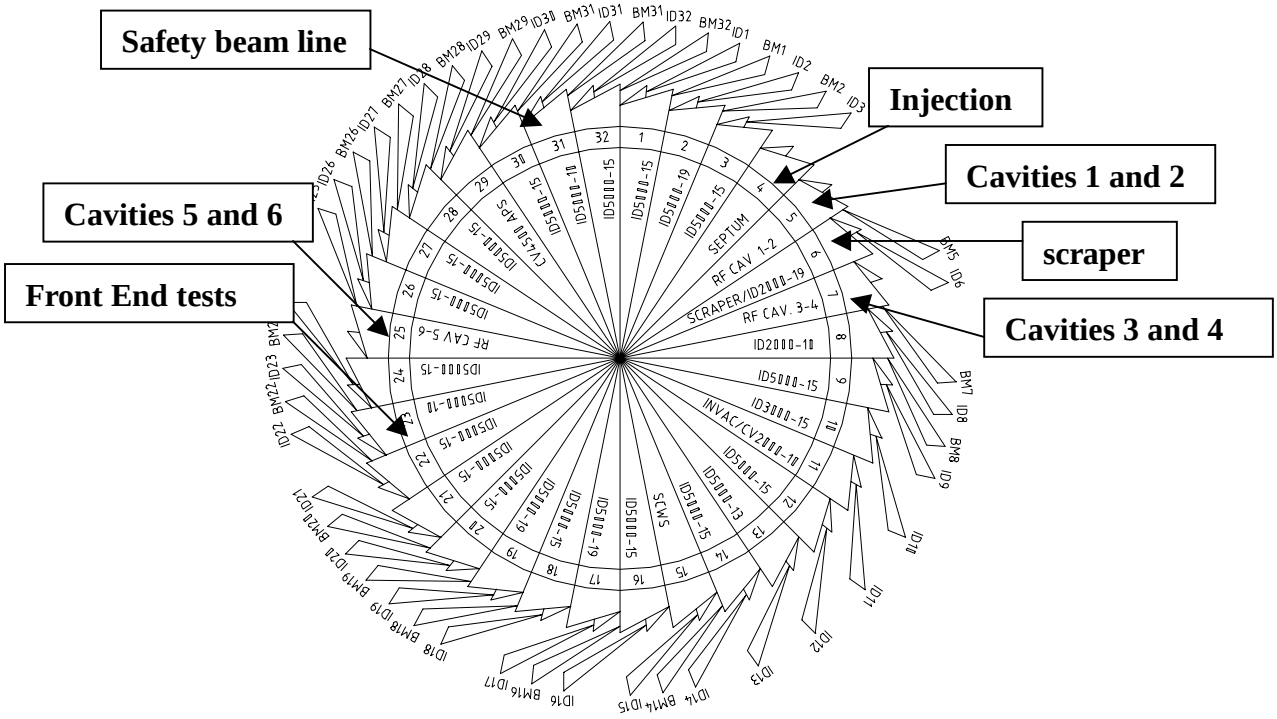

Figure 2-1 Vacuum chamber overview

There are several locations with specific use:
ID4: Injection into the storage ring
ID5: Cavities 1 and 2
Cell 5: One upper scraper jaw until March 99
ID6: Electron beam diagnostic beam line with a shaker, a four-jaw scraper, Current Transformers and one Insertion Device
ID7: Cavities 3 and 4
Cell 22: One upper scraper jaw since March 99
ID23: Straight section used for Front-End (FE) tests and development
ID25: Cavities 5 and 6 since summer 1997
ID31: Beam line used for Radiation measurements since March 98

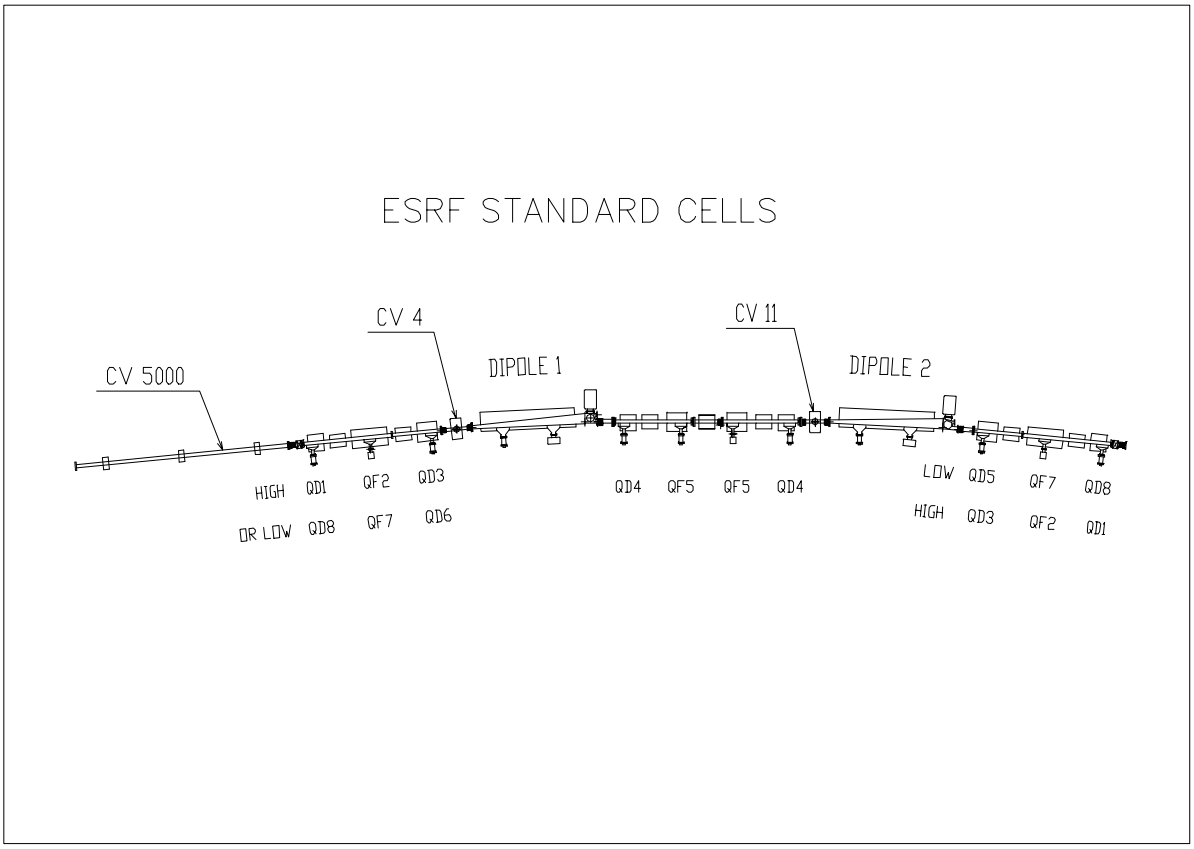

Figure 2-2 magnetic structure of one cell

The basic magnetic structure of each cell is a double bend achromat structure, i.e. two dipoles per cell. All even numbered cells are tuned to small horizontal beam divergence and are called high beta straight sections. All odd cells are on the contrary optimised to small beam dimension and are called low beta straight sections.
The shorter distance between the two dipole magnets is called achromat since it is the location of highest dispersion. It contains two defocusing quadrupoles QD4 and two focusing quadrupoles QF5.
Two quadrupole triplets provide the focusing at both sides of the straight sections. The high beta straight sections are tuned by the magnets QD1, QF2 and QD3. The low beta straight section focusing is achieved with the magnets QD6, QF7 and QD8. Thus there are eight quadrupole families. For each family the magnets are connected in serie (32 or 64 magnets) and fed by one power supply.

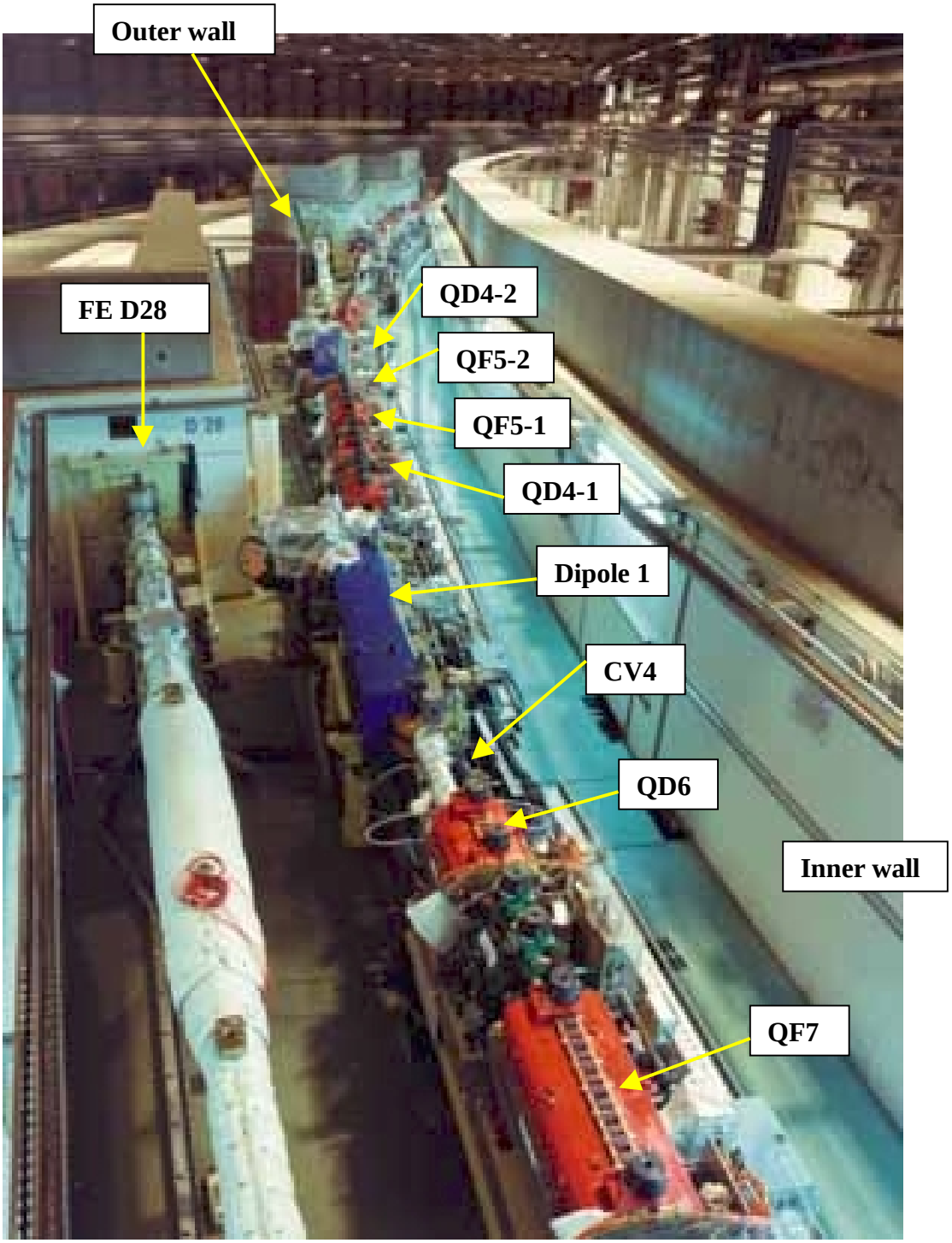

Figure 2-3 View of a storage ring cell

The photo was taken during the construction phase. The second part of the Front End of D28 is seen in white on the left side. From the storage ring on the right side one can easily distinguish in blue the two dipoles of cell 29. From the quadrupoles in red one can see in order QF7, QD6 (before dipole 1), QD4-1, QF5-1, QF5-2 and QD4-2 (between the two dipoles). The vacuum vessel between QD6 and the first dipole is the CV4 vessel of cell 29.

To compensate for chromatic errors and to achieve a sufficiently high dynamic aperture seven sextupoles are mounted per cell, which are powered in 6 families. They are called S4, S6, S13, S19, S22 and S24.

Length of storage ring C [m]	844.4
Nominal electron energy E [GeV]	6.04
Number of straight sections	32
Energy loss per turn from dipoles [MeV]	4.88
Energy loss per turn from IDs [MeV]	0 – 0.6
Nominal electron intensity I [mA]	200
RF frequency ν_{RF} [MHz]	352.2
Number of available buckets h	992

Table 2-1 Main storage ring parameter

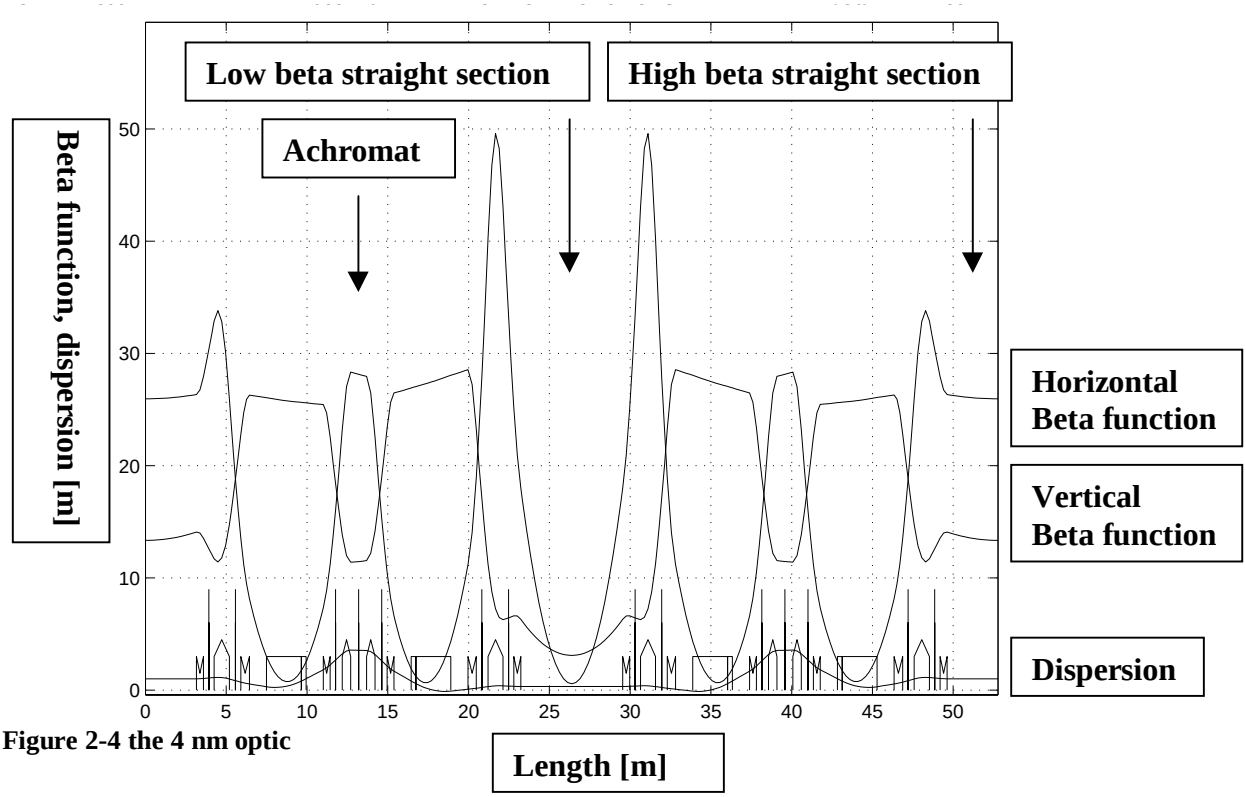

Figure 2-4 the 4 nm optic

The ESRF optic has a 16-fold symmetry. The "4nm" optic is shown which was used until November 96 as nominal optic for operation.

As already mentioned the dispersion has its maximum in the achromat. In the straight sections the dispersion is smaller but not zero.

The horizontal beta function in the low beta straight sections varies from maximum in the QF7 magnets to the minimum in the middle of the straight section. In the high beta straight sections, on the other hand, it remains rather constant at a large value between the quadrupole triplet. The horizontal beta function reaches also small values in the dipoles to achieve a small emittance.

The vertical beta function behaves in the straight sections like the horizontal one. It only has a smaller value in the high beta sections and bigger value in the low betas

straight sections than the horizontal beta function. Along the dipoles, on the other hand, it is rather constant with at a large value.

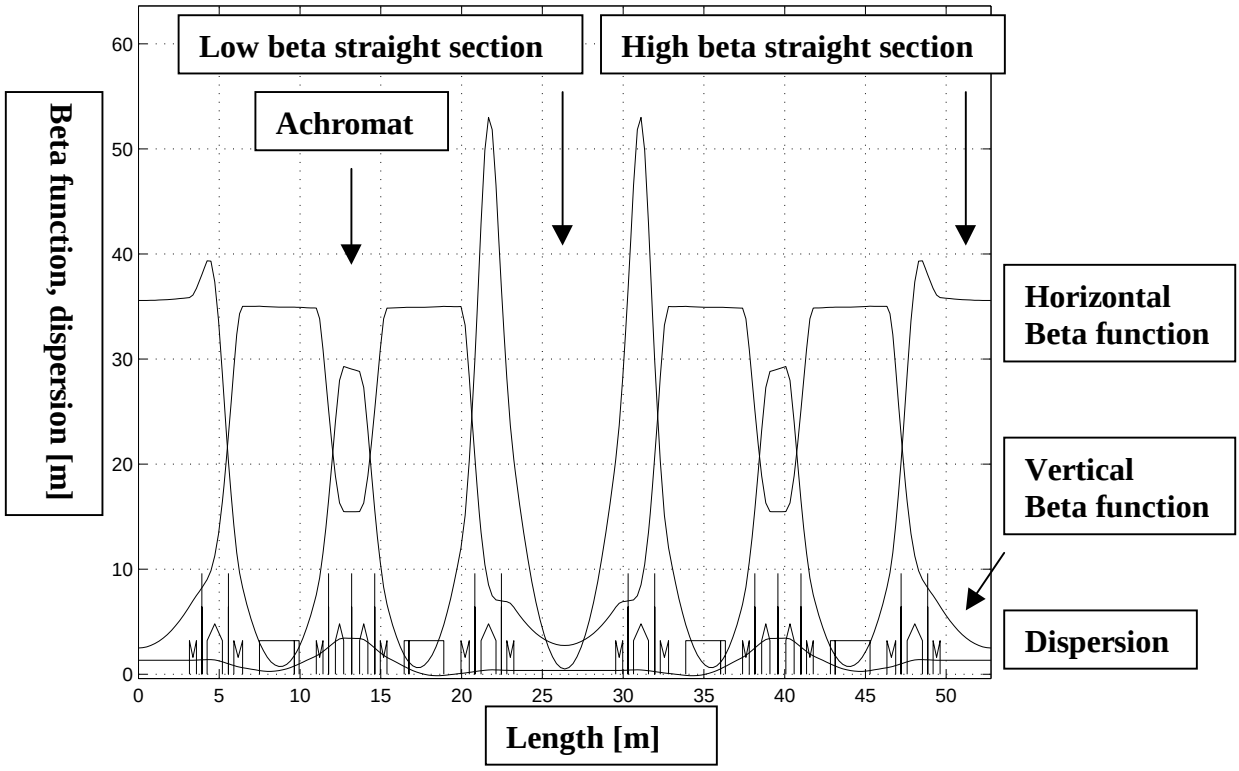

Figure 2-5 the low vertical beta optic

One of the major steps to allow operation with small gap vacuum vessels was the change in the machine optic to the so-called low vertical beta optic. This optic was initiated by the need to match the vertical electron beam size to the photon beam size to take advantage of the small vertical emittance[4]. To do this a smaller vertical beta function in the high beta straight section was looked for. The change was also strongly driven by the need to increase the vertical acceptance in the high beta straight sections for the beam loss reasons[5]. This will be explained in the section 2.4. Finally the optic was optimised with a vertical beta function of 2.5 m in the middle of the high beta straight sections. It was adopted as standard operation optic in November 1996[6]. As can be seen in Figure 2-5 the change of the vertical beta function in the straight sections lead to larger horizontal beta functions in the high beta straight sections as well as to larger vertical beta functions along the dipoles. The different parameters are summarised in the following table:

Parameter	4 nm optic	Low vertical beta optic
Horizontal tune ν_x	36.44	36.44
Vertical tune ν_z	11.39	14.39
Horizontal emittance ε_x [nm]	4	4
Vertical emittance ε_z [nm]	0.04	0.04
Momentum compaction factor α	$2 \cdot 10^{-4}$	$1.9 \cdot 10^{-4}$
Natural energy spread $\delta p/p$	$1.1 \cdot 10^{-3}$	$1.1 \cdot 10^{-3}$
Transverse damping time $\tau_{x,z}$ [ms]	7	7
Longitudinal damping time τ_s [ms]	3.5	3.5
Hor. beta function high beta straight [m]	25.9	35.6
Ver. beta function high beta straight [m]	13.3	2.5
Hor. beta function low beta straight [m]	0.57	0.5
Ver. beta function low beta straight [m]	3.1	2.7

Table 2-2 Main optical parameter

2.2 Brilliance considerations

The photon flux F is defined as the number of photons per second in a given bandwidth of 0.1 %. The brilliance B is defined as

$$B = \frac{F}{4\pi^2 \cdot \sigma_x \cdot \sigma_x' \cdot \sigma_z \cdot \sigma_z'}$$

Equation 2-1 Brilliance definition

with σ_x, σ_x', σ_z and σ_z' as the horizontal and vertical photon beam sizes and photon beam divergences**.**

The spectrum of the synchrotron radiation from an Insertion Device depends largely on the kind of Insertion Device. The main parameter is the undulator parameter K[7], which is defined as

$$K = \frac{\lambda_u \cdot e \cdot B}{2 \cdot \pi \cdot m_e \cdot c} \cong 0.934\, B[T]\, \lambda_u[cm]$$

Equation 2-2 undulator parameter K

with λ_u as undulator period, e as electron charge, B as maximum magnetic field on the beam axis, m_e as electron mass and c as the velocity of light. In case of a K value much larger than one the synchrotron radiation has a continuous spectrum similar to a dipole magnet spectrum and the Insertion Devices is called a wiggler. Its brilliance is proportional to the number of Wiggler periods. In the case of smaller K values the spectrum becomes more and more discrete with very narrow band peaks. The wavelength of the first harmonic on the axis λ_1[8] can be calculated to be

$$\lambda_1 = \frac{\lambda_u}{2 \cdot \gamma^2}\left(1 + \frac{K^2}{2}\right)$$

Equation 2-3 wavelength of the first harmonic of an undulator

with γ being the relativistic factor. To tune the photon energy between the first and the third harmonic one has to be able to shift the first harmonic by a factor of three. Looking to Equation 2-3 this means that a maximum K value of two is necessary. To maintain the K high the product of magnetic field and undulator period has to be maintained high as can be seen from Equation 2-2. For field geometry reasons the undulator period has to be at least twice as long as the minimum Insertion Device gap. This leads to the necessity of small gaps if one wants to use small Insertion device periods. The undulator radiation is on the fundamental proportional to square of the number of periods. Undulators are therefore preferred with respect to wigglers. Due to the small K value they have, however, a smaller magnetic field than wigglers. At high photon energies therefore wigglers have to be used.

2.3 History of Small Gap Vacuum Vessels

At the ESRF higher brilliance was achieved by reducing the undulator periods in several steps. The basic parameter is summarised in Table 2-3.

date	Und. Period	Min. ID gap	Beam aperture	Technology
Since 94	46 mm	20 mm	15 mm	Fixed vacuum vessel
Since 06/95	42 mm	16 mm	11 mm	Fixed vacuum vessel
Since 12/96	35 mm	11 mm	8 mm	Fixed vacuum vessel
Since 01/99	23 mm	6 mm	6 mm	In-Vacuum undulator

Table 2-3 steps to smaller ID gaps at the ESRF

The ESRF's transverse minimum apertures were defined in the Foundation Phase Report[9] to be 70 mm full size aperture in the horizontal plane and 30 mm full size aperture in the vertical plane. The chamber size that was finally accepted was 74 mm in the horizontal plane and 33 mm in the vertical plane.

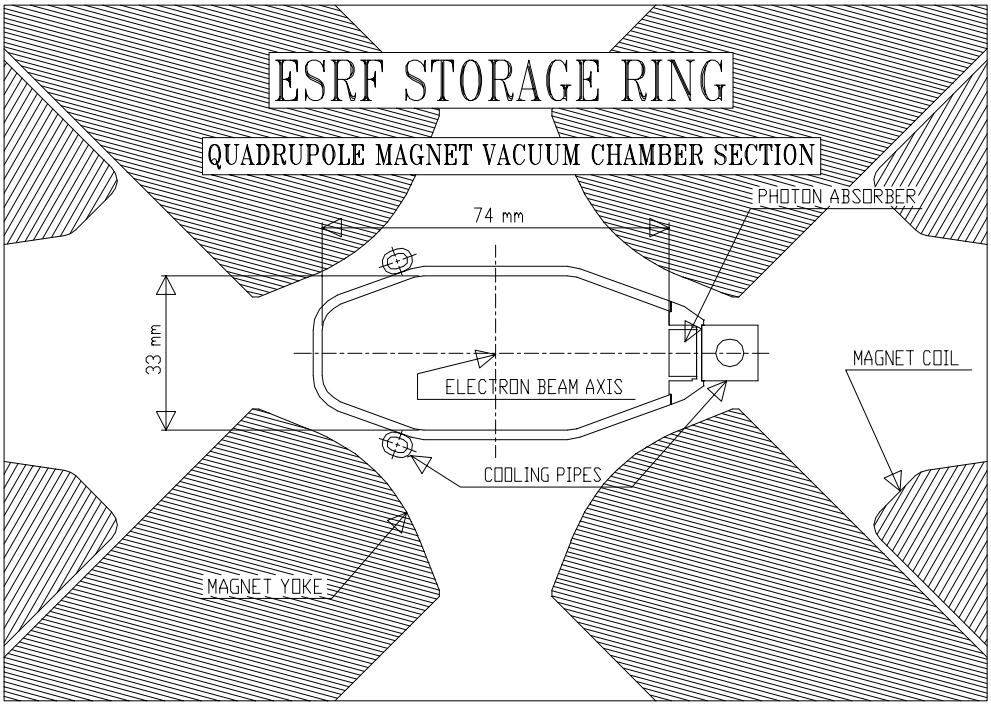

Figure 2-6 Standard vacuum chamber cross section

During the last years straight section vacuum vessels were the only elements in the vacuum system, which were changed according beam line requirements. As already mentioned it is the outer vertical aperture of the vacuum chamber, which has to be kept small. Insertion Device vacuum vessels are therefore flat shaped keeping the horizontal aperture at standard dimension. To allow the installation of several Insertion Devices most of the straight section chambers are about 5 m in length. At the ESRF the standard length of an Insertion Device is 1.65 m. This allows the installation of up to 3 Insertion Devices per straight section. In case of an undulator tunability of the harmonics is required to cover the full wavelength spectrum.

For the design of an Insertion Device for an operating beam line one wants to reach maximum brilliance for a given wavelength region. To reach very high energies one has to work on high harmonics on undulators. Above a certain energy wiggler radiation will become superior due to the higher possible magnetic field. Following Equation 2-3 one has to use small undulator periods to achieve high photon energies from undulator radiation. To keep the k value high one has therefore to go to large magnetic fields. A practical limit to this approach is given by the minimum gap, which is allowed for the undulator. To have sufficient magnetic field on axis it is mandatory to keep the undulator period twice as large as the minimum gap[10]. Most undulators are mounted outside vacuum so that the vacuum chamber dimension defines the limit. For very small gaps In-Vacuum Undulators have to be used[11 and 12].

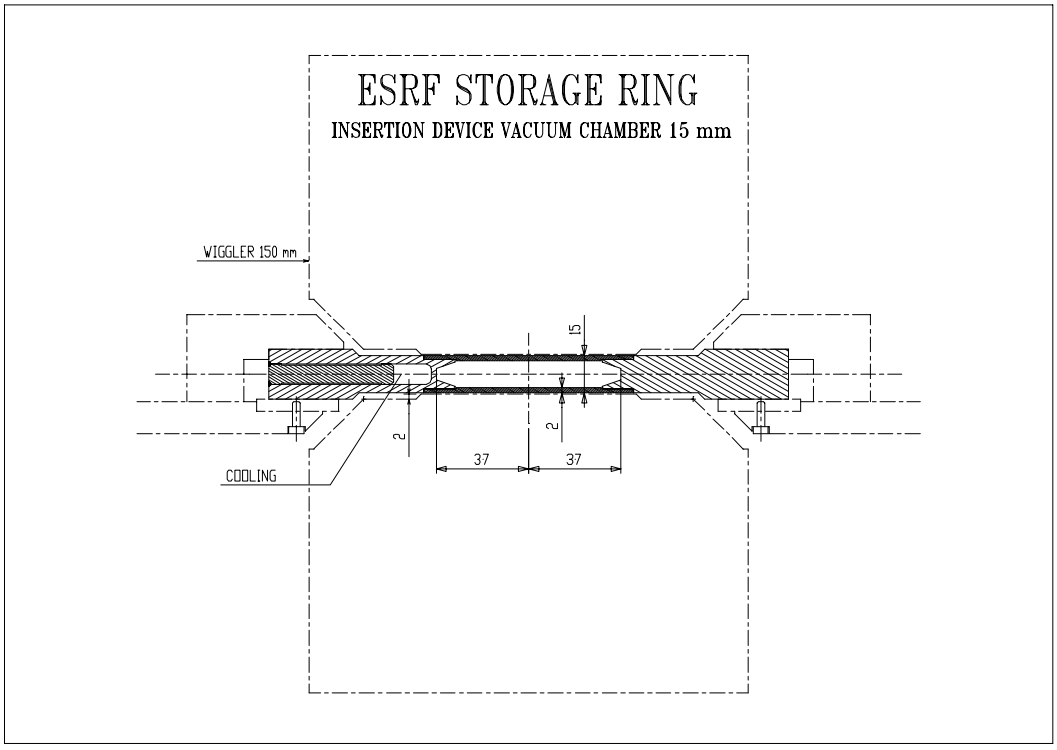

Figure 2-7 Cross section of a CV15

The first set of Insertion Device vessels had an outer vertical aperture of 19 mm with an inner aperture of 15 mm. On the low beta straight section of ID 13 a special chamber of an outer aperture of 13 mm and an inner aperture of 9 mm was then installed.

To allow smaller gap Insertion Devices a new set of Insertion Device chambers was designed and installation started from summer 1995. These chambers are characterised by a 15 mm outer vertical aperture and an 11 mm inner aperture.

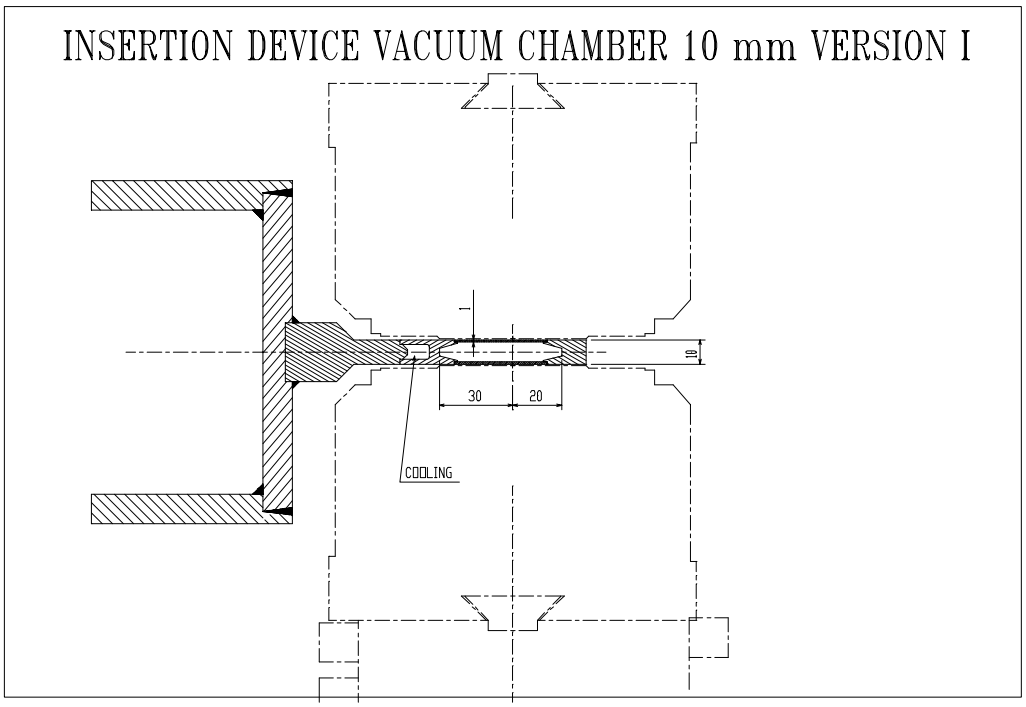

Figure 2-8 Cross section of a CV10

Figure 2-9 Photo of 8 mm inner aperture CV5000 vacuum chamber in ID31

Installation of a more recent Insertion Device chamber design started in December 1996. These chambers have a 10 mm outer aperture chambers and 8 mm inner aperture (Figure 2-8). To maintain mechanical stability with the reduced chamber wall thickness

(1mm instead of the former 2 mm) the inner horizontal half aperture was reduced from 37 mm to 20 mm.

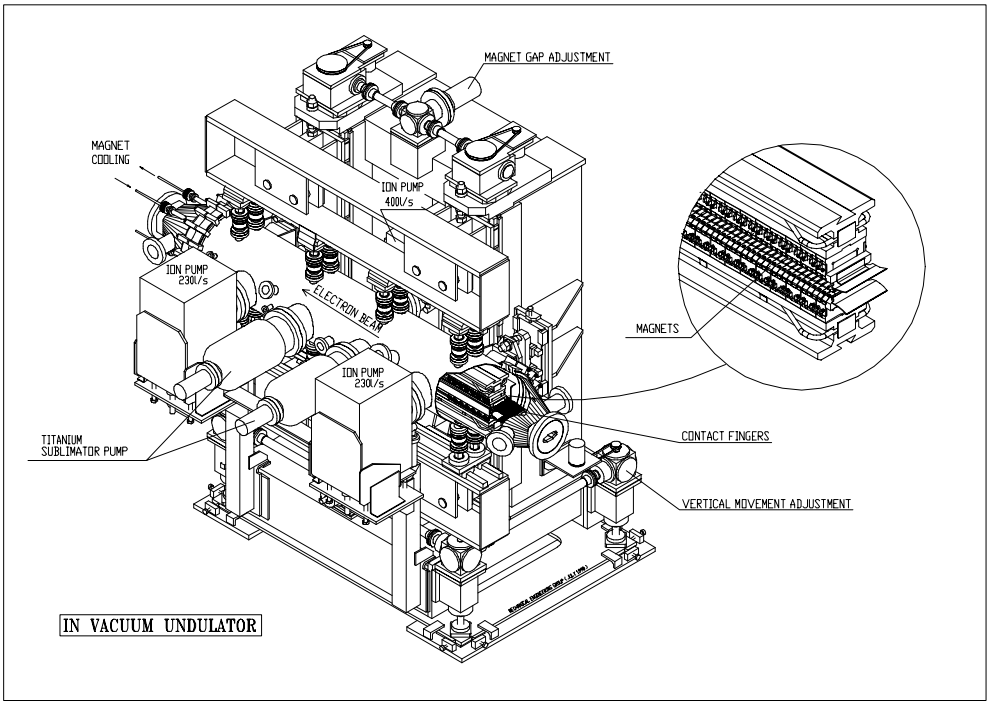

Figure 2-10 View of the In-Vacuum Undulator at the ESRF.

In contrary to the standard technology the In-Vacuum undulator technology consist of having the undulator inside the vacuum vessel. This gives a gain in the minimum gap of the usual vacuum chamber wall thickness. Since the gap has to be movable the minimum aperture seen by the beam is also variable which gives flexibility for example during injection. The In-Vacuum undulator technology is, on the hand, more complicated, more expensive and less flexible in terms of undulator exchange due to need of an vacuum intervention.
With the In-Vacuum Undulator technology at the ESRF undulator radiation is superior to wiggler radiation up to a photon energy of 70 keV.

For completeness it has to be mentioned that in ID10 there is also a minigap undulator installed. In consist of an Insertion Device which is installed on a movable vacuum vessel. Due to technical problems this device is, however, very short and was therefore practically not used at small gaps for the beamline operation. Since at larger gaps it did not cause any aperture reduction it is not taken into account in the further discussions. The technology to mount insertion devices on movable vacuum vessels is now ruled out by the In-Vacuum technology[11].

The different vacuum chamber installations during the last years are listed in the following table. The installation of 16 vacuum chambers of 11 mm inner aperture was finished in October 98. The main requests now lie on the 8 mm inner vertical aperture chambers and the In-Vacuum undulators.

Date	Location	Inner vertical aperture
6/1995	ID13	9 mm
7/1995	ID12	11 mm
7/1995	ID18	11 mm
10/1995	ID1	11 mm
10/1995	ID30	11 mm
11/1995	ID9	11 mm
12/1995	ID16	11 mm
5/1996	ID14	11 mm
5/1996	ID27	11 mm
7/1996	ID21	11 mm
7/1996	ID22	11 mm
9/1996	ID26	11 mm
11/1996	ID3	11 mm
12/1996	ID23	11 mm
12/1996	ID27	8 mm
3/1997	ID11	8 mm
5/1997	ID20	11 mm
7/1997	ID10	11 mm
7/1997	ID32	11 mm
11/1997	ID28	8 mm
12/1997	ID31	8 mm
12/1997	ID24	11 mm
5/1998	ID23	8 mm
10/1998	ID29	8 mm
10/1998	ID28	11 mm
1/1999	ID11	In-Vacuum

Table 2-4 History of ID chamber installation

2.4 Transverse Acceptances

For the discussion of beam losses the transverse acceptances will be essential. They depend on the vacuum chamber half aperture d(s) at the position s around the ring as well as the beta function at that point. For each point one can for example calculate the local vertical acceptance from

$$z_m(s) = \sqrt{A_z(s) \cdot \beta_z(s)} = d(s).$$

to be

$$A_z(s) = \frac{d^2(s)}{\beta_z(s)}$$

The phase space at the point at that point is illustrated in Figure 2-11.

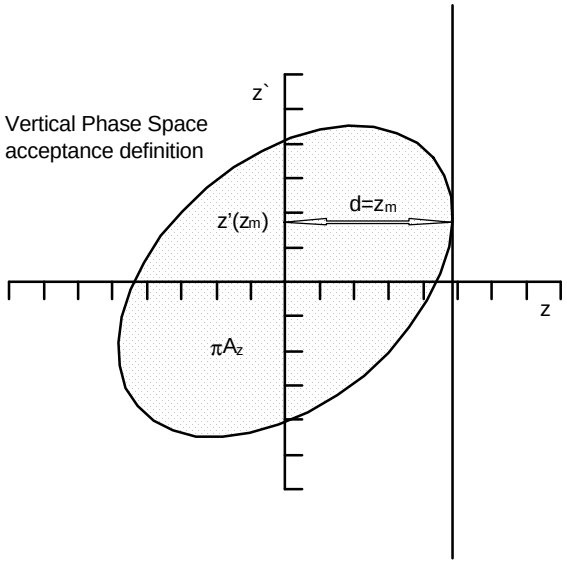

Figure 2-11 Vertical Acceptance phase space

The phase space surface in which the electrons remain stable has the surface π $A_z(s)$. One can derive the total vertical acceptance A_z of the storage ring to be

$$A_z = Minimum_s\ A_z(s) = Minimum_s\left[\frac{d^2(s)}{\beta_z(s)}\right]$$

Equation 2-4 Vertical acceptance

Each vacuum chamber with its inner vertical aperture represents a local limitation to the vertical beam oscillations. The overall vertical acceptance is, however, only defined by the smallest limitation around the ring.

The angle where the acceptance ellipse touches the vertical physical aperture is

$$z'(z_m(s)) = -\alpha_z(s)\sqrt{\frac{A_z(s)}{\beta_z(s)}} = -d(s)\frac{\alpha_z(s)}{\beta_z(s)}$$

Equation 2-5 vertical angle at maximum vertical position

In the horizontal plane one has to take into account the dispersion D(s). The horizontal acceptance $A_x(s)$ should therefore be defined as a function of the energy offset $A_x(s, \Delta p/p)$. Again the phase space is drawn at the location where the horizontal acceptance is limited.

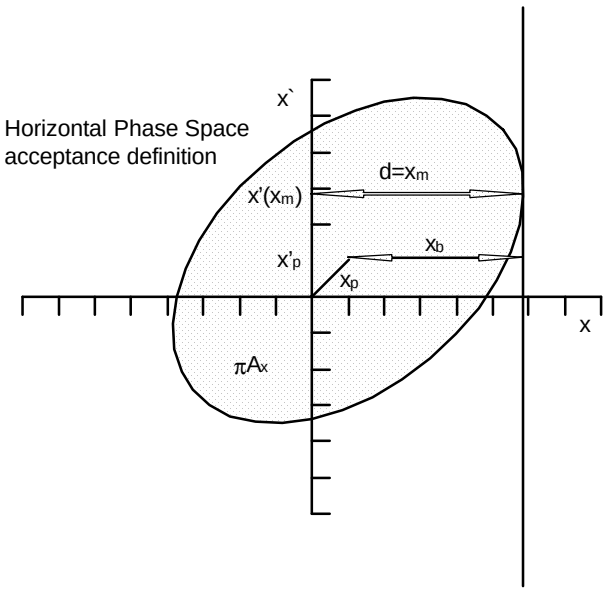

Figure 2-12 Horizontal phase space

For the horizontal acceptance one can use the following relations

$$d(s) = x_m(s) = x_b(s) + x_p(s) = \sqrt{A_x(s) \cdot \beta_x(s)} + D(s) \cdot \Delta p / p$$

The horizontal acceptance can then be defined as

$$A_x(\Delta p/p) = Minimum_s\ A_x(s, \Delta p/p) = Minimum_s \left[\frac{(d(s) - D(s) \cdot \Delta p/p)^2}{\beta_x(s)} \right]$$

Equation 2-6 horizontal acceptance

The horizontal angle where the acceptance ellipse touches the aperture can be taken from the following relations:

$$x'(x_m(s)) = x_b'(s) + x_p'(s) = -\alpha_x(s)\sqrt{\frac{A_x(s)}{\beta_x(s)}} + D'(s) \cdot \frac{\Delta p}{p}$$

$$= -d(s)\frac{\alpha_x(s)}{\beta_x(s)} + (\frac{\alpha_x(s)}{\beta_x(s)} D(s) + D'(s))\frac{\Delta p}{p}$$

Equation 2-7 maximum angle at horizontal aperture limitation

Vacuum chambers normally have a constant aperture. To calculate the acceptance of one chamber one has therefore to look for the maximum beta function along the vessels. Insertion Device vacuum chambers are installed in straight sections. One can therefore use the equation for the beta function development in a straight section[13].

$$\beta(s) = \beta(0) + {s^2}/{\beta(0)}$$

Equation 2-8 evolution of the beta function in a straight section

The point s = 0 is here the point where the beta function is minimum.
The other Twiss parameter is

$$\alpha(s) = -\frac{1}{2}\beta'(s) = -\frac{s}{\beta(0)}, \quad \gamma(s) = \frac{1+\alpha^2(s)}{\beta(s)} = \frac{1}{\beta(0)}$$

Equation 2-9 Twiss parameter in a straight section

In order to ease the following formula we define the half length D of a straight section with the length L to be D=L/2. The phase advance $\Delta\Psi$ from –D to D along the straight sections is

$$\Delta\Psi = \int_{-D}^{D} \frac{1}{\beta(s)} ds = \int_{-D}^{D} \frac{1}{\beta(0) + \frac{s^2}{\beta(0)}} ds$$

$$\Delta\Psi = \beta(0) \int_{-D}^{D} \frac{1}{\beta^2(0) + s^2} ds = \arctan\left(\frac{D}{\beta(0)}\right) - \arctan\left(\frac{-D}{\beta(0)}\right)$$

Equation 2-10 phase advance in a straight section

The development of the different beta functions along the 5 m long ESRF straight sections are shown in Figure 2-13 and Figure 2-14 for the two different optics.

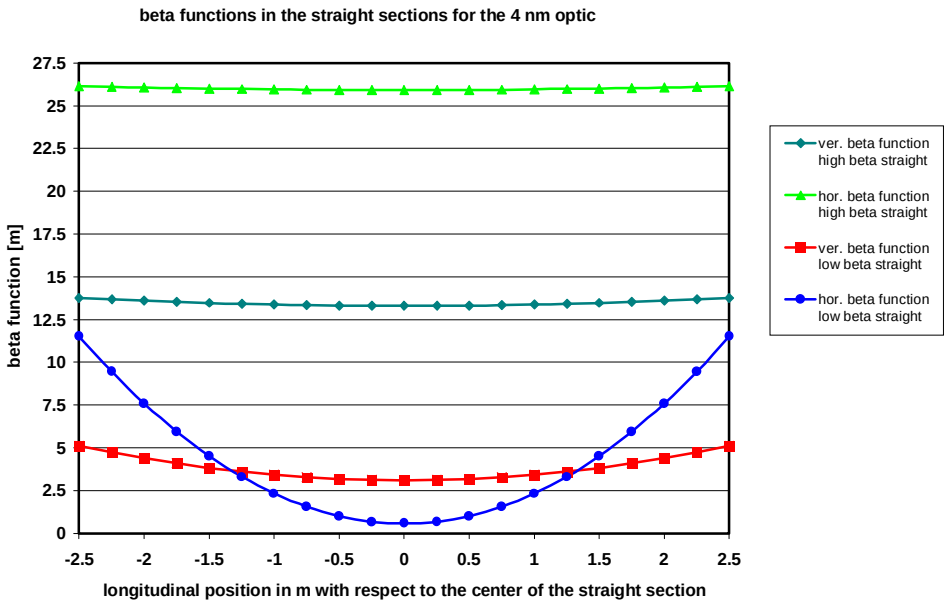

Figure 2-13 Beta functions in the 4 nm optic

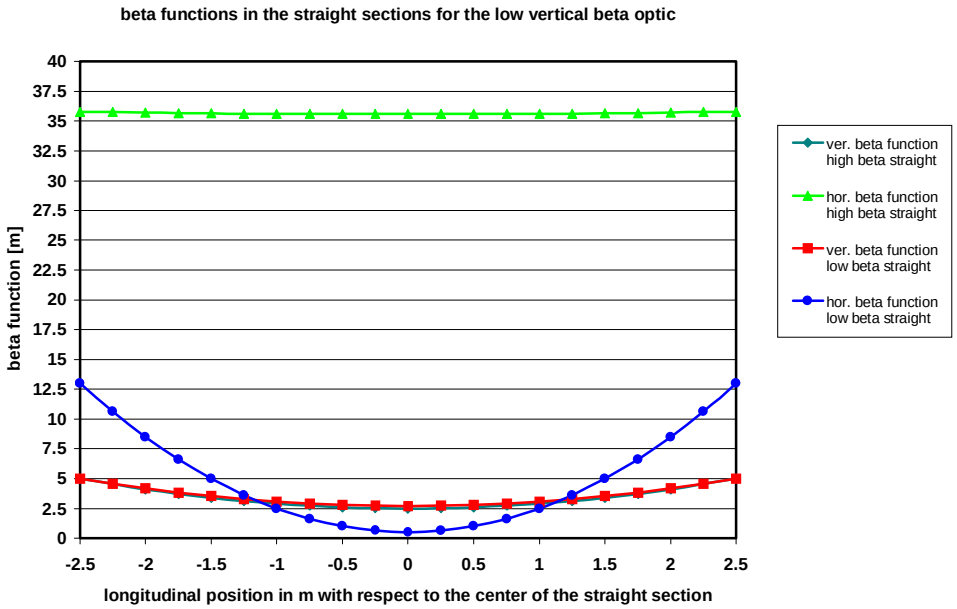

Figure 2-14 Beta functions in the low vertical beta optic

Using **Equation 2-4** and **Equation 2-8** the vacuum chamber acceptance can be calculated:

$$\beta_{\max} = \beta(D) = \beta(-D) = \beta(0) + D^2 \Big/ \beta(0)$$

$$A(\beta(0)) = \frac{d^2}{\beta_{\max}} = \frac{d^2}{\beta(0) + D^2 \Big/ \beta(0)} = \frac{d^2 \cdot \beta(0)}{\beta(0)^2 + D^2}$$

Equation 2-11 Total vacuum chamber acceptance

It is also possible to calculate the maximum position and angle the electrons can have along the straight section vacuum vessel:

$$z_{\max}(s) = \sqrt{A(\beta(0)) \cdot \beta(s)} = \sqrt{\frac{d^2 \cdot \beta(0)}{\beta^2(0) + D^2} \cdot \left(\beta(0) + \frac{s^2}{\beta(0)} \right)} = d \sqrt{\frac{\beta^2(0) + s^2}{\beta^2(0) + D^2}}$$

Equation 2-12 Maximum acceptable electron position along a straight section

$$z'_{\max}(s) = \sqrt{\frac{A(\beta(0))}{\beta(0)}} = \sqrt{\frac{d^2 \cdot \beta(0)}{\beta^2(0) + D^2} \cdot \frac{1}{\beta(0)}} = \frac{d}{D} \sqrt{\frac{D^2}{\beta^2(0) + D^2}}$$

Equation 2-13 Maximum acceptable electron angle along the straight section

For the different beta functions and apertures the acceptances in the 4 nm optic are:

Location	Inner vertical aperture [mm]	Maximum vertical beta function β_z [m]	Vertical acceptance A_z [m rad]
Standard vessel	33	27.5	$9.9\ 10^{-6}$
High beta straight	15	13.8	$4.1\ 10^{-6}$
High beta straight	11	13.8	$2.2\ 10^{-6}$
Low beta straight	15	5.1	$11.0\ 10^{-6}$
Low beta straight	11	5.1	$5.9\ 10^{-6}$
Low beta straight	9	5.1	$4.0\ 10^{-6}$

Table 2-5 Chamber acceptances in the 4nm optic

Before the installation of the small gap vessels the total vertical acceptance was limited to about $10\ 10^{-6}$ m rad. This was reduced to $4\ 10^{-6}$ when installing the 9mm inner aperture vessel in ID13. Installing the 11mm inner aperture vessels in the high beta straight sections reduced this value again by about a factor two to a total vertical acceptance of $2.2\ 10^{-6}$ m rad. The chamber acceptance around the ring is shown in the following figure with the vacuum chamber situation of November 1996.

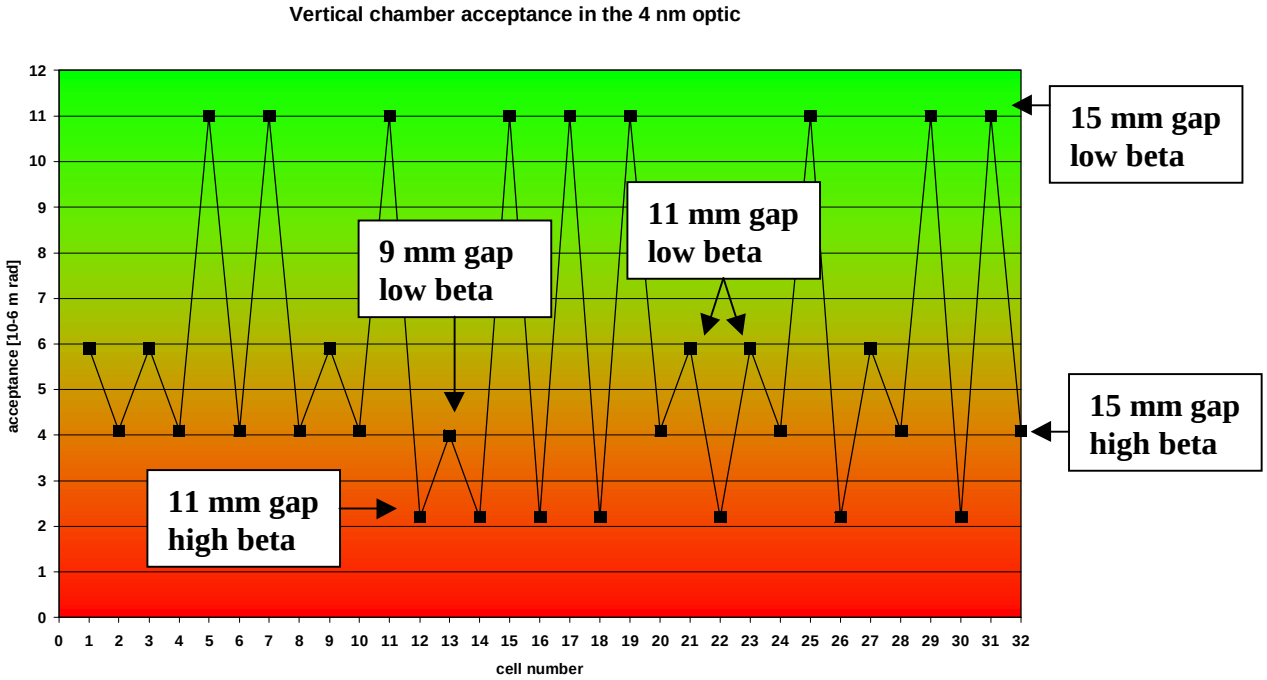

Figure 2-15 Vertical chamber acceptances in the 4 nm optic

The switch to the low beta optic lead to the following chamber acceptances:

Location	Inner vertical aperture [mm]	Maximum vertical beta function β_z [m]	Vertical acceptance A_z [m rad]
Standard vessel	33	35	$7.8\ 10^{-6}$
High beta straight	15	5.0	$11.3\ 10^{-6}$
High beta straight	11	5.0	$6.1\ 10^{-6}$
High beta straight	8	5.0	$3.2\ 10^{-6}$
Low beta straight	15	5.0	$11.3\ 10^{-6}$
Low beta straight	11	5.0	$6.1\ 10^{-6}$
Low beta straight	9	5.0	$4.1\ 10^{-6}$
Low beta straight	8	5.0	$3.2\ 10^{-6}$

Table 2-6 Chamber acceptances in the low vertical beta optic

The distribution of the different chamber acceptances around the machine in July 1999 is shown in the following figure:

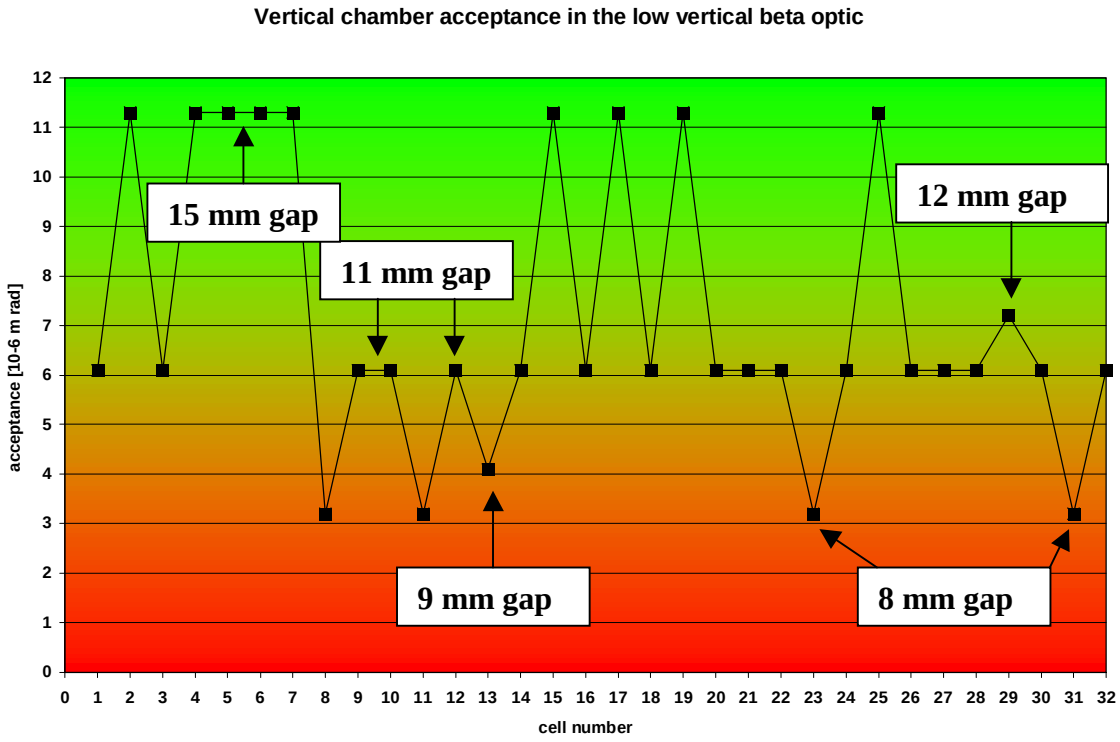

Figure 2-16 Vertical chamber acceptances in the low vertical beta optic

Due to the reduction of the vertical beta functions in the high beta straight sections the vertical acceptance of the 11 mm vacuum chambers was increased from $2.2\ 10^{-6}$ m rad to $6.1\ 10^{-6}$ m rad. Half of the straight sections are now equipped with these vessels.
The 8 mm inner aperture vessel now gives the total vertical acceptance of 3.2 10-6 m rad.

2.5 Injection process and horizontal Acceptances

At the ESRF the injection takes place in cell 4. It is a horizontal injection scheme using a closed orbit bump with 4 kicker magnets. The injected beam is steered towards the stored beam via two septum magnets- S1/2 and S3. The injected beam enters the storage ring vacuum chamber at the exit of the S3 vacuum vessel about 1 m downstream the middle of the straight section. If the kicker bump is well closed the stored beam will not be excited during the injection process. The injected beam will on the other hand oscillate around the closed orbit. The oscillation is then damped by the radiation damping within a few damping times.

The maximum repetition rate of the injector system is 10 Hz and is used during the filling of the few bunch modes, which are described in chapter 2.6.1. The normal repetition rate for the 200 mA multibunch mode of operation is, however, 1 Hz. In both cases the time necessary to achieve the maximum intensity is in the range of two minutes.

The injection process is shown in the following figure:

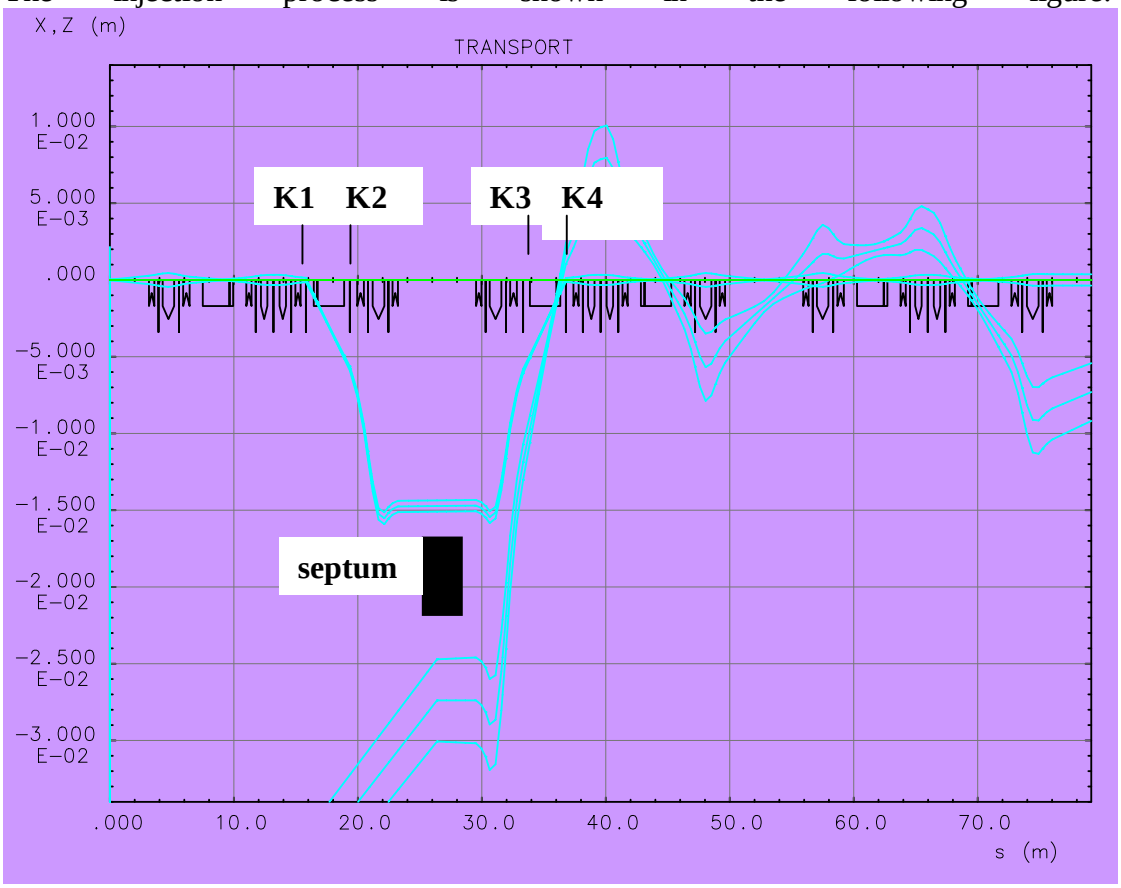

Figure 2-17 the injection scheme at the ESRF

The graph shows the 3 sigma envelopes of the stored beam and the injected beam with respect to the axis of the storage ring. The part of the ring, which is shown, is from the middle of ID3 to the middle of ID5.

To gain injection efficiency, the strength of the last two kickers can be increased to reduce the oscillation amplitude of the injected beam. This reduces the overall acceptance needed by the injected beam but induces some oscillation of the stored

beam[14]. This tuning is applied at the ESRF as standard injection. For single bunch operation, however, the kicker bump has to be perfectly closed as oscillation of the high intensity single bunch excite transverse beam instabilities[15].
In the horizontal plane the S3 septum sheet limits the acceptance. However, to keep some flexibility the septum was designed to be movable[16]. This allows the septum sheet positions between 13.5 mm and 19.5 mm with respect to the SR axis on the inner side of the ring. Until January 1997 the septum sheet was positioned at 13.5 mm. To gain horizontal acceptance after having switched to the low vertical beta optic the septum sheet was moved to 19.5 mm at that time.

Optic used	aperture	Hor. beta function β_x	Hor. acceptance A_x
4 nm	13.5 mm (septum)	25.9 m	7.0 10^{-6} m rad
Low ver. beta	13.5 mm (septum)	35.6 m	5.1 10^{-6} m rad
Low ver. beta	19.5 mm (septum)	35.6 m	10.7 10^{-6} m rad
both	34 mm (standard)	51 m	23 10^{-6} m rad

Table 2-7 Horizontal acceptance limitation from the septum sheet for on momentum particles

The injection scheme does not impose any reduction to the vertical acceptance. The impact of the transverse acceptances on the beam losses during injection will be discussed in chapter 0.

2.6 User Service Mode

The ESRF operation can be divided in three states:

- the shutdowns which are used for interventions and maintenance without beam
- the Machine Dedicated Time (MDT) which is used for machine studies and preparation of the machine for the users
- the User Service Mode (USM) with beam delivery to the users for about 5600 hours a year

The distribution of the different ESRF operation modes can be seen in Figure 2-18

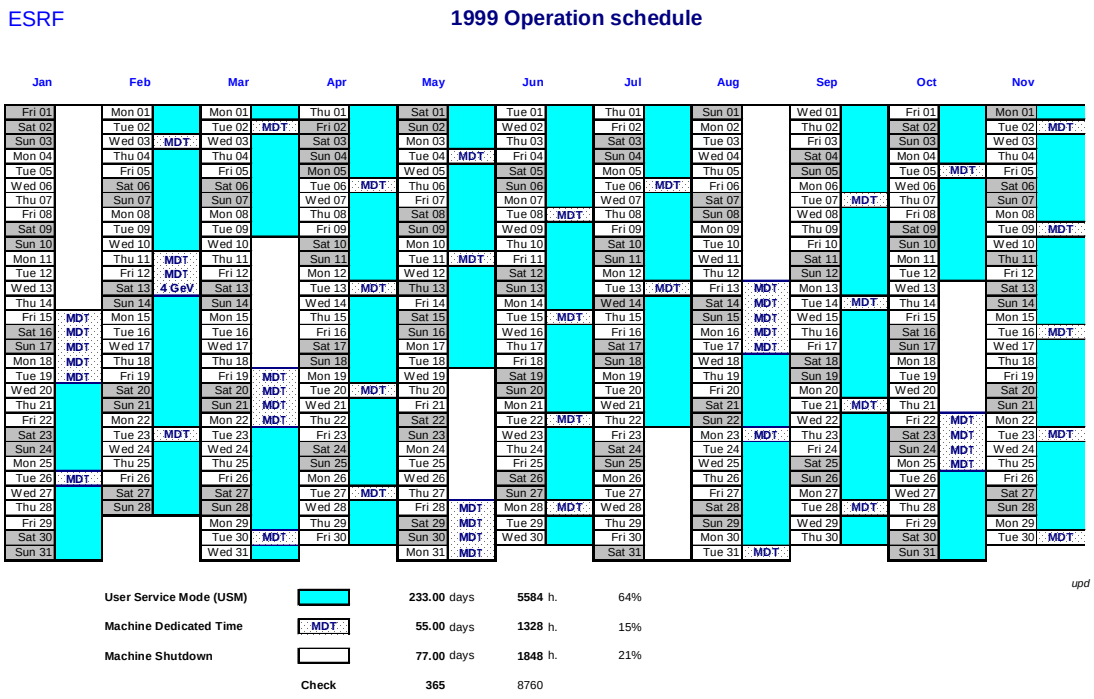

Figure 2-18 Operation schedule of the ESRF

2.6.1 Filling patterns

During the User Service Mode (USM) the beam lines are allowed to take beam. In that case the Front End, which is the connection between the storage ring and the beam line, remains open and the synchrotron radiation can pass through the tunnel wall into the beam line. Before injecting, however, the Front Ends have to be closed. This is in order to prevent electrons lost during the injection process to leave the tunnel via the open Front End. There are different kinds of beam delivery modes[17]:

- the 1/3-filling mode: standard mode until October 1996
- the 2/3-filling mode: standard mode from October 1996 to March 1999
- the 2 x 1/3-filling mode: standard mode since April 1999
- the 16 bunch mode: 16 equally spaced bunches
- the single bunch mode: one single bunch
- the hybrid 1 mode: 1/3-filling opposite to a single bunch

The main parameters are shown in the following table:

Fill mode	Number of bunches N_b	Maximum Intensity I [mA]	Lifetime τ [hours]	Number of refills per day	Maximum Intensity per bunch I_b [mA]
1/3-filling	352	200	40	2	0.57
2/3-filling	704	200	60	2	0.28
2 x 1/3-filling	704	200	60	2	0.28
16 bunch	16	90	12	4	5.6
Single bunch	1	16	6	6	16
Hybrid 1	352 + 1	193 + 7	40 +7=>35	2	0.57 + 7

Table 2-8 filling patterns at the ESRF

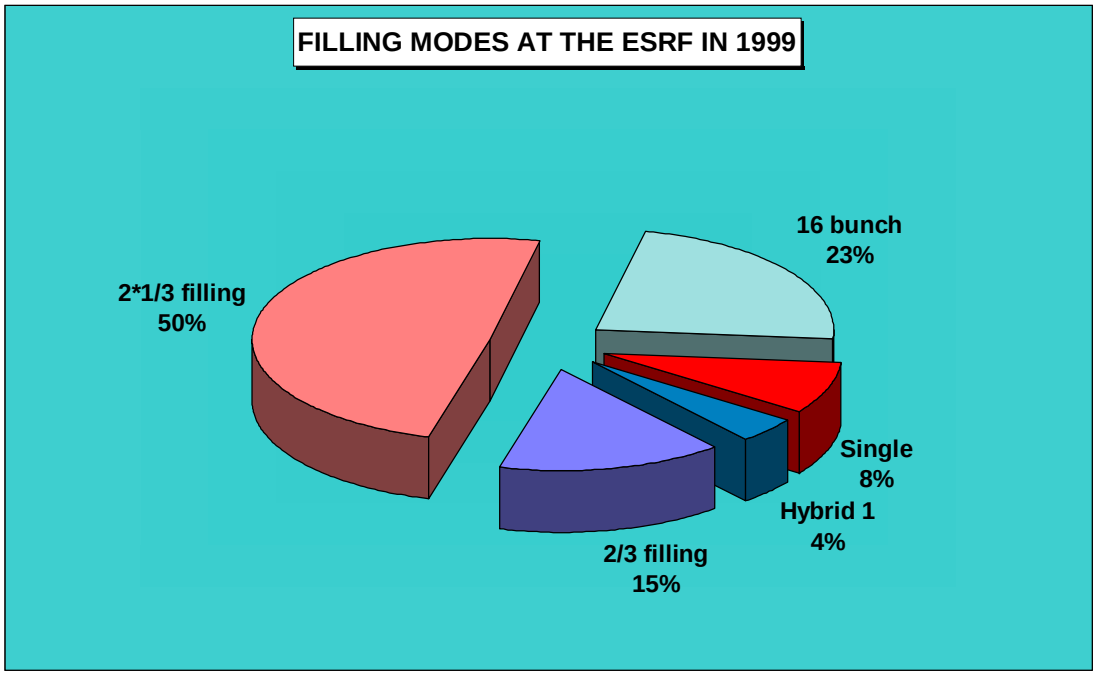

Figure 2-19 filling pattern distribution in 1999

The change from the 1/3-filling to the 2/3-filling was initiated from the attempt to reduce the beam losses by increasing the lifetime. The beam lifetime will be discussed in chapter 3.2. The switch to 2 x 1/3-filling followed the upgrade of the cavity water temperature control and was requested by users who benefit from the time structure.

For all high current per bunch modes, i.e. single bunch, 16 bunch and hybrid mode, it is necessary to keep all the other buckets empty, i.e. less than 5 nA in them. This is requested by the Mössbauer spectroscopy beam lines ID18 and ID22 which measure the relaxation of exicted states in the time windows between the bunches. To achieve this purity a cleaning procedure is used at the ESRF, which consists in exciting a vertical oscillation of the beam with a vertical shaker. Due to the vacuum chamber impedance there is a tune difference between bunches with many electrons and bunches with few electrons. If one chooses the frequency of the shaker excitation correctly it is possible to excite a strong vertical oscillation of only the electrons in the lowly populated bunches. The extracted electrons are collected on a scraper jaw, which is inserted vertically towards the beam axis. The full process is called cleaning and by its nature is a source of beam loss. In well optimised conditions, however, the initial filling after injection is already so good that less than 1 % of the total electrons are placed in unwanted buckets and are therefore lost during the cleaning process.
An important problem with this cleaning procedure is that it attacks all lowly populated bunches which is particularly penalising in the hybrid mode. To avoid dipole vacuum chamber over-heating due to a vertical beam blow-up it was therefore necessary to kill the beam prior to a refill in hybrid mode. During hybrid mode operation this beam kill was the main source of beam loss as it occurred every twelve hours (There were two scheduled refills per day in this filling mode).
To reduce the losses in that mode a gated cleaning was put into operation for the Hybrid 1 mode. The cleaning only applies a shaker excitation in a 1 μs time window around the single bunch and leaves the 1/3-bunch train untouched. As a consequence topping-up was made possible and the beam losses in the hybrid 1 filling were reduced by more than a factor of 2.

Another aspect of the different filling patterns are the transverse single bunch instabilities. At the ESRF it is necessary to operate the machine with the vertical and the horizontal chromaticity at large positive value[18]. An overview is given in the following table:

Single bunch intensity	Vertical chromaticity	Horizontal chromaticity
0.3 mA	6	3
5 mA	9	5
16 mA	13	7

Table 2-9 Chromaticity in the different filling patterns

2.6.2 Failures during USM

During normal operation of the machine additional losses occur due to equipment failures or unsafe situations for either the personnel or the machine equipment.

A trip on the RF system, for example, leads to a very fast beam loss due to a lack of RF voltage. The electrons permanently lose 0.1% of their energy per turn and are therefore lost, at the most, after about 100 turns or 280 μs.
A trip of a main power supply is another event which directly kills the beam

In many cases it is also necessary to kill the beam to protect machine equipment from damage. Some examples are:
- Automatic valves close when there is a significant rise in the vacuum pressure. In this event it is necessary to kill the beam to prevent overheating of the valves.
- If a Front End shutter closes without the movable absorber closing the beam has to be killed to avoid the shutter overheating.
- If the beam becomes unstable in the vertical plane or is displaced in the vertical plane there is a risk of heating a dipole vacuum chamber with the synchrotron radiation and thereby melting it. A beam kill is therefore necessary.
- If the cooling of a vacuum chamber fails the beam is killed to avoid overheating the chamber.

For all these cases a hard wired machine interlock system will trip the storage ring RF system to ensure a fast beam dump before any damage due to overheating can develop.

For personnel protection the Personnel Safety System PSS is used. For example, if a door of an optics hutch is opened while the Front End is still open the beam is killed. The same action is applied if a person tries to enter into the tunnel while there is still beam stored. The beam has to be killed before a door can be fully opened. This is done by tripping the RF as well as inserting what is called a "beam killer". This device creates an energy loss for the electrons that is greater than what can be recuperated from the RF so that even without the RF stopping, the beam is lost.

Another origin of beam loss comes from pushing an emergence stop button, which trips equipment, which is necessary to maintain the beam, stored. The stop button actions differ depending on the position but they will always trip power supplies.
A standard figure of the mean time between failures at the ESRF is 40 hours. This means that, on average, every 40 hours a trip, like one mentioned above, occurs.

2.7 Radio Frequency and longitudinal beam parameter

2.7.1 RF settings

The main RF system of the storage ring from the restart of the ESRF consisted of 4 cavities fed by one or two transmitters. The standard operation voltage was 8 MV.
More recently a third RF unit called SRRF3[19] was installed and commisioned. It consists of a pair of cavities installed in cell 25 and a 1 MW transmitter station able to feed it. This installation is operational since summer 1997 and increased the maximum RF voltage from 8 MV to 12 MV. The optimum RF settings are different for the different filling patterns:

- For lifetime reasons it is useful to operate the machine at the lowest RF voltage which does not reduce the energy acceptance[20]. 8 MV has been found as good compromise.
- For a correct cavity tuning, however, a minimum voltage of 1.5 MV per active cavity has to be applied.

- Up to 150 mA beam current can be supplied from one transmitter and 4 cavities.

The different RF tunings are listed in the following table:

situation	SRRF1	SRRF2	SRRF3
200 mA in 1996	4 MV, cav. 1 + 2	4 MV, cav. 3 + 4	-
200 mA in 1999	8 MV, cav. 1 to 4	-	4 MV, cav. 5 + 6
16 bunch	8 MV, cav. 1 to 4	-	-
Single bunch	8 MV, cav. 1 to 4	-	-

Table 2-10 RF settings for different filling patterns

For completeness is has to be mentioned that some other filling patterns and RF tunings were temporary used at the ESRF[21].

2.7.2 Longitudinal parameter

The **momentum compaction factor** $\alpha = \frac{\Delta C/C}{\Delta p/p}$ with C as length of the closed orbit is given by the machine lattice and can be calculated as follows

$$\alpha = \frac{1}{C}\oint \frac{D(s)}{R(s)} ds$$

Equation 2-14 momentum compaction factor

With R(s) being the bending radius in the dipoles. For third generation light sources the dispersion function is kept small in the dipoles to minimise the horizontal emittance. This results also in a small momentum compaction factor.

The electrons are performing synchrotron oscillations in the longitudinal plane[22]. The **synchronous phase** ψ_s is given by

$$\sin(\psi_s) = \frac{U_0}{U_{RF}}$$

Equation 2-15 synchronous phase

With U_0 being the energy loss per turn and U_{RF} being the effective RF voltage.
The **synchrotron frequency** υ_s can be calculated as follows[23]:

$$\upsilon_s = \frac{1}{2\pi}\sqrt{\frac{\nu_r h \eta_c e}{E}\frac{dU_{RF}}{d\psi_s}}$$

Equation 2-16 synchrotron frequency from RF slope

with h as the number of buckets, υ_r as revolution frequency and $\eta_c = \alpha - 1/\gamma^2$. For a pure sinusoidal RF field this can be transformed to

$$\upsilon_s = \upsilon_r \sqrt{-\frac{U_{RF} h \cos(\Psi_s)\eta_c}{2\pi E}}$$

Equation 2-17 synchrotron frequency for sinusoidal field

The synchrotron frequency becomes larger for larger RF voltage, larger RF frequency, larger synchronous phase and larger momentum compaction factor. It decreases with the energy and longer storage rings have smaller synchrotron frequencies. It has to be mentioned, however, that there is only a weak dependence on the parameters. Using harmonic cavities is a way to lower the synchrotron frequency. Looking to Equation 2-16 the effect comes from the flattening of the RF voltage slope at the synchronous phase. The slope can even be reduced to zero.

The **energy spread** is a synchrotron radiation equilibrium parameter, which only depends on the energy and the dipole distribution. At high single bunch intensities, however, there is a widening of the energy spread due to the microwave instability. This can be seen in the following figure:

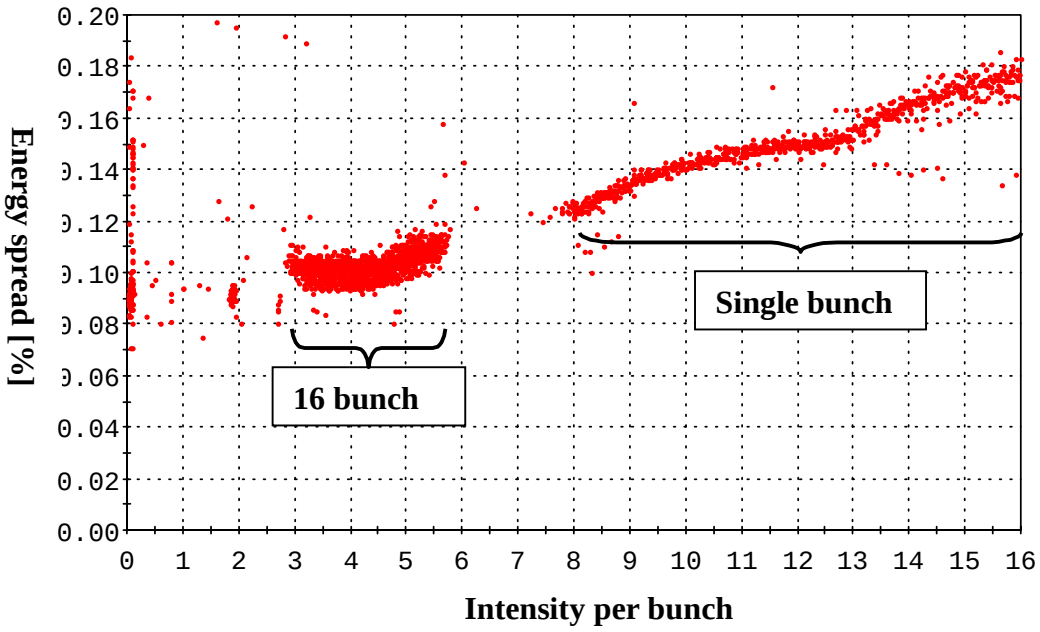

Figure 2-20 Energy spread as function of single bunch intensity

The energy spread was calculated from two beam size measurements at locations of different dispersion.

The natural energy spread Δp/p is an equilibrium from the excitation due to synchrotron radiation and the longitudinal synchrotron radiation damping. It determines the **natural bunch length** which can be calculated as follows:

$$\sigma_s = \frac{c\eta_c \cdot \Delta p/p}{2\pi\nu_s}$$

Equation 2-18 natural bunch length

As will be explained in the next chapter it might be useful to look for the maximum possible bunch length. There are three ways to influence the natural bunch length:

- the synchrotron frequency ν_s
- the momentum compaction factor η_c
- the energy spread $\Delta p/p$

At the ESRF the effective RF voltage and the energy spread are the only parameter which vary according to the different filling patterns. Harmonic cavities to lengthen the bunch are, however, now used or planned on several smaller energy third generation light sources.

Trying to increase the momentum compaction is in principle possible. To achieve this without an increase of the emittances is, however, rather difficult. It would require larger dispersion outside the bending magnets while maintaining small dispersions within the bending magnets.

There is also a bunch lengthening due to the interaction of the electrons with the vacuum chamber wall[24]. The created field is reducing the slope of the effective RF voltage at the synchronous phase and therefore lengthening the bunch. The bunch length for different single bunch intensities was measured at the ESRF with a streak camera. The result is shown in Figure 2-21.

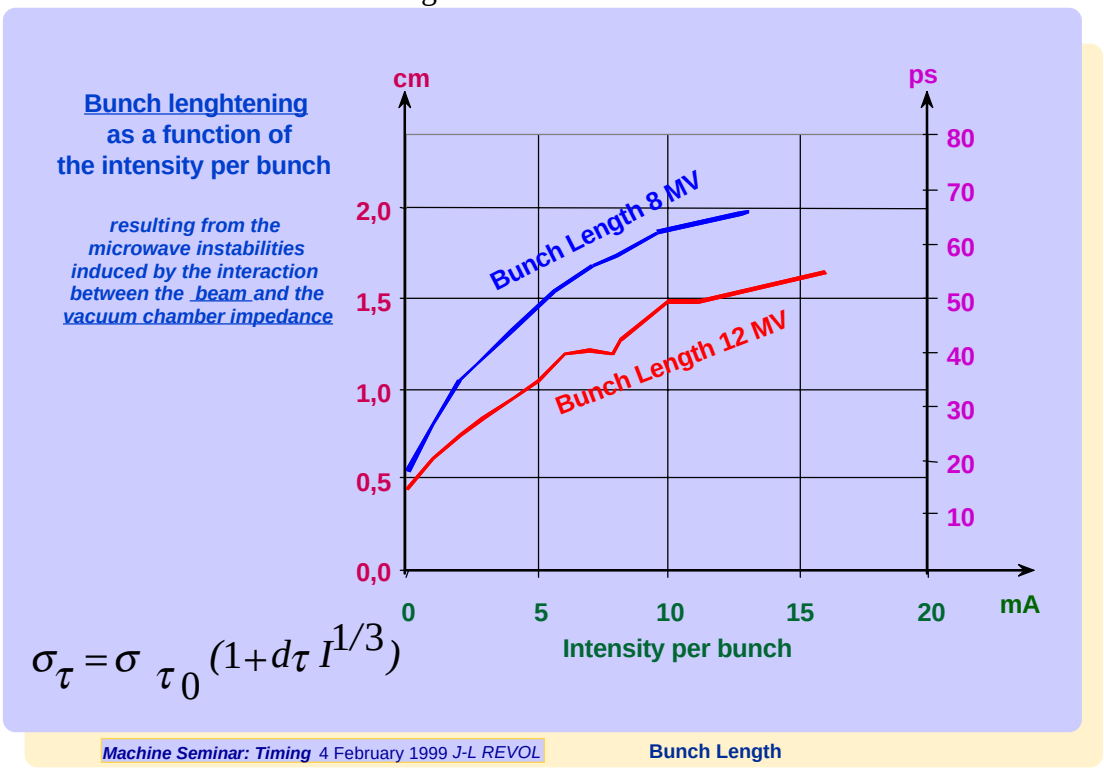

Figure 2-21 Bunch length as function of single bunch intensity
The influence of the RF voltage on the bunch length can be clearly seen.

2.8 Machine Dedicated Time

At least one day per week is reserved for studies to maintain and increase the performance of the machine as well as for accelerator related studies. This time is the so-called Machine Dedicated Time "MDT". Major study work is done on lattice, beam position stability, injection process, low energy potential, diagnostic tools, coupling, on high intensity single bunch behaviour and on mastering beam losses. A lot of work is always dedicated directly to the beam delivery: the repair of equipment, the upgrade of filling procedures, the verification of the ID effect on the beam, diagnostic verification and beam delivery tests. The distribution of MDT between the different groups involved is shown for the year 1998 in Figure 2-22.

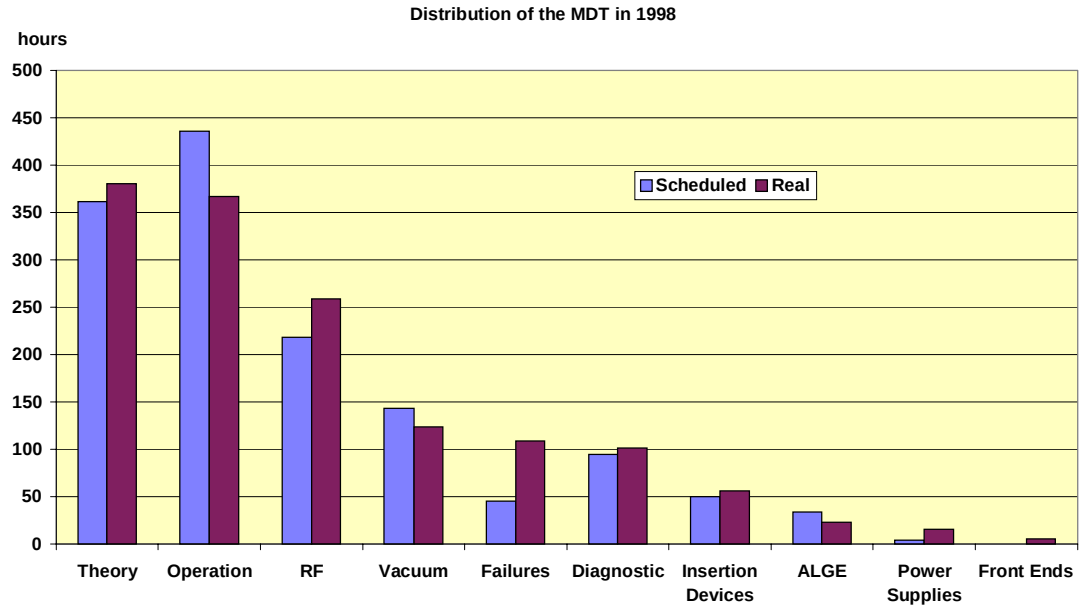

Figure 2-22 Distribution of MDT between the different groups

By nature all this work causes a lot of beam losses. In principle beam losses during MDT are not different from those during normal operation but they are more difficult to quantify. To get a more quantitative figure of the MDT losses it was decided to monitor the amount of electrons passing by the transfer line to the storage ring. Although the electrons may not be immediately lost after the injection this gives the best long-term view of the total amount of electrons lost in the storage ring. Monitoring the electrons passing by the transfer line is also the only way to take into account the injection losses.

The electrons pass through a fast current transformer in the transfer line and the current and the integrated charge are stored in the historical database. They are afterwards attributed to the different MDT topics. The result of this shown in the next figure:

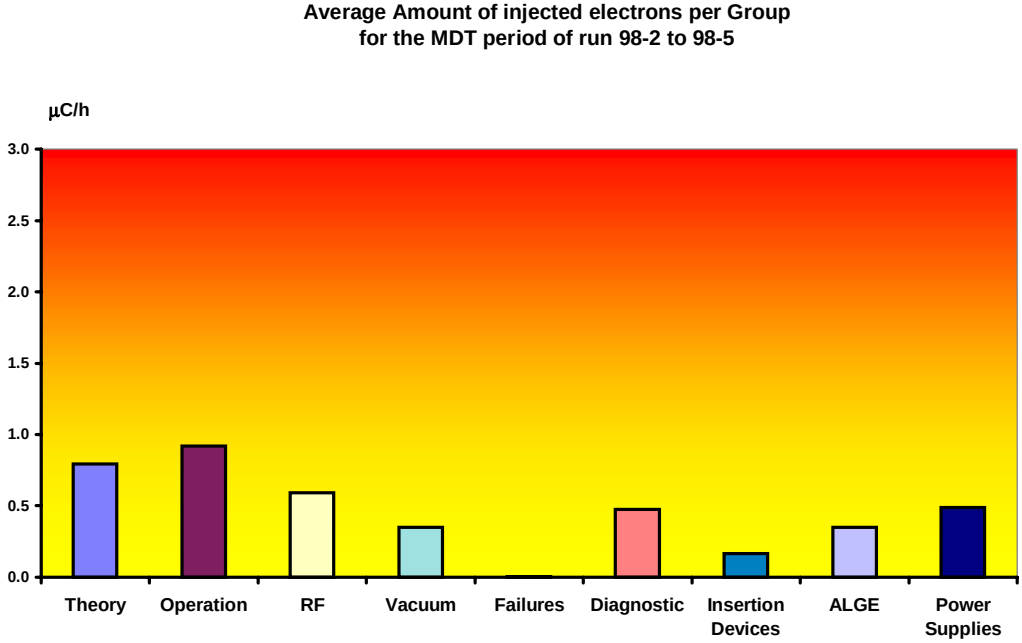

Figure 2-23 Electron Losses for the different MDT topics

An important fact in discussing beam losses is that the Front Ends are generally closed during MDT. Consequently there is very little radiation on the beam lines even for higher beam losses.

2.9 Radiation Considerations

2.9.1 General shielding geometry

There are two major sources of radiation at the ESRF:

- the synchrotron radiation itself in the X-ray regime
- the radiation created by electron losses

To avoid exposure of persons with synchrotron radiation the beam line hutches have a specific shielding[25]. The shielding assures a low radiation level outside the hutches and consists of lead with a thickness from 12 mm to 35 mm. This is necessary due to the high photon energy and intensity of the synchrotron radiation at the ESRF. The ESRF Beamline Personnel Safety System was build to avoid that persons enter into the hutches while there is still synchrotron radiation inside[26].

The accelerator complex is shielded with concrete walls and a concrete roof to avoid irradiation of persons following electron losses. Similar to the beamlines access to the tunnel is restricted by the Machine Personal Safety System (PSS). The external tunnel wall was built out of 1m thick heavy concrete whereas the inner tunnel wall is 1.3 m thick and built with normal concrete. Two layers of 0.5 m thick concrete blocks make up the tunnel roof. The shielding geometry with the exception of the tunnel roof can be seen in figure 2-3. The two concrete layers of the tunnel roof can be seen in Figure 2-9.

2.9.2 Radiation limits in the experimental hall

The experimental hall of the ESRF is classed as a free access zone. As a consequence the ESRF personnel is classed as non-exposed and the corresponding annual dose is limited to 5 mSv. Given a yearly working time of 2000 hours this means that the dose rate in the experimental hall has to be kept below 2.5 μSv/h.

Due to a new European Directive[27], which will be applied from May 2000 on the annual dose in free access, zones will be reduced to 1 mSv. To maintain the experimental hall a free access zone the dose rate will therefore be limited to 0.5 μSv/h.
Additionally the neutron quality factor will be multiplied by two.
Many studies were carried out by the safety group to develop a radiation monitoring system, which enables to measure such low dose rates. Based on this appropriate shielding and interlocks can be used which prevent from too high dose rates[28].

2.9.3 Injection Limitation

Based on radiation measurements it was calculated by the safety group that the equivalent of 3 μC electrons lost per hour would limit the dose rate outside the tunnel in all places to a maximum of 2.5 μSv/h. To assure the free access dose rate limitations of the Experimental Hall it was therefore decided to limit the amount of available electrons to be injected to this value and to provide an interlock on the LINAC. For practical reasons (MDT organisation by half shifts) the limit was set on fixed 4-hour periods per day to 12 μC.

Applying the new dose rate limit of 0.5 μSv/h including the new quality factor for neutrons the amount of available electrons is proposed to be lowered to 1.4 μC for a 4-hour period. This has to be compared to the electron charge of 0.57 μC in one 200 mA filling. Therefore only two injection per 4-hour period would be allowed.
As this may be too restrictive and could be detrimental to the smooth delivery of beam to the users, it was decided to install a set of neutron monitors on the tunnel roof and to associate the injected current limitation to real dose measurements. In such a manner, local shielding would help releasing the safety constraint.
These devices will be described in chapter 5.3.4.

2.10 Summary

As one can see the machine and consequently the beam losses have significantly changed during the last years. In order to keep the overview only two machine situations will be discussed. The first one will be called the initial situation and represents the machine in summer 1996. The second will be called recent situation and represents the machine in summer 1999. The changes in between were mainly driven by beam loss considerations. The main characteristics are

Parameter	Initial situation	Recent situation
Optic	4nm	Low vertical beta
Minimum vertical gap in high beta straight section	11 mm	8 mm
Minimum vertical gap in low beta straight section	9 mm	8 mm
Main filling pattern	200 mA 1/3-filling	200 mA 2 x 1/3-filling
RF voltage	8 MV	12 MV
Scraper position	ID6 and cell 5	ID6 and cell 22
Killing in hybrid mode	Yes	No
Available amount of electrons during 4 hours	No limit	12 μC
Septum sheet position	13.5 mm	19.5 mm

Table 2-11 Machine status in summer 1996 and summer 1999

3. Electron Loss Mechanisms

This chapter starts with the description of the different beam loss origins and the energy acceptance. They are qualitatively well known and the points specific to the ESRF will be emphasised. The second part of the chapter is dedicated to the quantification of the losses.

3.1 Injection Losses

Injection is a major issue regarding beam losses. At APS, for example, where a continuous topping up of the storage ring intensity was done, detailed calculations for radiation protection during injection were necessary[29].

During standard injection the equivalent of 5 nC electrons per second is injected into the storage ring. This means that the actual 4-hour limit of 12 μC is reached after about 2400 seconds or 40 minutes. In other words only 40 minutes of standard injection speed can be allowed over a 4-hour period. This works without problem during USM but limits some injection intensive machine studies.

If the injection efficiency is known it is possible to calculate the contribution of the injection losses compared to the total number of losses. For a standard operation value of 80 % injection efficiency 20 % of all losses come from injection. The injection losses can be divided into two categories: losses due to a transverse mismatch of the injected beam and losses due to the longitudinal capturing process.

3.1.1 Transverse Mismatch of injected beam

The injected beam has to be matched to the storage ring optic in position, angle, size and divergence at the exit of the septum to optimise injection efficiency. Angle and position have to be adjusted once per run in both the horizontal plane and the vertical plane, due to closed orbit drifts in the booster. However, as the incoming beam is injected off-axis in the horizontal plane, it experiences large betatron oscillations during the first turns before being damped. betatron oscillations[16]. If the amplitude of these oscillations exceeds the transverse acceptance the particles are lost.

A reduction of the vertical acceptance by reducing the chamber aperture might lead to a reduction in injection efficiency and an increase of losses due to injection. This effect was measured at SRS and was one argument to fix their minimum inner aperture at 15 mm[30]. Injection is also taken into account for machines currently at the design level such as SOLEIL[31]. At the ESRF a calculation of the aperture limitations due to injection[32] as well as measurements of injection efficiency versus vertical aperture were carried out[33]. No reduction of injection efficiency down to 6 mm inner aperture was measured. The measurements were carried out for different vertical beta functions in the high beta straight section[34 35].

Although the peak performance of injection efficiency is not affected by small gap chambers, efficiency was found to reduce within a few weeks due to mismatching of the injected beam[15]. This can be explained due to closed orbit changes in the booster following slow magnet drifts caused by ground motions. No orbit correction can be applied to the booster at extraction energy. Therefore all changes of the uncorrected closed orbit directly change the transfer path to the storage ring.

3.1.2 Longitudinal Capturing

In the longitudinal plane the injected beam have also to be captured. The injected electrons have to be in phase and at the same energy as the stored electrons, if not they start synchrotron oscillations. If the mismatch is greater than the RF energy acceptance they continuously lose energy[36] [37]. The longitudinal phase space situation during injection is sketched for two different RF voltages in the following graph:

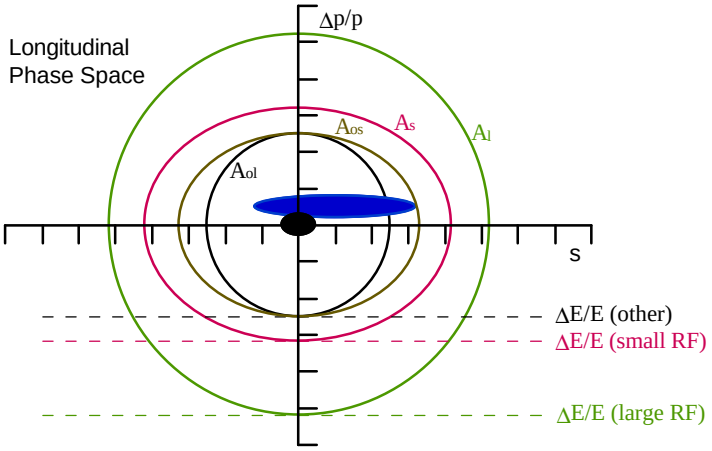

Figure 3-1 the longitudinal phase space during injection

The axis are chosen in arbitrary units to only show the principle. The black ellipse in the centre represents the stored beam. The blue ellipse represents an injected beam which is mismatched in phase and energy. One should note that although the energy spread of the injected beam is the same as the one of the stored beam the bunches are much longer in the booster due to the larger momentum compaction factor.

Lets compare the longitudinal phase space for two RF voltages U_1 and U_s. The green ellipse A_l is the region of electron capture for the large RF voltage U_1. For a smaller RF voltage U_s this region reduces to the red ellipse A_s. Not only the energy acceptance is reduced in this case but also to a lesser extend the phase or longitudinal acceptance.

As will be discussed later in this chapter the energy acceptance might also be limited by transverse or beam dynamic effects. This has some impact on the longitudinal acceptance. Lets assume a smaller energy acceptance (black) than the RF energy acceptance coming from the RF voltage Us. This will lead to acceptance A_{ol} in the case of the RF voltage U_1 and to the acceptance A_{os} in the case of the RF voltage U_s. The phase acceptance in this case is smaller for the higher RF voltage due to fact that a larger RF voltage leads to larger energy offsets for electrons which are injected with a phase offset. The maximum longitudinal acceptance for a given transverse or dynamic energy acceptance is therefore reached when the RF voltage just supplies the same energy acceptance.

At the ESRF the energy matching between the booster and the storage ring was measured several times and found to be in the range of 0.2 %[38] [39]. Once optimised by the use of a streak camera no problems were encountered with the longitudinal capturing.

3.2 Lifetime limiting processes

The different contributions to the lifetime of a stored beam in a storage ring have already been discussed for a long time[40] [41]. The effects contributing to the lifetime were calculated for the ESRF[42]. More recent work was done to correctly include coupling in the Touschek lifetime as well as to improve the calculation of the energy acceptance[43] [44] [45]. The effect of scattering on thermal photons was discussed for LEP[46]. Recent work has been carried out to quantify the ESRF energy acceptance and the lifetime components[47] [48].

3.2.1 Elastic gas scattering

Due to residual gas in the vacuum chamber the electrons in the storage ring might hit a molecule. There are two principle effects: the electron might be deflected without loosing energy but getting a deflecting angle or an energy transfer takes places to the molecule. The first effect is called elastic gas scattering and can be described by Coulomb scattering.

For stored electrons the scattering on the nuclei is much stronger than on the shell electrons. Therefore the formula for Rutherford scattering can be used:

$$\frac{d\sigma}{d\Omega} = \left(\frac{r_e Z}{2\gamma\beta^2} \right)^2 \frac{1}{\sin^4(\frac{\Theta}{2})}$$

Equation 3-1 Rutherford cross section

with the scattering angle Θ, $d\Omega = 2\pi \sin(\Theta) d\Theta$, the nucleus charge Z, the electron radius r_e and the relativistic parameters γ and β.

For small angles one obtains the differential cross-section

$$\frac{d\sigma}{d\Theta} = 8\pi \cdot \left(\frac{r_e Z}{\gamma\beta^2} \right)^2 \cdot \frac{1}{\Theta^3}$$

Equation 3-2 Rutherford cross section for small angles

The density of the residual gas can be expressed by $n_j = \sum_i \alpha_{ij} \cdot \frac{p_i}{kT}$ with p_i as partial pressure of gas i, k as Boltzmann constant, T as absolute temperature and α_{ij} as number of atoms j per molecule i. This finally results in the formula for the elastic gas scattering lifetime per plane

$$\frac{1}{\tau_{x,z}} = \frac{2\pi r_e^2 c}{\gamma^2 \beta^3 kT} \frac{1}{A_{x,z}} \sum_{atom\, j} \left(Z_j^2 \cdot \sum_{gas\, i} \alpha_{ij} \left\langle \beta_{x,z} p_i \right\rangle \right)$$

Equation 3-3 elastic gas scattering lifetimes

$A_{x,z}$ are the horizontal and vertical acceptances. Lifetime is proportional to transverse acceptance or to the square of the aperture at the aperture limiting point. Therefore

installing smaller gap ID chambers significantly reduces the vertical elastic gas scattering lifetime.

After several years of operation at the ESRF high pressure zones are limited to intervention zones, i.e. due to leaks or new installed vacuum vessels. After a machine shutdown period during which several vacuum interventions have been carried out the total lifetime rises with vacuum conditioning over several weeks until it stabilises. As an example of vacuum conditioning, the lifetime and the average pressure are shown for the first six weeks of run 98-4:

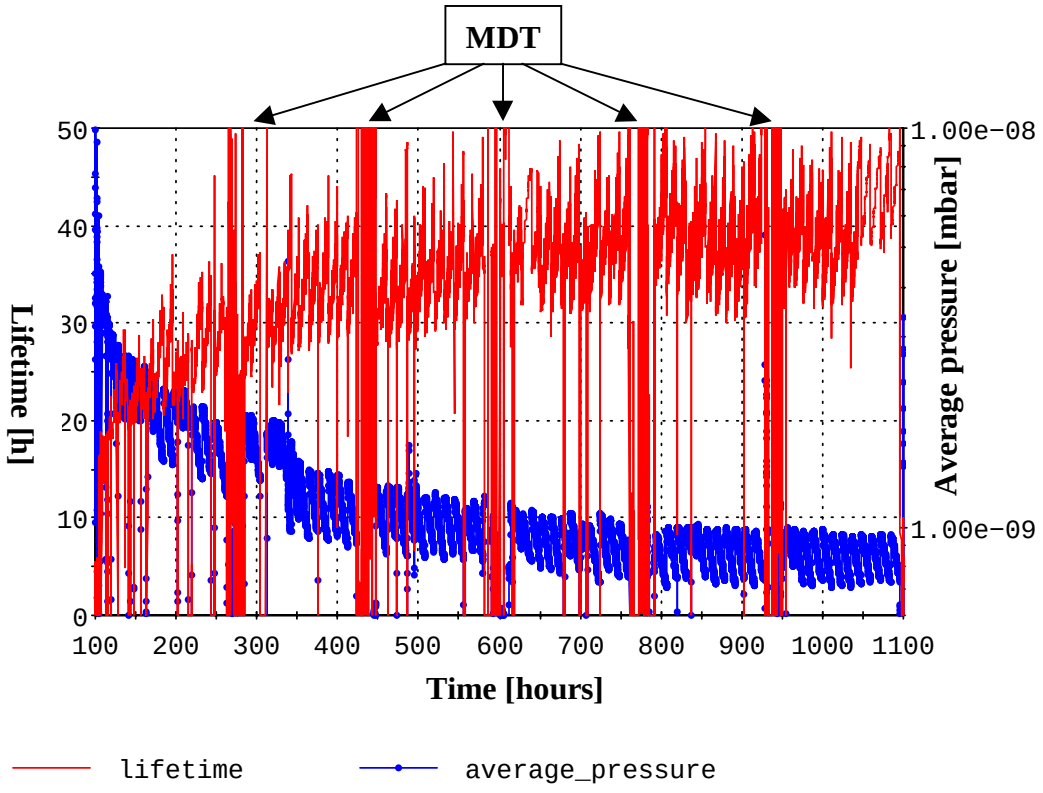

Figure 3-2 Vacuum conditioning and lifetime increase during run98-4

The six weeks of USM were delivered in 2/3-filling and interrupted by five MDT days. As can be seen the lifetime was 20 hours at 200 mA at the beginning of the run and reached 40 hours at the end. Since there were less installations of new vacuum vessels the record lifetime of 65 hours at 200 mA was reached at the end of a run 99-5 with an average pressure of less than 8 10^{-10} mbar.

It is also important to discuss the gas composition. Following a vacuum intervention the fraction of methane, carbonmonoxide and carbondioxide is higher than after conditioning[49]. This makes a scaling of the elastic gas scattering lifetime with simply the average pressure impossible. The same rule applies when a leak is developing. This can be seen in the following figure:

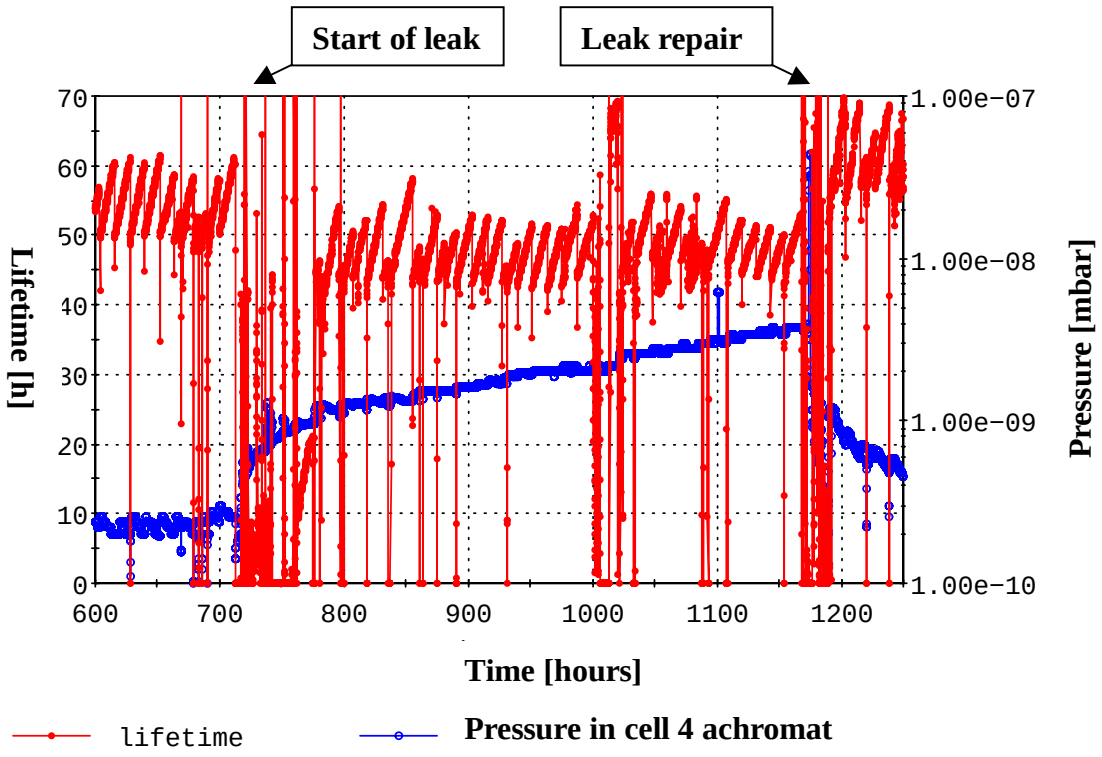

Figure 3-3 Leak development in cell 4 in run99-1

The local vacuum pressure and the lifetime are shown over the period where the leak developed.

It is difficult to develop a model of the gas composition along the beam axis. This has several reasons. The first reason is that the gas composition is time dependent after interventions until vacuum conditioning is finished. Additionally the pumping of methane and argon is different for NEG pumps and ion pumps leading to variations depending on the pumping set up. To have a vacuum profile model which can be used for lifetime calculations the resolution along the axis has to be good with respect to the change of beta function. At the ESRF there are only one to two residual gas analyser and seven pressure gauges per cell which is not sufficient in this respect. Therefore no vacuum profile model which is consistent with elastic gas scattering lifetime measurements is available at the moment.

Looking to Equation 3-3 one can see that it is the combination of high pressure and high beta function in the vertical plane which is the most detrimental to the lifetime. From Figure 2-2 and Figure 2-5 one can see that this is the case for interventions on dipole chambers. There are only two vacuum valves per cell upstream and downstream the straight section chambers. In case of a vacuum intervention the full length between these two valves will go under atmospheric pressure and has to be reconditioned with beam. A quantitative discussion of the lifetime will be given at the end of the chapter.

3.2.2 Inelastic gas scattering

When electrons hit residual gas atoms they sometime lose energy by emitting photons. The resulting radiation is called gas bremsstrahlung. The photons have opening angles the range of $1/\gamma$ in the forward direction [50]. They have broad band spectrum reaching up to the full electron energy. If the energy loss of the electron exceeds the energy acceptance the electron is lost.

The differential cross section for a photon emitted in the energy range between E_b and $E_b + dE_b$ can be expressed by[42].

$d\sigma = \frac{4 r_e^2 Z^2}{137} F(E, E_b) \frac{dE_b}{E_b}$ with the function $F(E,E_b)$ from the Bethe-Heitler formula

$$F\left(E, E_b\right) = \left[\frac{4}{3}\left(1 - \frac{E_b}{E}\right) + \left(\frac{E_b}{E}\right)^2\right] \ln \frac{183}{Z^{1/3}} + \frac{1}{9}\left(1 - \frac{E_b}{E}\right)$$

Equation 3-4 Bethe-Heitler formula

The lifetime resulting from this process can be calculated by

$$\frac{1}{\tau_b} \cong \frac{4 r_e^2 c}{137 kT}\left(-\frac{4}{3}\ln\left(\Delta E / E\right) - \frac{5}{6}\right) \sum_{atom\, j}\left(Z_j^2 \ln \frac{183}{Z_j^{1/3}} \sum_{gas\, i} \alpha_{ij}\, p_i\right)$$

Equation 3-5 inelastic gas scattering lifetime

with $\Delta E/E$ as energy acceptance of the machine which will be discussed later in this chapter.

The dependence on the gas composition and the local pressure are identical to the elastic gas scattering. The lifetime is independent of the aperture and the beta functions but slightly dependent on the energy acceptance.

The bremsstrahlung created due to inelastic gas scattering is an important radiation problem after vacuum interventions. In case of an intervention in a straight section the bremsstrahlung can leave the tunnel via the open Front End of the corresponding beam line. Straight section in this respect means the full length between the two dipoles. Since the opening angle and the direction of the bremsstrahlung are very similar to the synchrotron radiation ones there is a high probability for passing by the Front End. Beam lines are prevented from operation when the level of bremsstrahlung exceeds 2.5 µSv/h outside the optics hutches. Usually this is the case for a few weeks after an intervention. The exact time depends on the vacuum intervention, the beam line set up and the beam line shielding. A quantitative discussion of the lifetime will be done at the end of the chapter.

3.2.3 Touschek lifetime

Electrons perform oscillations in the longitudinal plane as well as in the transverse plane. If the electron density in a bunch is high the number of collisions between the electrons become significant. The transverse oscillations dominate since the horizontal betatron frequency of 13 MHz and the vertical betatron frequency of 5 MHz are far above the synchrotron frequency of only 2 kHz. If a collision takes place a part of the momentum will be transferred into the longitudinal plane. Assuming a smaller vertical

emittance than the horizontal emittance, the collision are mainly coming from the horizontal movements. If the resulting energy change exceeds the energy acceptance then the two electrons will be lost. If one assumes a flat beam one can calculate the Touschek lifetime[42]:

$$\frac{1}{\tau_t} \cong \frac{N r_e^2 c}{8\pi\sigma_x\sigma_z\sigma_s\beta^3\gamma^2(\Delta E/E)^3} D(\nu)$$

Equation 3-6 Touschek lifetime

$$\nu = \frac{(\Delta E/E)^2 \beta_x^2}{\gamma^2\sigma_x^2}$$

Equation 3-7 ν parameter

$$D(\nu) = \frac{\sqrt{\nu}}{2}\left[-3e^{-\nu} + \nu\int_\nu^\infty \frac{\ln u}{u} e^{-u} du + (3\nu - \nu\ln\nu + 2)\int_\nu^\infty \frac{e^{-u}}{u} du\right]$$

Equation 3-8 function $D(\nu)$

with the number of electrons N in the bunch, the horizontal beam size σ_x, the vertical beam size σ_z and the bunch length σ_s.

The function D(ν) is plotted for ν varying from 0.0001 to 10.

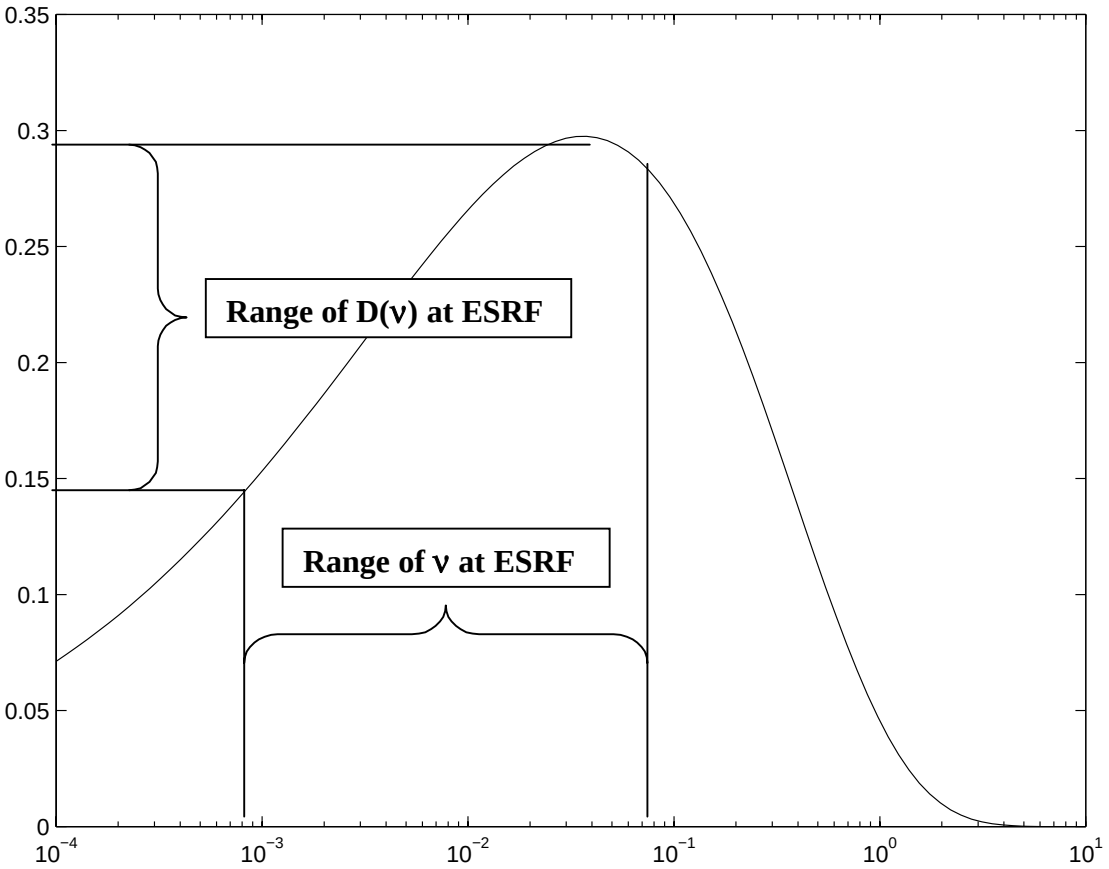

Figure 3-4 D(ν) as function of ν

At the ESRF ν varies between 0.0008 and 0.08 along the ring for an energy acceptance in the range of 3 %. The extrema are both reached in the low beta straight section where the horizontal beta function reaches its maximum and minimum values.

The Touschek scattering is the most important lifetime limitation in third generation light sources due to the small bunch volumes, which are achieved. It is therefore useful to discuss each parameter entering into Equation 3-6.

The **energy** comes in quadratically. This is the reason why low energy machines suffer most from this effect.

The lifetime goes down with the **intensity per bunch**. At the ESRF the intensity per bunch is 55 times higher in the single bunch mode than in 2/3-filling mode, which makes this mode completely dominated by the Touschek scattering. This explains the smaller lifetimes for the high intensity per bunch modes, which are listed in **Table 2-8**. Since the high intensity per bunch is also required for storage ring FELs the Touschek lifetime will be very small in the corresponding machines.

The **bunch length** was already discussed before. It is, however, worth to mention that the installation of harmonic cavities on several third generation light sources was mainly driven by Touschek lifetime considerations.

The **horizontal beam size** is given at any location by

$$\sigma_x(s) = \sqrt{\varepsilon_x \cdot \beta_x(s) + D_x{}^2(s) \cdot \left(\Delta p/p\right)^2}$$

Equation 3-9 horizontal beam size

In most of the cases the contribution from the dispersion and the energy spread can be neglected. The horizontal emittance is a synchrotron radiation equilibrium parameter, which is also influenced by optics. It a can be used to increase the Touschek lifetime but as it is a key parameter in the brilliance one normally tries to minimise it. The emittance scales quadratically with the electron energy. As a consequence going to lower energies for a given storage ring will add this effect to the already existing direct energy dependence.

The horizontal beta function has to be small in the dipoles to minimise the horizontal emittance. In the straight sections it is optimised for the beam lines. At the ESRF there is, however, a request to switch several straight sections from low beta to high beta. This is in terms of Touschek lifetime certainly the good direction. For future machines with even smaller horizontal emittances and beam sizes it might therefore be useful to only go for high beta straight sections.

The **vertical beam size** can be calculated to be

$$\sigma_z(s) = \sqrt{\varepsilon_z \cdot \beta_z(s) + D_z{}^2(s) \cdot \left(\Delta p/p\right)^2}$$

Equation 3-10 vertical beam size

The vertical dispersion is generally very small since horizontal magnetic fields are only coming from second order effects as vertically off centred closed orbit in quadrupoles and sextupoles and rotated dipoles. Therefore the contribution of the dispersion and the energy spread can be generally neglected.
The vertical emittance comes from the coupling of the horizontal motion into the vertical direction via magnetic and closed orbit errors. The following relations can be used:

$$\kappa = \frac{\varepsilon_z}{\varepsilon_x}, \quad \varepsilon_z = \frac{\kappa}{1+\kappa}\varepsilon_{x0}, \quad \varepsilon_x = \frac{1}{1+\kappa}\varepsilon_{x0}, \quad \varepsilon_{x0} = \varepsilon_x + \varepsilon_z$$

Equation 3-11 coupling parameter

with ε_{x0} as natural horizontal emittance.

Normal values for the coupling of modern light sources are 1%. Using corrector magnets for coupling correction enabled the coupling to be reduced to 0.3 % at the ESRF[51]. The corresponding vertical emittance is 12 pm. In operation conditions 0.25% to 1.5% coupling are served since only few beam lines take profit from the small vertical emittance and in high intensity bunch mode it helps to increase the Touschek lifetime. At the ESRF the vertical emittance is close to the diffraction limit of the photon beam. For future light sources with even smaller emittance the coupling might therefore need to be increased.

The vertical beta function has to be optimised in straight sections for vertical acceptance reasons. In the rest of the cell it is usually already large so that no optimisation can be expected in this respect.

The **energy acceptance** will be discussed in chapter 3.3. It is clear that this is the ideal parameter to increase the Touschek lifetime as there is a strong dependency on it and there is no detrimental effect to the users. A lot of effort is therefore spent in this direction for new projects[44] [45].

Finally the function D(ν) can be discussed. For ν < 0.01, i.e. the large beam size case one can approximate D(ν) by

$D(\nu) \cong \sqrt{\nu}(-\ln\nu - C - 1.5)$ with the Euler constant $C = 0.577215$. D(ν) is therefore proportional to the inverse of the horizontal beam size. It therefore increases the influence of the beam size.

Between 0.01 and 0.1 D(ν) reaches its maximum and is rather constant. Variations of ν in this range are practically without influence on the lifetime.

With ν above 0.1 D(ν) decreases again. For large ν one can do the following simplifications:

$$\int_{\upsilon}^{\infty} \frac{e^{-u}}{u} du \to \frac{e^{-\upsilon}}{\upsilon}, \quad \int_{\upsilon}^{\infty} \frac{\ln(ue^{-u})}{u} \to \ln(\upsilon)\frac{e^{-\upsilon}}{\upsilon}$$

Equation 3-12

Taking only the driving terms simplifies D(ν) to

$$D(\upsilon) = \frac{1}{2}\upsilon^{3/2}\ln(\upsilon)e^{-\upsilon}$$

Equation 3-13 D(ν) for large ν

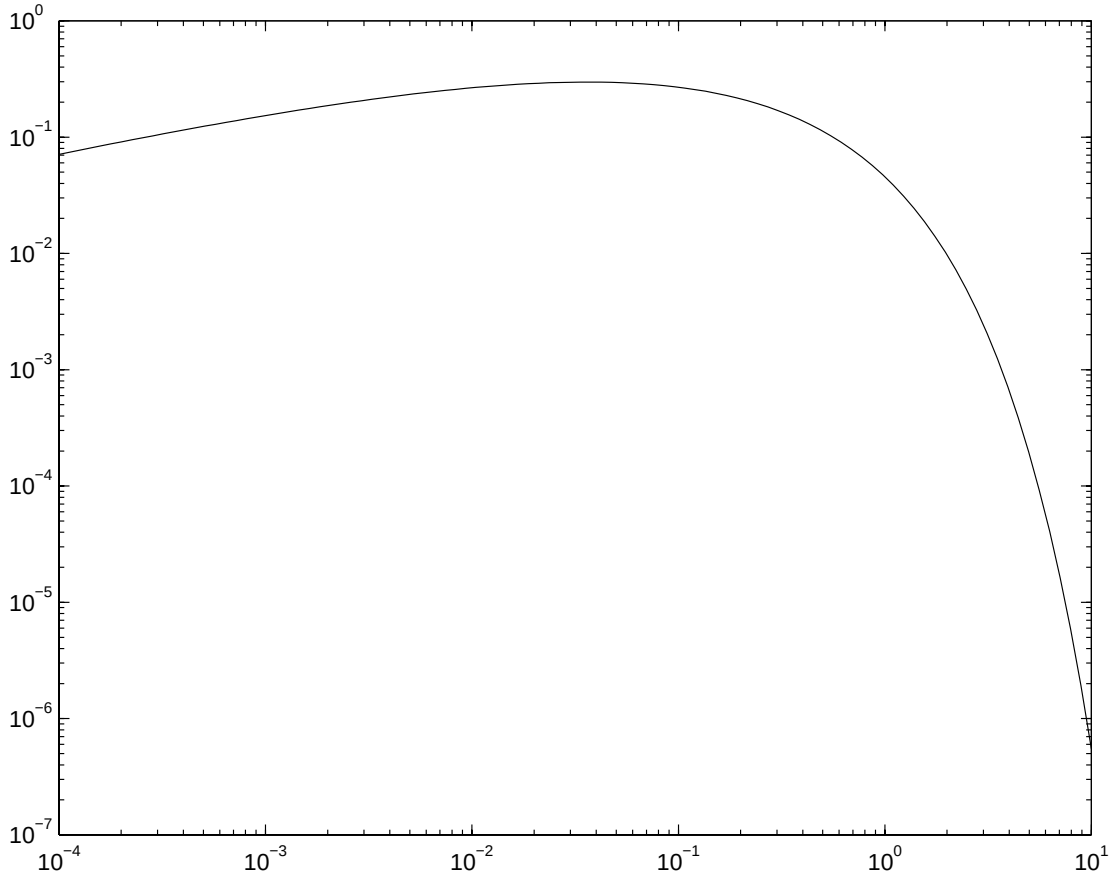

Figure 3-5 D(ν) as function of ν in double logarithmic view

The exponential dependence on ν can be seen in Figure 3-5 and will finally lead to an increase of the Touschek lifetime for even smaller beam sizes[52]. The present light sources are still far from this region. For future light sources with much smaller horizontal beam sizes, however, values of ν much larger then the 0.1 can be reached as can be seen in the following table:

Energy [GeV]	3	3	3	3
Emittance [m rad]	$4\cdot10^{-11}$	$4\cdot10^{-11}$	$4\cdot10^{-11}$	$8\cdot10^{-11}$
Hor. beta [m]	10	10	2.5	10
Energy accept.	0.04	0.03	0.04	0.04
Resulting ν	11.1	6.2	2.8	5.6

Table 3-1 ν as function of emittance, beta function and energy acceptance

The physical explanation why at very low emittances and therefore very high electron densities in a bunch the Touschek lifetime can increase is the following: the electron loss rate is proportional to the number of electron collisions and to the probability that these collisions throw the electrons out of the energy acceptance. The number of collision increases with larger electron density. The probability that these collisions

result in an electron loss (which is expressed by D(ν)), however, decreases. This can be explained by the fact that for very small horizontal emittances and large horizontal beta functions the transverse momentum of the electrons becomes so small that the probability to create a large momentum transfer becomes very small also.

To resume the discussion one can list again how a Touschek lifetime optimised future light source should look like
- high number of bunches
- harmonic cavities for bunch lengthening
- large momentum compaction factor for a given emittance
- very small emittances to achieve large ν
- high energy acceptance
- full coupling
- low energy to achieve large ν

Numbers for the Touschek lifetime at the ESRF will be given at the end of this chapter.

3.2.4 Compton scattering

The stable stored electrons can also suffer from scattering on photons. When too much energy is transferred to the photons the electrons will leave the energy acceptance and will be lost. At the ESRF there are two kinds of photons likely to interact with the beam: the overall present thermal photons and laser photons coming from the experiment GRAAL. This experiment takes advantage of Compton back scattered photons from the electron beam which have an energy which extends into the GeV region hereby enabling nuclear physics reactions. An agreement, by contract, authorises this experiment to reduce the beam lifetime by a maximum of 20 %.

The differential Compton cross section can be written as

$$\frac{d\sigma_c}{d\Omega} = \frac{r_e^2}{2} \cdot \left[1 + \cos^2\Theta + x + 1/x - 2\right] \cdot x^2$$

$$\text{with } x = \left[1 + \frac{\gamma E_{ph}}{m_e c^2} \cdot (1 - \cos\Theta)\right]^{-1}$$

Equation 3-14 differential Compton cross section

with r_e as classical electron radius, m_e as electron mass and E_{ph} as incoming photon energy[46].
The minimum x is given by

$$x_{\min} = 1 - 4\gamma \frac{E_{ph}}{m_e c^2}$$

Equation 3-15

The mean photon energy in Compton scattering is boosted by a factor γ^2 compared to the mean initial photon energy. Assuming a temperature of 40°C the mean thermal photon energy 2.7 kT is 0.073 eV. This leads to x_{min} = 0.993 at the ESRF. In this case

one can approximate the Compton cross section by the Thompson cross section for elastic scattering, i.e. x=1:

$$\frac{d\sigma_c}{d\Omega} \to \frac{d\sigma_t}{d\Omega} = \frac{r_e^2}{2} \cdot \left(1 + \cos^2 \Theta\right)$$

Equation 3-16 Thompson cross section

The loss rate due to Compton scattering can then be expressed by

$$\frac{1}{\tau_c} = \rho_\gamma \cdot c \cdot f \cdot \sigma_t$$

Equation 3-17 Compton scattering lifetime

with ρ_γ as photon density, $\sigma_t = \frac{8\pi}{3} r_e^2$ as Thomson cross section and f as the fraction of the scattering which results in a beam loss.

The number of thermal photons in a volume V within the frequency span ν and ν + dν can be calculated from the Planck formula to be:

$$dn = \frac{8\pi V}{c^3} \frac{\nu^2 d\nu}{e^{h\nu/kT} - 1}$$

Equation 3-18

The photon density $\rho_\gamma = n/V$ can then be expressed by

$$\rho_\gamma = 8\pi \left(\frac{kT}{hc}\right)^3 \int_0^\infty \frac{x^2}{e^x - 1} dx$$

Equation 3-19 thermal photon density

with h as Planck constant and k as Boltzmann constant. The integral can be calculated as

$$\int_0^\infty \frac{x^2}{e^x - 1} dx = \Gamma(3) \cdot \zeta(3) \cong 2.404$$

Assuming that all scattering on thermal photons at room temperature would lead to a beam loss (f=1) one can calculate the lifetime to be about 22 hours. This is general for all accelerators. Fortunately only collisions leading to photon energies larger than the energy acceptance of the electrons lead to electron losses. It is therefore necessary to calculate the energy spectrum of the photons. The mean final photon energy is boosted by a factor γ^2 compared to the initial photon energy. This leads to a mean final photon energy following scattering on thermal photons at the ESRF of about 10.2 MeV or 0.169 % of the electron energy.
In order to calculate the part of scattering which leads to beam losses one must calculate the part of the photons which receive more energy from the electron than the electron can afford due to the limited energy acceptance. The calculation can be done

bearing in mind that the relevant photons are a great deal above the mean thermal energy.

$$\int_a^\infty \frac{x^2}{e^x - 1} dx \Rightarrow \text{for } a >> 1 \quad \int_a^\infty x^2 \cdot e^{-x} dx = \left[- e^{-x} \cdot \left(x^2 + 2x + 2 \right) \right]_a^\infty$$

Equation 3-20

For a final photon energy of 3 % of the electron energy or 181.2 MeV the initial photon energy is 1.297 eV. This is the equivalent of 48 kT or a = 48. This gives the integral $\int_{48}^\infty \frac{x^2}{e^x - 1} dx = 3.42 \cdot 10^{-18}$, which means that these photons are so rare that no lifetime limitation at the ESRF can be expected of them.

It is the γ^2 boost of the photons, which makes the scattering on thermal photons only important at very high energies. This is the reason why the LEP lifetime is limited by this effect[46].

3.2.5 Quantum lifetimes

So far only lifetime components where the electrons are lost due to a single scattering process have been discussed. Only effects contribute where the probability of single scattering beyond the acceptance limit is sufficiently high. The effect of synchrotron radiation on the lifetime is quite different. The probability of creating a synchrotron radiation photon of 180 MeV (about the energy acceptance of the storage ring) is very small. The number of photons with energies much higher than the critical energy goes down with $\exp(-E_{ph}/E_c)$ with E_{ph} as photon energy and E_c as critical energy. The critical energy at the ESRF reaches 100 keV for the high field super conducting wavelength shifter at 4 T magnetic field. The suppression factor is therefore exp(-2000) and makes this event impossible.

However, as the amount of synchrotron radiation photons emitted is very high it can be asked if a chain of many events might push the electron out of acceptance. This effect has, however, to be fast enough to overcome the radiation damping process which damps down all longitudinal and transverse motions with a damping time of the range of 10 ms at the ESRF. The method to calculate this effect takes advantage of the quantum statistical character of synchrotron radiation that results in a Gaussian distribution of the equilibrium beam size and bunch length. From the conditions at the border of the acceptance it is possible to calculate the flux leaving the stable region and directly from this, the lifetime which is called the quantum lifetime. The process can be described in both the longitudinal and the transverse plane.

The different lifetime components can be calculated by[42]:

$$\frac{1}{\tau_{qt}} = \frac{1}{\tau_{x,z}} \cdot \frac{A_m}{\varepsilon_{x,z}} \exp\left(-\frac{A_m}{2 \cdot \varepsilon_{x,z}}\right)$$

Equation 3-21 transverse quantum lifetimes

with

τ_{qt}	horizontal (vertical) quantum lifetime
$\tau_{x,z}$	horizontal (vertical) damping time
A_m	horizontal (vertical) acceptance
$\varepsilon_{x,z}$	horizontal (vertical) equilibrium emittance

$$\frac{1}{\tau_{ql}} = \frac{1}{\tau_s} \cdot \frac{(\Delta E / E)^2}{(\Delta p / p)^2} \exp\left(-\frac{(\Delta E / E)^2}{2 \cdot (\Delta p / p)^2}\right)$$

Equation 3-22 longitudinal quantum lifetime

with

τ_{ql}	longitudinal quantum lifetime
τ_s	longitudinal damping time
$\Delta E / E$	energy acceptance
$\Delta p/p$	equilibrium energy spread

Generally one can say that the quantum lifetime can be neglected if the transverse acceptance value exceeds forty times the emittance value and the energy acceptance exceeds six times the energy spread. In which case the quantum lifetime exceeds 100 h.

Taking the values for the recent machine situation from Table 2-2, Table 2-7 and Table 2-6 we get:

Plane	Acceptance	Emittance or energy spread	Acceptance to emittance Ratio
Horizontal plane	$11 \cdot 10^{-6}$ m rad	$4 \cdot 10^{-9}$ m rad	2750
Vertical plane	$3.2 \cdot 10^{-6}$ m rad	$40 \cdot 10^{-12}$ m rad	80000
Longitudinal plane	0.03	0.0011	27

Table 3-2 Acceptance ratios for the different quantum lifetimes

Therefore the ESRF is far from being quantum lifetime limited.

3.2.6 Effect of many small scattering events

Following the discussion on quantum lifetime it could be questioned whether or not the effect of many small scattering events plays a significant role in touschek scattering, elastic gas scattering, inelastic gas scattering and Coulomb scattering on photons also. The model of the quantum lifetime holds as long as the excitation is based on small statistically independent pertubations. The scattering effects will add extra excitation terms leading to an increase of the equilibrium parameter as emittances and energy spread. As a consequence the corresponding quantum lifetime will be reduced.

A way to quantify the effect is to calculate the growth rate of a specific multiple scattering process and to compare it to the damping time. If the invariant increase is much slower than the radiation damping process no equilibrium invariant increase will take place and, consequently, no lifetime reduction due to this effect will occur.

For example, one can calculate the emittance growth rate for the multiple Coulomb scattering to be[42].

$$\frac{\delta\varepsilon}{\delta t} = 8 * \pi \frac{r_e^2 c}{\gamma^2 \beta^3} \ln \frac{183}{Z^{1/3}} \sum_{atom\ j} \left(Z_j^2 \sum_{gas\ i} \alpha_{ij} \left\langle \beta_{x,z}\, p_i \right\rangle \right)$$

Equation 3-23 emittance growth due to Coulomb scattering

Using the Equation 3-3 one can transform this to

$$\frac{\delta\varepsilon}{\delta t} = 4 \ln \frac{183}{Z^{1/3}} \frac{\varepsilon_{xm,zm}}{\tau_{x,z}}$$

Equation 3-24 emittance growth expressed by elastic gas scattering lifetime

The time to reach an emittance growth comparable to the acceptance can then be calculated as

$$T = \frac{\varepsilon_{xm,zm}}{\frac{\delta\varepsilon}{\delta t}} = \frac{1}{4 \ln \frac{183}{Z^{1/3}}} \tau_{x,z}$$

Equation 3-25

With a typical gas scattering lifetime of about 200 hours, the rise time is in the range of 10 hours. This is six orders of magnitude above the damping time of the betatron oscillations so that no emittance growth takes place and as a consequence no lifetime reduction.

Concerning multiple inelastic gas scattering, one can take advantage of the fact that the differential cross section is proportional to the inverse of the photon energy at bremsstrahlung photon energies much below the electron energy. This means for example, that emitting 10 photons of 0.3 % of the electron energy takes the same time as emitting one photon of 3 % of the electron energy. Therefore, the time that multiple inelastic gas scattering requires to add up to the energy acceptance is in the range of the single scattering lifetime. This is much more than the damping time and therefore this process can be neglected.

Multiple Touschek scattering is called intra beam scattering. Here one takes into account the exchange between the different planes. Detailed simulations with the ZAP code[53] were carried out at the ESRF to investigate this effect in view of running the ESRF at lower energies[54]. It was found that no significant emittance growth or energy widening can be found at energies above 3 GeV. Therefore additional beam losses due to this effect can be excluded.

Concerning Coulomb scattering on thermal photons it was calculated above that taking the full cross section for scattering on thermal photons the interaction time is many hours (lifetime would be about 22 hours). This is again long compared to the damping time and can therefore be neglected.

As a conclusion, one can say that the scattering effects leading to significant single scattering losses do not lead to a quantum lifetime reductions by adding the effect of many small scattering events. This is consistent with the fact that no emittance increase beyond the synchrotron radiation equilibrium emittance was measured at the ESRF.

3.3 Energy acceptance

From the discussion of the lifetime it is clear that the energy acceptance is a major input parameter for the dominant Touschek lifetime. It is therefore important to understand what is really limiting the energy acceptance.

3.3.1 Longitudinal energy acceptance

One limit comes from the longitudinal acceptance[55] and can be calculated by

$$\left(\frac{\Delta E}{E}\right)^2 = \frac{eU_{RF}}{\pi h \eta E q} F(q)$$

Equation 3-26

with $F(q) = 2\left(\sqrt{q^2 - 1} - \arccos(1/q)\right)$, $q = \frac{U_{RF}}{U_0}$ and the same notations as used in paragraph 2.7.

The beam loading leads to a modulation of the RF voltage around the average for non-uniform filling patterns[56]. The voltage drops along the bunch train so that the electrons at the end experience a significantly lower RF voltage than those at the beginning. Due to this the electrons at the end are confronted with a smaller energy acceptance than those at the beginning of the bunch train. At 200 mA this effect was measured to be about 0.9 MV in 1/3-filling and half of this in 2/3-filling.

Due to the interaction of the electrons with the vacuum chamber wall there are additional energy losses of the electrons. Calculation for the ESRF vacuum system, however, limits these losses to about 30 keV per turn in a 10 mA single bunch[57]. This means that this effect can be neglected compared to the radiation loss per turn.

The energy loss per turn of the electrons is 4.88 MeV from the dipole radiation. The additional losses due to the Insertion Device can be up to 0.6 MeV turn.

Taking the values from Table 2-1 and Table 2-3 one can calculate the following energy acceptances:

RF voltage [MV]	RF Modulation [MV]	ID losses [MV]	Min. Energy Acceptance	Max. Energy Acceptance
8	0.9	0.6	0.02	0.033
8	0.9	0	0.025	0.037
12	0.9	0.6	0.045	0.054
12	0.9	0	0.049	0.057
8	0.45	0.6	0.023	0.045
8	0.45	0	0.028	0.034
12	0.45	0.6	0.048	0.052
12	0.45	0	0.051	0.055

Table 3-3 Longitudinal Energy Acceptance for different RF settings

3.3.2 Energy Acceptance from physical aperture

A second restriction for the energy comes from the horizontal physical aperture. Taking the definition for the horizontal acceptance Equation 2-6 the energy acceptance can be calculated as the energy offset where the horizontal acceptance drops to zero:

$$A_x(\Delta E / E) = 0 \Rightarrow \frac{\Delta E}{E} = Minimum_s\left[\frac{d(s)}{D(s)}\right]$$

Equation 3-27 Energy acceptance from dispersion

With a standard vacuum chamber half aperture of 37 mm and the maximum dispersion of 0.3521 m this results in an energy acceptance of 10.6 %.

Using Equation 3-27 is not correct for particles where a betatron oscillation is excited by the scattering process. This is, however, always the case when the energy change takes place at a location with non-zero horizontal dispersion or its derivative. This can be seen in the following figure:

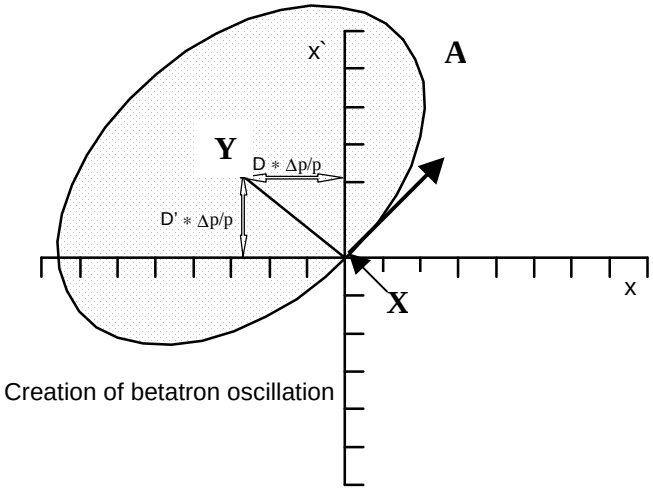

Figure 3-6 creation of betatron oscillation in presence of dispersion

The electron is arriving at the scattering point at the position X. Due to the energy loss its reference closed orbit which is the dispersion curve for its new energy is suddenly displaced to the point Y. Therefore the electron will start to rotate along the border of the ellipse A in the direction of the arrow.

Using the relations

$$x(s) = D(s)\cdot\frac{\Delta p}{p}, \quad x'(s) = D'(s)\cdot\frac{\Delta p}{p}$$

$$A = \gamma(s)\cdot x^2(s) + 2\alpha(s)\cdot x(s)\cdot x'(s) + \beta(s)\cdot x'^2(s)$$

A can be calculated to be

$$A = H(s) \cdot \left(\frac{\Delta p}{p} \right)^2$$

Equation 3-28 Betatron oscillation creation due to energy loss

with H(s) as the H-function

$$H(s) = \gamma(s) \cdot D^2(s) + 2\alpha(s) \cdot D(s) \cdot D'(s) + \beta(s) \cdot D'^2(s)$$

Equation 3-29 H function

The maximum position x the electron will reach at the location s following the scattering at location s_0 with the energy change $\Delta p/p$ is

$$x_{\max}(s) = D(s) \cdot \frac{\Delta p}{p} + \sqrt{H(s_0) \cdot \left(\frac{\Delta p}{p} \right)^2 \cdot \beta(s)}$$

Equation 3-30 oscillation amplitude after energy loss

From this one can derive the energy acceptance for a scattering at the location s_0 to be

$$\frac{\Delta E}{E}(s_0) = Min_s \left[\frac{d(s)}{D(s) + \sqrt{H(s_0) \cdot \beta(s)}} \right]$$

Equation 3-31 energy acceptance due to physical aperture

There are several items that are worth to highlight.

The energy acceptance limitation due to the physical aperture depends on **the H-function at the point of the scattering**. This makes the energy acceptance a local function. On the other hand the H function is only varying along the dipoles and is a constant everywhere else. A table of the H-function is given below.

Location	H(s) in 4 nm optic	H(s) in low ver. beta optic
High beta straight section	0.0004 m	0.0005 m
Low beta straight section	0.0020 m	0.0026 m
achromat	0.0045 m	0.0040 m

Table 3-4 H function at different locations and for different optics

The H-function is large in the achromats due to the large dispersion. The dispersion in the achromats can in principle be reduced with the drawback of increasing it in the straight sections.

The H-function is much larger in the low beta straight sections than in the high beta straight sections due to the strong focusing.

The corresponding energy acceptances for the two machine situations described in Table 2-11 are

Location	ΔE/E(s) in 4 nm optic	ΔE/E(s) in low ver. beta optic
High beta straight section	0.066	0.073
Low beta straight section	0.041	0.045
achromat	0.031	0.038

Table 3-5 Energy acceptance at different locations and for different optics

Since the H-function is very small in the high beta straight sections the energy acceptance is very large. The switch from low beta straight sections to high beta straight sections which was discussed for the Touschek lifetime would therefore go into the good direction.

The **dispersion and the horizontal beta function at the horizontal aperture limiting point** should be chosen as small as possible. At the ESRF both values increased when switching to the low vertical beta optic. The corresponding loss in energy acceptance could, however, be overcome by pushing the septum sheet further out.

3.3.3 Energy acceptance from dynamic aperture

The third restriction in the energy acceptance comes from the dynamic aperture. The dynamic aperture is the region of stable transverse motion of electrons taking into account all non linear effects at large amplitude as well as alignment and fabrication errors of the magnets.

The dynamic aperture plays an important role at the ESRF for the following reasons:
- The strong focusing of the ESRF lattice requires strong sextupoles for chromaticity compensation. This leads to strong non-linear fields far from the magnet axis.
- The high chromaticities listed in Table 2-9 lead to large tune shifts with energy offsets so that many resonances in the tune diagram are crossed.
- There is a large tune shift with betatron amplitude due to the strong non-linear fields.

At the ESRF several resonances are systematically corrected with corrector magnets to maintain a small coupling, small beta function beats and a high lifetime. The vertical half integer resonance was found to have the largest effect on the lifetime. This can be understood when looking to Figure 3-7 that shows the tune shifts with energy offset for the 4 nm optic and nominal chromaticity.

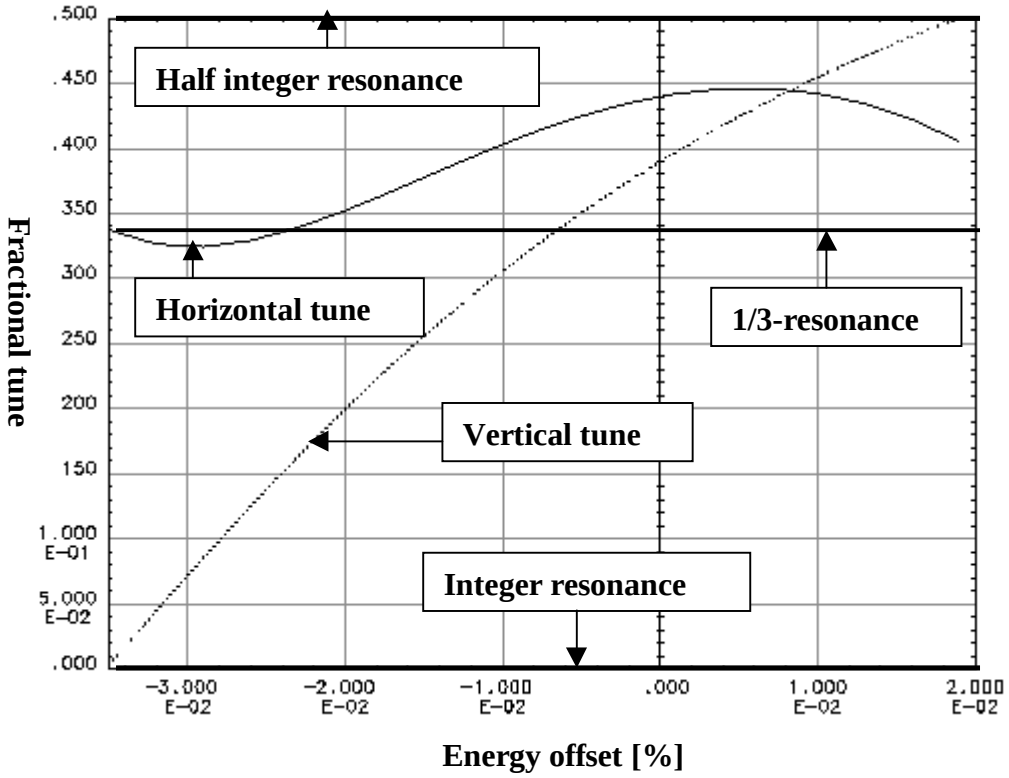

Figure 3-7 Tune shift with energy offset for the 4 nm optic

The dotted curve is the vertical tune, the other curve the horizontal tune. As can be seen the vertical half integer resonance is reached at about 2% energy offset, i.e. well within the limitations coming from the RF voltage or the physical aperture.

More recently it was shown that the point 0.333,0.333 in the tune diagram represents another severe dynamical aperture limitation[58].

From many measurements it is clear that electrons entering the integer resonance stop bands at the ESRF are lost. These stop bands limit the energy acceptance due to dynamic aperture for negative energy offsets. Figure 3-8 shows the tune shift with energy for two different sextupole tunings in the recent situation:

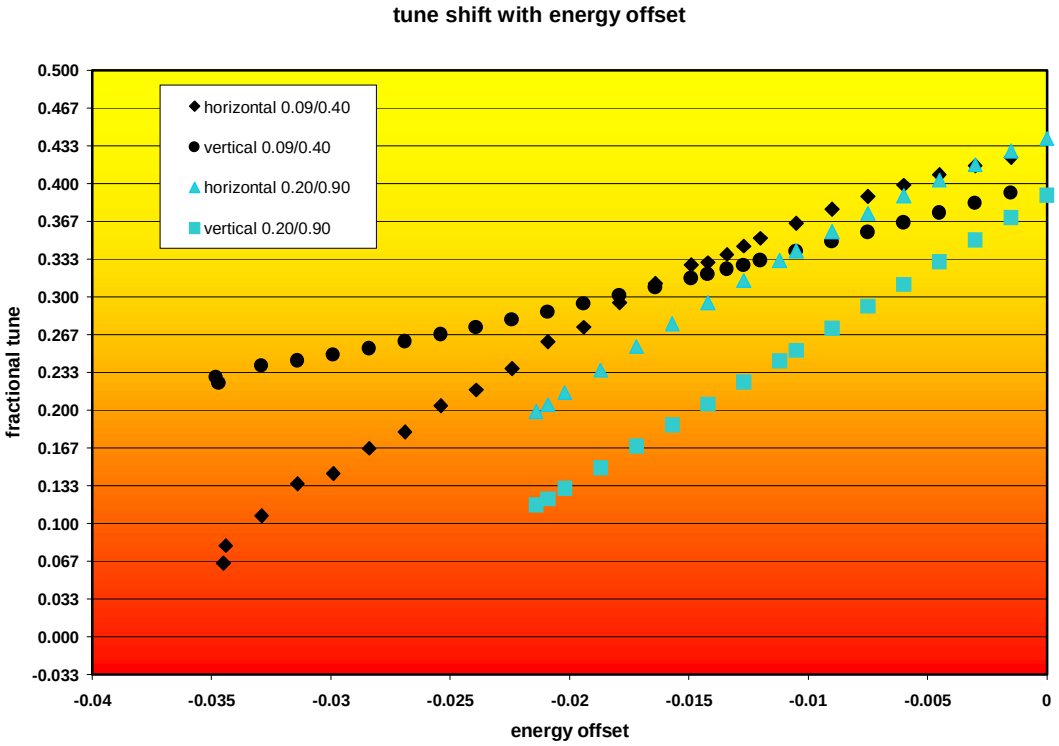

Figure 3-8 Tune shift with energy offset for different sextupole tunings with different chromaticities

The sextupole setting with the normalized chromaticities of 0.09 horizontal and 0.4 vertical is used during operation in the 2/3-filling mode. A horizontal normalized chromaticity of 0.2 and a vertical normalized chromaticity of 0.9 are used in single bunch operation at 15 mA. The values of the harmonic sextupoles are also different for dynamic aperture optimisation. The vertical and horizontal tune shifts as a function of energy offset were measured until the beam was lost on a resonance. The beam was lost in the small chromaticity tuning at –3.5% energy offset and a horizontal tune at 0.06. In the high chromaticity tuning the energy limit was reached at –2.1% and a vertical tune of 0.12. In both cases the vertical tune behaves very linear whereas the horizontal tune decreases faster when lowering the electron energy.

It is difficult to calculate the beam behavior far from the ideal orbit and energy due to the non-linear behavior. Additionally it is necessary to have a very good model of the machine imperfections to correctly describe resonances. For this reason no dynamic aperture model which is consistent with the lifetime measurements at the ESRF is available. One can, however, roughly estimate the energy acceptance when estimating the integer resonance stop band to 0.1 and a constant chromaticity all along the tune path down. This gives the following energy acceptances in the horizontal and the vertical plane:

$$\left(\frac{\Delta E}{E}\right)_x = \frac{0.34}{\xi_x} \text{ and } \left(\frac{\Delta E}{E}\right)_z = \frac{0.29}{\xi_z}$$

Equation 3-32 dynamic energy acceptance due to stop bands and chromaticity

For the chromaticities listed in Table 2-9 this gives the following table:

Single bunch intensity	Energy acceptance from vertical tune	Energy acceptance from horizontal tune
0.3 mA	0.048	0.11
5 mA	0.032	0.068
16 mA	0.022	0.049

Table 3-6 Energy acceptance limitation for different chromaticities

The different energy acceptances are illustrated for different machine situations in the following figures. An error of 10% was estimated on the physical aperture and the dynamic aperture. For the RF voltage the full span for the variation of ID losses and the effective RF voltage with beam loading is given.

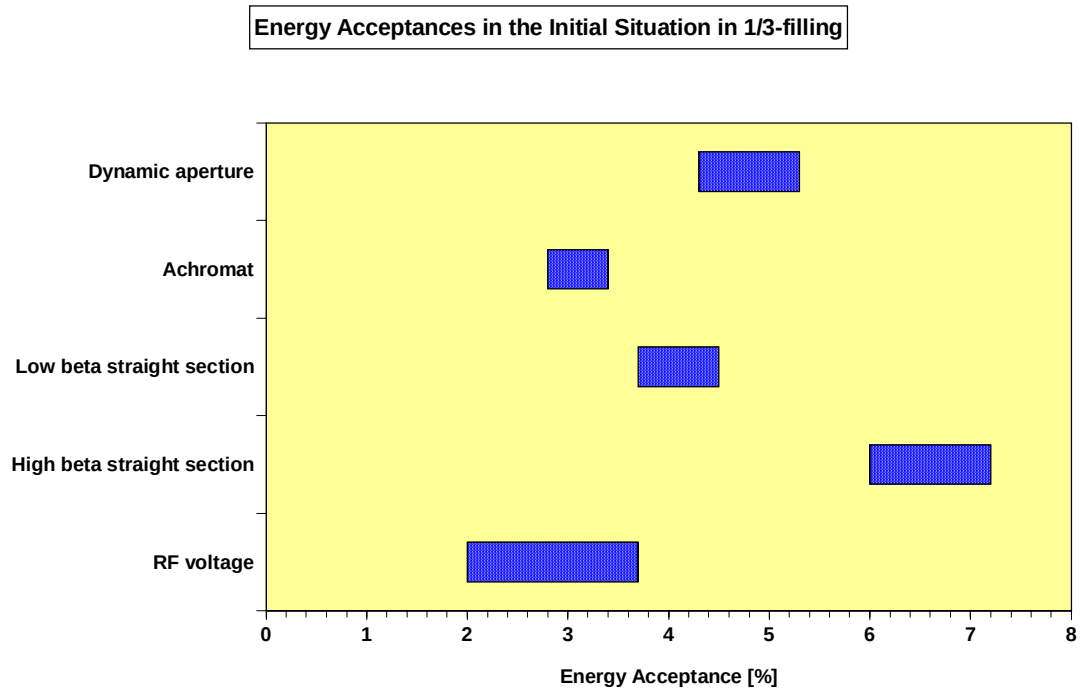

Figure 3-9 Energy Acceptance in the Initial Situation in 1/3-filling pattern

The RF voltage limitation to 8 MV was the energy acceptance limiting point in the Initial Situation. For particles at the beginning of the bunch train with higher effective voltage another limitation was coming from the physical aperture if the scattering took place in the achromat. The overall energy acceptance therefore varies between 2% and 3.7 %.

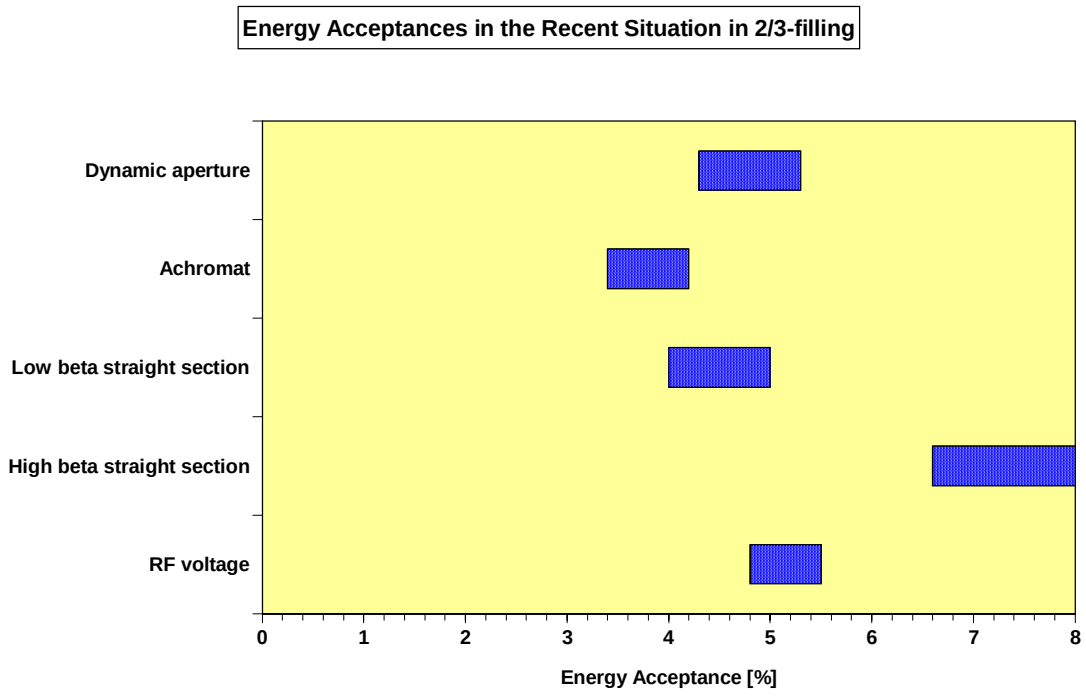

Figure 3-10 Energy Acceptance in the Recent Situation in the 2/3-filling pattern

Comparing the Recent situation with the Initial Situation one sees the beneficial effect of the RF voltage increase to 12 MV and the septum sheet displacement from 13.5 mm to 19.5 mm. In this situation it is the energy acceptance due to physical aperture which limits the energy acceptance in the achromats and the low beta straight sections. For energy losses in the high beta straight sections the RF acceptance and the dynamic aperture play the limiting factor. The overall energy acceptance therefore lies between 3.4 % and 5.4 %. **To further increase the energy acceptance requires a reduction of the dispersion in the achromat or a reduction of the horizontal beta function and dispersion in the high beta straight sections**. The next step lies in smoothing the optic in the low beta straight sections. Finally the dynamic aperture has to be increased.

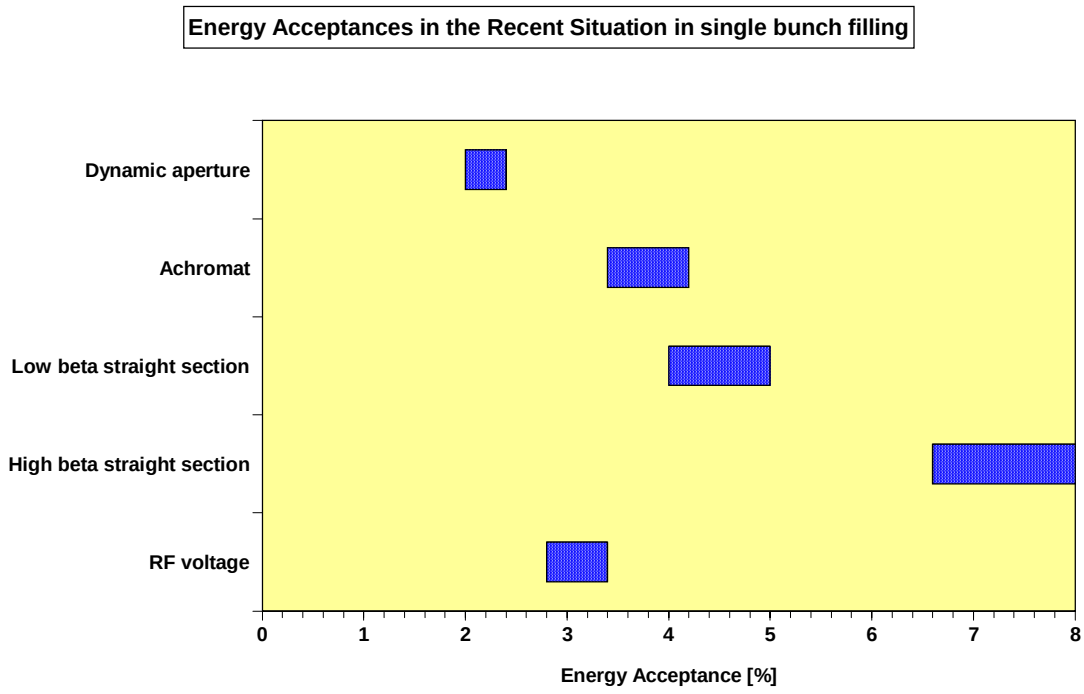

Figure 3-11 Energy Acceptance in the Recent Situation in single bunch filling pattern

In single bunch operation the energy acceptance is reduced to about 2.2 % by the dynamic aperture due to the large vertical chromaticity. This also explains why the RF voltage can be lowered to 8 MV without affecting the lifetime. **In this mode the only way to increase the energy acceptance is the reduction of the vertical chromaticity and/or a working point change**.

It is worth to discuss the energy acceptance for future light sources. For the same wavelength region of the synchrotron radiation smaller electron energies will probably be used following the recent development of small gap undulators. On the other hand the machine circumference will be increased to achieve smaller emittance. The use of damping wigglers will probably be necessary to achieve horizontal emittances close to the diffraction limit of the synchrotron radiation.
The energy loss per turn created in such a machine is not yet clear. Achieving sufficient energy acceptance from the RF is, however, only a question of money and space and will therefore be always achieved.
Lengthening the machine reduces the dispersion everywhere due to the smaller angle per dipole. On the other hand the use of damping wigglers will require zero dispersion at the place of the wiggler. Approaching the diffraction limit would require the horizontal beta function in the straight sections to be optimised to roughly half of the length of the straight section. This would with respect to the ESRF lower the horizontal beta function in the high beta straight sections and increases the horizontal beta function in the low beta straight section. Both changes are beneficial to the energy acceptance given by the physical aperture. **It can therefore be concluded that future light sources will have larger energy acceptances coming from the physical aperture**.
Increasing the circumference of the machine while maintaining the basic optic increases the tune. To avoid transverse single bunch instabilities it will probably be necessary to

increase the chromaticities[59]. Consequently the energy acceptance coming from the dynamic aperture will be decreased.
The dynamic aperture due to large tune drifts will very likely limit the energy acceptance of future light sources with energy offset. It will therefore be mandatory for future light sources to keep the chromaticities as low as possible.

3.3.4 Quantification

At last a quantification of the lifetime components can be made.
The intensity lost per time interval due to a loss process i is proportional to the loss rate and the intensity:

$$\left(\frac{\Delta I}{\Delta T}\right)_i = -\frac{I}{\tau_i}$$

Equation 3-33 intensity loss per time interval for one loss process

The total intensity lost per time interval is the sum off all individual losses:

$$\frac{\Delta I}{\Delta T} = -\frac{I}{\tau} = \sum_{all\ i}\left(\frac{\Delta I}{\Delta T}\right)_i = \sum_{all\ i} -\frac{I}{\tau_i} = -I\sum_{all\ i}\frac{1}{\tau_i}$$

Equation 3-34 total loss rate

The total lifetime can therefore be calculated as follows:

$$\frac{1}{\tau_t} = \sum_{all\ i}\frac{1}{\tau_i}$$

Equation 3-35 total lifetime

A quantification of the lifetime was done for the Initial Situation in 1/3-filling pattern. The following table shows the calculated lifetime for different assumptions of energy acceptance, average pressure and residual gas composition.

Parameter	Case 1	Case 2	Case 3	Case 4
Energy acceptance	0.0295	0.022	0.0295	0.022
Average pressure	$2\cdot10^{-9}$ mbar	$2\cdot10^{-9}$ mbar	$1\cdot10^{-8}$ mbar	$1\cdot10^{-8}$ mbar
Fraction of CO	0.1	0.1	0.2	0.2
Touschek lifetime	134 hours	62 hours	134 hours	62 hours
Inelastic gas scattering lifetime	404 hours	367 hours	45 hours	41 hours
Vertical elastic gas scattering lifetime	591 hours	591 hours	65 hours	65 hours
Horizontal elastic gas scattering lifetime	1880 hours	1880 hours	205 hours	205 hours
Total lifetime	82 hours	47 hours	20 hours	16 hours

Table 3-7 lifetime comparison for different cases

The low pressure settings with 10% fraction of CO in the residual gas represent the vacuum conditioned machine. Assuming $1\cdot10^{-8}$ mbar with 20% CO present is in line with the lifetimes measured after vacuum interventions. With conditioned vacuum the lifetime is limited by Touschek scattering. The typical total lifetime of 40 hours in that case is more in line with an energy acceptance of 2.2 % than with an energy acceptance

of 2.95%. Raising the RF voltage showed indeed a lifetime saturation at about 7.1 MV or 2.2 % energy acceptance.

The same table can be achieved for the Recent Situation in 2/3-filling

Parameter	Case 1	Case 2	Case 3	Case 4
Energy acceptance	0.034	0.025	0.034	0.025
Average pressure	$2 \cdot 10^{-9}$ mbar	$2 \cdot 10^{-9}$ mbar	$1 \cdot 10^{-8}$ mbar	$1 \cdot 10^{-8}$ mbar
Fraction of CO	0.1	0.1	0.2	0.2
Touschek lifetime	235 hours	93 hours	235 hours	93 hours
Inelastic gas scattering lifetime	425 hours	382 hours	47 hours	42 hours
Vertical elastic gas scattering lifetime	859 hours	859 hours	94 hours	94 hours
Horizontal elastic gas scattering lifetime	2874 hours	2874 hours	314 hours	314 hours
Total lifetime	123 hours	67 hours	25 hours	21 hours

Table 3-8 Lifetime in the Recent Situation in 2/3-filling

Case1 and Case 3 are calculated with the energy acceptance derived before for the Recent situation. Case 2 and Case 4 are calculated with an energy acceptance of 2.5% that is the one that is regularly found by scanning the RF voltage. The values of Case 2 and Case 4 fully agree with the lifetime measured in USM.

The fact that the ESRF energy acceptance is smaller than calculated in preceding paragraph comes very likely from a smaller energy acceptance due to dynamic aperture than estimated by the Equation 3-32. Studies are on the way to find the origin[60]. Part of the reduction can be explained with significant losses on the vertical half integer resonance or around the tune point 0.333/0.333.

Looking to the lifetime tables one can see that the Touschek lifetime is always dominating after the vacuum conditioning has taken place. From the losses created by the residual gas the largest fraction comes from the inelastic gas scattering and the vertical elastic gas scattering. The horizontal elastic gas scattering losses on the other hand never contribute to more than 10% to the total losses.

3.4 Quantification of Losses

It is useful to quantify the different loss origins with respect to the totality of the losses.

The first step is to separate the losses occuring during MDT from the one during USM. The share of total losses between MDT and USM can be calculated from the measurement of the number of electrons passing by the transfer line from the booster to the storage ring. As an example the history of the integrated TL2 intensity during the rune 99-1 is shown in the following figure:

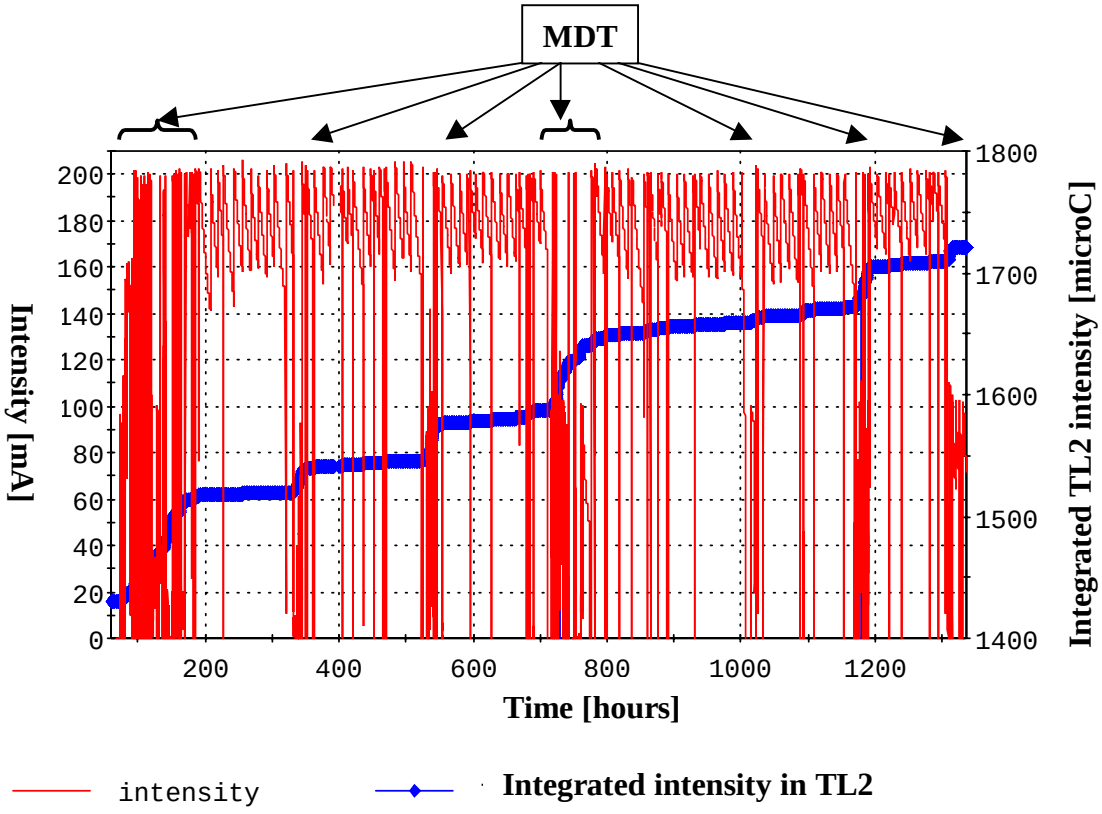

Figure 3-12 Integrated TL2 intensity during run 99-1

One can clearly see the steeper slope of the integrated TL2 intensity during the MDT period due to the different studies. The corresponding numbers are given in the following table

Run99-1	USM	MDT	TOTAL
Number of days	43	12	55
TL2 integrated intensity	60 µC	232 µC	292 µC
TL2 integrated intensity per 4 hour period	0.23 µC	3.22 µC	0.88 µC

Table 3-9 Integrated TL2 intensity during run 99-1

During run 99-1 80% of the losses were created during MDT. This figure varies from run to run. However, since the fraction of the run, which is MDT, is rather constant this value can be taken as a reference. Although the majority of losses takes place during MDT one has to keep in mind that losses are much more dangerous in USM during which the Front Ends are open.

For the USM delivery one can use the USM statistic to establish the share between the different beam loss origins. This was done for the Initial Situation using the USM statistic of 1996 and for the Recent Situation using the USM statistic of the first of 1999. The results are listed in the following figure:

Parameter	Initial Situation	Recent Situation
Number of USM days	220	233
Injection efficiency	80 %	80 %
Mean Time between failures	41 hours	28 hours
Touschek scattering USM	47 µC	41 µC
Inelastic gas scattering USM	26 µC	28 µC
USM vertical elastic gas scattering	16 µC	12 µC
USM horizontal elastic gas scattering	5 µC	4 µC
USM GRAAL losses	16 µC	15 µC
USM total lifetime losses	**110 µC**	**100 µC**
USM beam trips following failures	46 µC	76 µC
USM losses with Open Front End	**156 µC**	**176 µC**
USM active beam kills	38 µC	0 µC
USM injection losses	49 µC	44 µC
USM total losses	**243 µC**	**220 µC**
Lifetime losses per 4 hour period	0.08 µC	0.07 µC
Open Front End losses per 4 hour period	0.12 µC	0.13 µC
Total USM losses per 4 hour period	0.18 µC	0.16 µC

Table 3-10 USM losses in the Initial Situation and the Recent Situation

The total amount of lifetime losses was decreased by about 9 % during the last years although the USM time increased by 6 % and the inner vertical aperture in the Insertion Device vacuum vessels was decreased from 9 mm to 8 mm. The reduction was achieved by the change of the optic to gain vertical acceptance, the displacement of the septum sheet to gain horizontal physical aperture, the increase of the RF voltage to gain RF energy acceptance and the switch from 1/3-filling to 2/3-filling in standard filling mode to reduce the Touschek scattering.

Unfortunately the machine experienced a reduction of the Mean Time between Failures (MTBF) which increased the losses due to failures by about 65%. This results in the fact that the total amount of losses with Front Ends open which is the key figure for the beam line radiation problems was increased by 13%. The part of the equipment failures in this reaches now 45% with respect to 30% before.The beam kills in hybrid mode were suppressed so that together with the injection losses the total amount of USM losses could be reduced by 9%. To gain on the losses with open Front End the MTBF has to be improved and further optimisation of the filling patterns in terms of energy acceptance and lifetime to be carried out.

4. Electron Loss positions

An important step in the mastering of beam losses is the ability to predict the final collision point of the electrons with the storage ring vacuum chamber following, for example, a Touschek scattering. This knowledge is necessary for protection measures and to investigate radiation problems. This chapter sets on the main machine parameters that influence the beam loss position and links them to the different beam loss mechanisms. One important number in this respect is the fraction of electrons, which is intercepted by a vacuum chamber as a function of betatron amplitude and phase advance. The chapter ends with an overview of the different impact points of the electrons with the vacuum chamber.

4.1 General considerations

The first important parameter is the **travelling length of the electron from the loss origin point to the final collision point with the vacuum chamber**. Several different length scales can be defined.

As mentioned earlier a natural scale comes from the synchrotron radiation damping which is in the order of a thousand of turns. All processes that have growth lengths above this do not lead to losses. A second scale comes from the exploration of the betatron phase space by the electron for all phases. Depending on the fractional tune this is typically done within a few turns. Effects which have growing times longer than some revolution periods will only lead to losses on the acceptance limiting point since phase advances do not contribute anymore. This concerns most electrons with continuing energy loss outside the RF bucket or growing betatron amplitude on resonances.

The most complicated scale is where the losses occur within a few turns after the incident. These are large amplitude betatron oscillations following a scattering or coming from the injected beam. In this case the betatron phase advance between the beam loss origin point and the different physical apertures plays an important role.

The **source point** is also a matter of interest in the case of losses after less than a few turns where the phase advance plays an important role. Distributed source points as for the gas scattering and the Touschek scattering generally lead to distributed losses also. Injection losses in the transverse plane on the other hand are concentrated downstream the injection point as will be demonstrated later.

The **optical functions at the source point** are important as they determine the tolerance for different scattering processes. Large H-functions reduce the energy acceptance due to the physical aperture. Large beta function lead to small elastic gas scattering lifetimes.

The fourth important parameter is the **physical aperture distribution around the ring** and is important for losses occurring within a few turns. This can be illustrated by looking to Figure 2-15. The ID12 vacuum chamber is likely to intercept the electrons that jumped into the acceptance region between $2.2 \cdot 10^{-6}$ m rad and $4.1 \cdot 10^{-6}$ m rad following a scattering between cell 30 and cell12. ID14, ID16 and ID18 on the other hand receive much less electrons due to the probing of only 2 cells. A chamber

intercepts not all electrons since they might be at a betatron phase where the position is small and the angle large. A small fraction of electrons intercepted leads to a homogenous loss distribution. The fraction of electrons intercepted by a vacuum chamber will be discussed in paragraph 4.2. Generally one can, however, say that in order to avoid a lot of losses on one single vacuum chamber many chambers of the same aperture should be installed in the machine in a well-distributed manner.

The fifth parameter is the **kind of beam perturbation** that is created - whether it is an energy loss, a horizontal betatron oscillation, a vertical betatron oscillation or a combination of these. This was discussed in the presentation of the different beam loss origins.
Vertical elastic gas scattering losses will therefore lead to losses on small vertical gap vacuum vessels.
Horizontal elastic gas scattering will lead to losses on the septum sheet and for larger amplitudes everywhere at locations with large horizontal beta function. For the scattering creating energy losses as the inelastic gas scattering and the Touschek scattering: If the horizontal physical aperture limits the energy acceptance it is the septum sheet which will intercept most of the electrons. In the case of the limitation by the dynamic aperture the loss plane is determined by the kind of the resonance which is reached. This is illustrated in Figure 4-1 and Figure 4-2 that show the losses for the measurements already discussed in Figure 3-8.

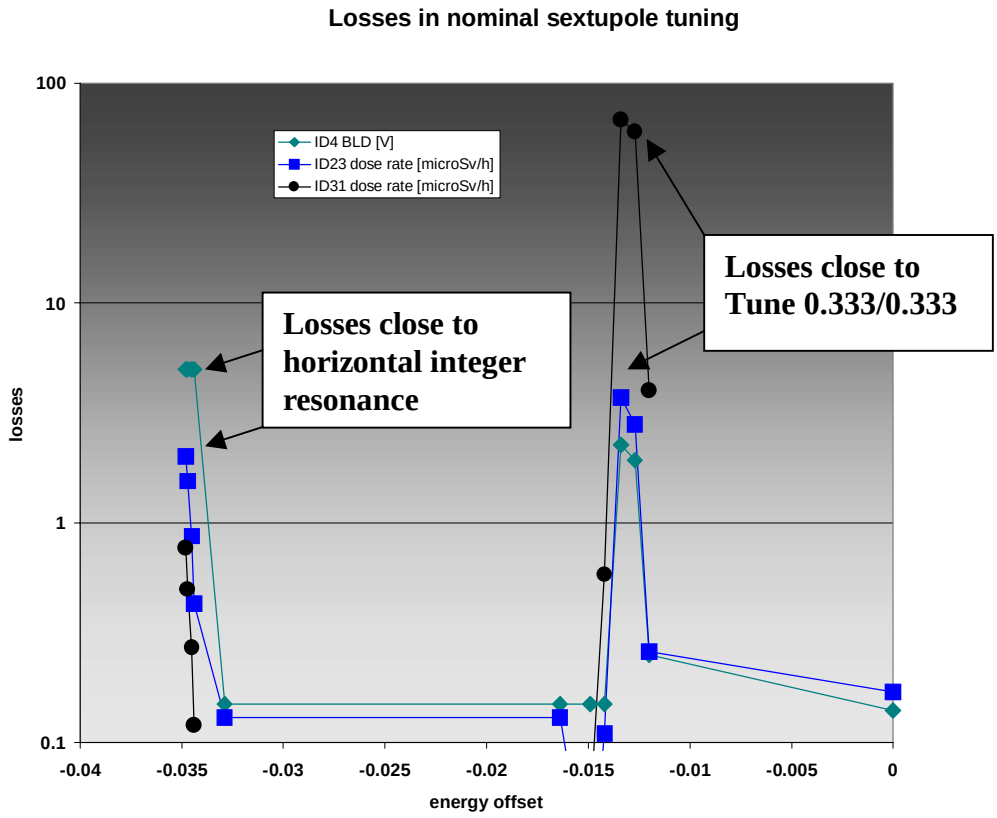

Figure 4-1 Losses on the resonances in nominal tuning

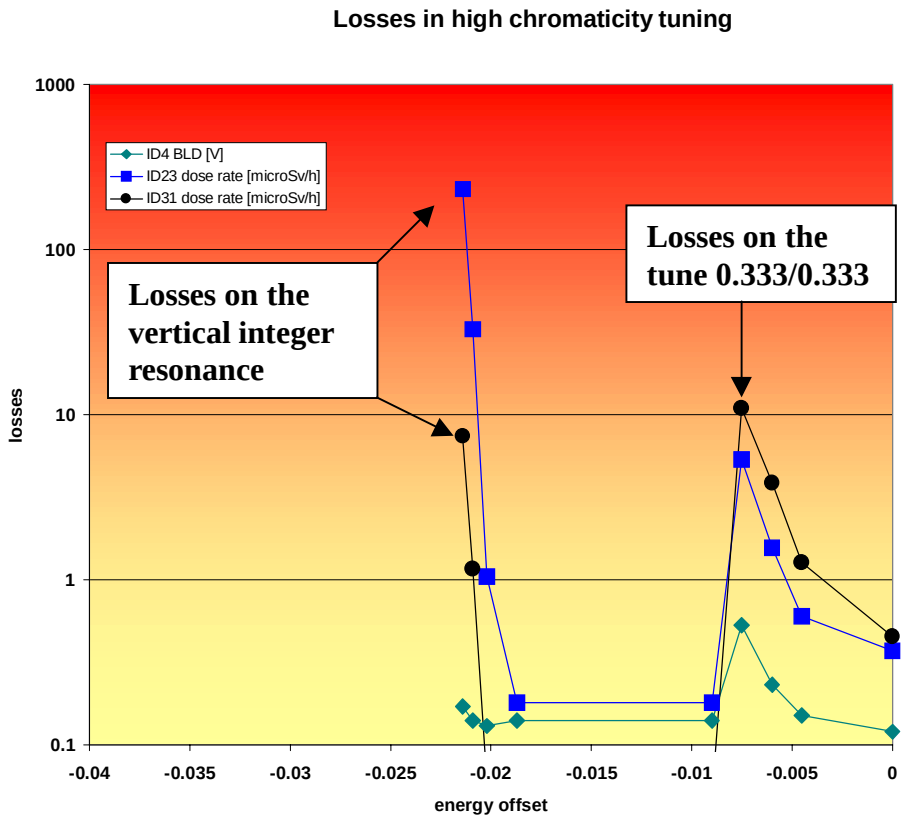

Figure 4-2 Losses on the resonances in high chromaticity tuning

The beam losses were measured with ionisation chambers and Beam Loss Detectors that will be presented in paragraph 5.3. It can be clearly seen that close to the horizontal integer resonance (-3.4 % in nominal sextupole tuning) the losses take place in ID4 ,i.e. on the septum sheet. On the vertical integer resonance (-2.1 % in high chromaticity tuning) the losses appear mainly on ID23 but also ID31 – the 8 mm inner vertical aperture vacuum vessels. The high beam losses at smaller energy offset were created due to the vicinity to the tune point 0.333/0.333. The losses at that tune are appearing in the vertical plane mainly on ID31.
If the RF voltage limits the energy acceptance the electrons will continue to lose energy until they reach the limit given by the physical aperture or the dynamic aperture. **In the case of a RF trip the energy loss is so slow that no betatron oscillation will be created. Consequently the electrons will be lost on resonances**.

To minimise losses on the small gap vacuum vessels it becomes clear from Figure 4-1 and Figure 4-2 that it should be avoided to limit the energy acceptance by a vertical resonance. The logic way to achieve this is to keep the vertical chromaticity small as it was already mentioned in paragraph 3.3.3.

4.2 Phase space scraping of a single vacuum chamber

In the preceding chapter it was shown, that it is important to know the fraction of the electrons, which is intercepted by a single chamber to derive the loss distribution on the different vacuum vessels. The betatron phase advance plays an important role for electrons that are lost within a few turns after the scattering event. The influence of the phase advance can at best be discussed by looking to the transverse phase spaces.

Choosing the middle of a straight section for displaying the phase space has the advantage that this is a symmetry point of the optic. The beam and acceptance ellipses are therefore symmetric with respect to the phase space axes.

4.2.1 Phase space of a single vacuum chamber

The first step to achieve this is to find the part of the phase space that is scraped by a single chamber. In Figure 4-3 several electron paths are drawn which are at the limit to hit the vacuum chamber wall of a small vertical aperture Insertion Device vessel.

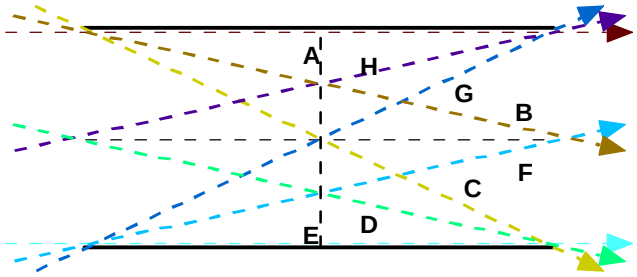

Figure 4-3 Extreme electron paths in an Insertion Device vacuum vessel.

For a chamber of the length 2D and a total inner aperture 2d one immediately gets the extreme positions and angles which are allowed to the electrons to pass by:

$$z_{\max} = d$$
$$z_{\min} = -d$$
$$z'_{\max} = d/D$$
$$z'_{\max} = -d/D$$

Equation 4-1 Extreme positions and angles in a vacuum chamber

One can now draw the different extreme electron paths into the vertical phase space in the middle of the straight section. This is done for an 11 mm inner aperture 5 m long vacuum chamber in Figure 4-4.

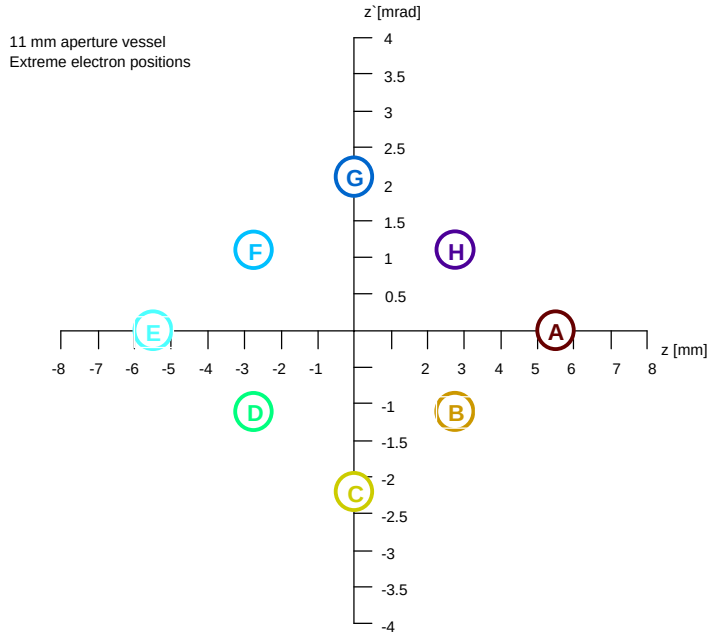

Figure 4-4 Vertical phase space for electrons with extreme paths

The electrons are grouped along four lines in the phase space:

$$z_1'(z) = \frac{1}{D}(z - d)$$

$$z_2'(z) = \frac{1}{D}(z + d)$$

$$z_3'(z) = -\frac{1}{D}(z - d)$$

$$z_4'(z) = -\frac{1}{D}(z + d)$$

Equation 4-2 Lines limiting the chamber acceptance

The four lines build together a frame, which is the border of the phase space region in which the electron will pass by the chamber. It has to be noted that this frame is only given by geometrical values and is therefore the same for whatever optic is used. The only assumption is that there is no magnetic field presents in the vacuum chamber that leads to deviations of the electron path. Using this frame to describe the vacuum chamber in the phase space has the advantage that the full chamber can be represented with only one figure. This helps a lot if one needs to represent several vacuum chambers at one location in the machine.

4.2.2 Optimum beta function in a straight section

The second step towards an estimation of the fraction of electrons that is intercepted is to draw the different acceptance into the phase space. This is done for a 5m long 11mm inner vertical aperture chamber in the 4 nm optic in Figure 4-5 and Figure **4-6.**

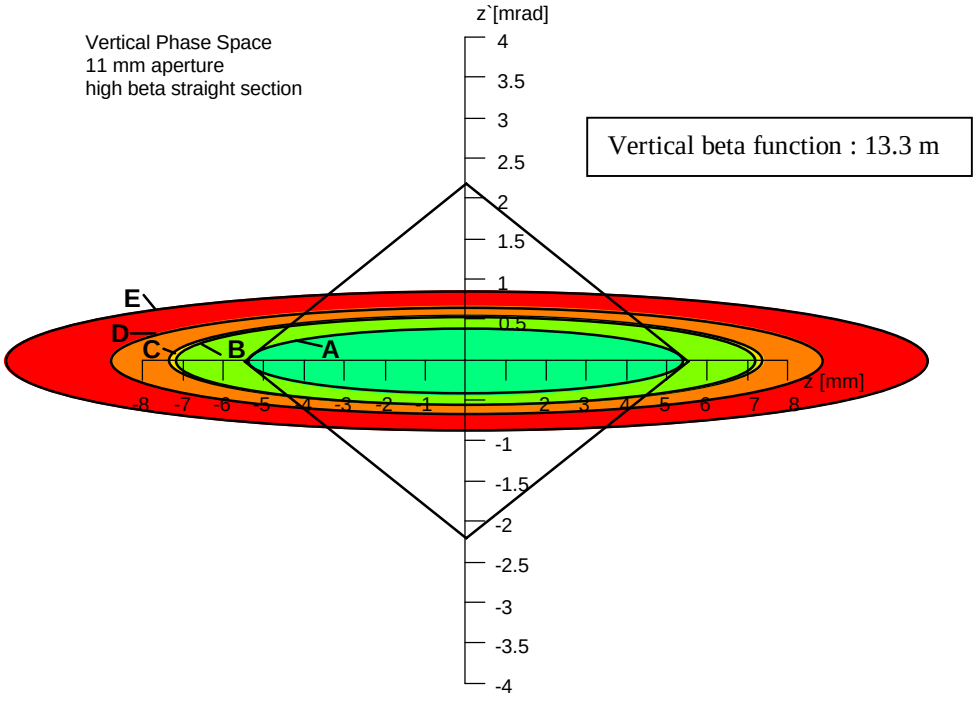

Figure 4-5 Vertical phase space in a high beta straight section in the 4nm optic

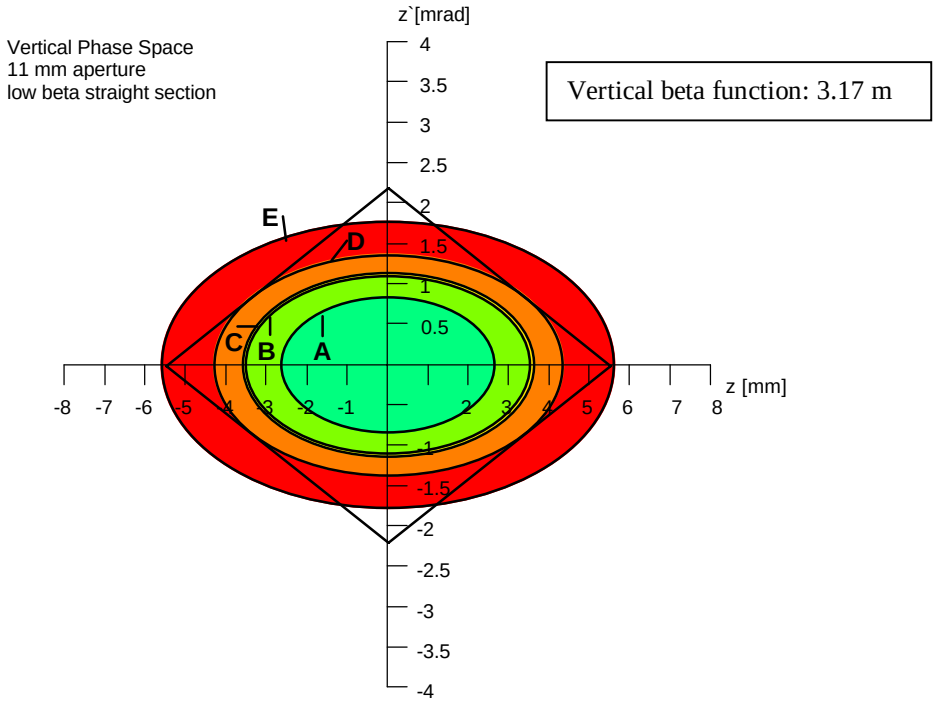

Figure 4-6 Vertical phase space in a low beta straight section in the 4 nm optic

Different acceptance limits are shown in the figure:

- Acceptance A (dark green) is the vertical acceptance defined by the 11 mm vacuum vessels in the high beta straight sections.
- Acceptance B (light green) applies to a 9mm aperture in a low beta straight section.
- Acceptance C (yellow) applies to a 15mm aperture in a high beta straight section
- Acceptance D (orange) applies to an 11mm aperture in a low beta straight section.
- Acceptance E (red) applies to the 32 mm aperture in the dipole vacuum vessels.

The phase space outside the dipole Acceptance E (red) is of small interest since electrons that are scattered into it are rare and most likely stopped before reaching the straight section vessel. The colouring is made to visualise the different acceptances and indicates that with increasing betatron oscillation amplitude the probability for the electrons to be lost is increasing. Looking to the figures it becomes immediately clear that the low beta function is much more adapted to the vacuum chamber dimensions than the high beta functions: Electrons in the acceptance D still pass whereas in the high beta straight section only electrons in the acceptance A can pass. The optimum beta function to match a given vacuum chamber can be calculated using Equation 2-11:

$$\frac{\partial A\left(\beta(0)\right)}{\partial \beta(0)} = \frac{d^2}{\left(\beta^2(0)+D^2\right)}\left(D^2-\beta^2(0)\right)$$

The minimum is therefore reached for

$$\boxed{\beta_{opt}(0) = D}$$

Equation 4-3 Optimum beta function in a straight section

The beta function at the entrance and the exit of the straight section becomes:

$$\boxed{\beta(s=\pm D) = \beta_{opt}(0) + \frac{D^2}{\beta_{opt}(0)} = 2D}$$

Equation 4-4 Minimum beta function at the entrance and exit of a straight section vessel

This gives the following figures for the optimum acceptance and the phase advance:

$$\boxed{A_{opt}\left(\beta(0)=D\right) = \frac{d^2 \cdot D}{D^2+D^2} = \frac{d^2}{2D}}$$

Equation 4-5 Optimum acceptance for a straight section vacuum chamber

$$\Delta\Psi = \beta(0)\int_{-D}^{D}\frac{1}{\beta^2(0)+s^2}ds = \arctan\left(\frac{D}{\beta(0)}\right) - \arctan\left(\frac{-D}{\beta(0)}\right) = \arctan(1) - \arctan(-1) = \pi/2$$

Equation 4-6 Phase advance for optimum beta function in straight section

The ratio of the total acceptance with respect to optimum acceptance can then be calculated to be:

$$\frac{A\left(\beta(0)\right)}{A_{opt}} = 2\frac{\beta(0)/D}{1+\left(\beta(0)/D\right)^2}$$

Equation 4-7 Ratio of total acceptance with respect to the optimum acceptance

The tolerance towards other beta functions can be taken from the following figure:

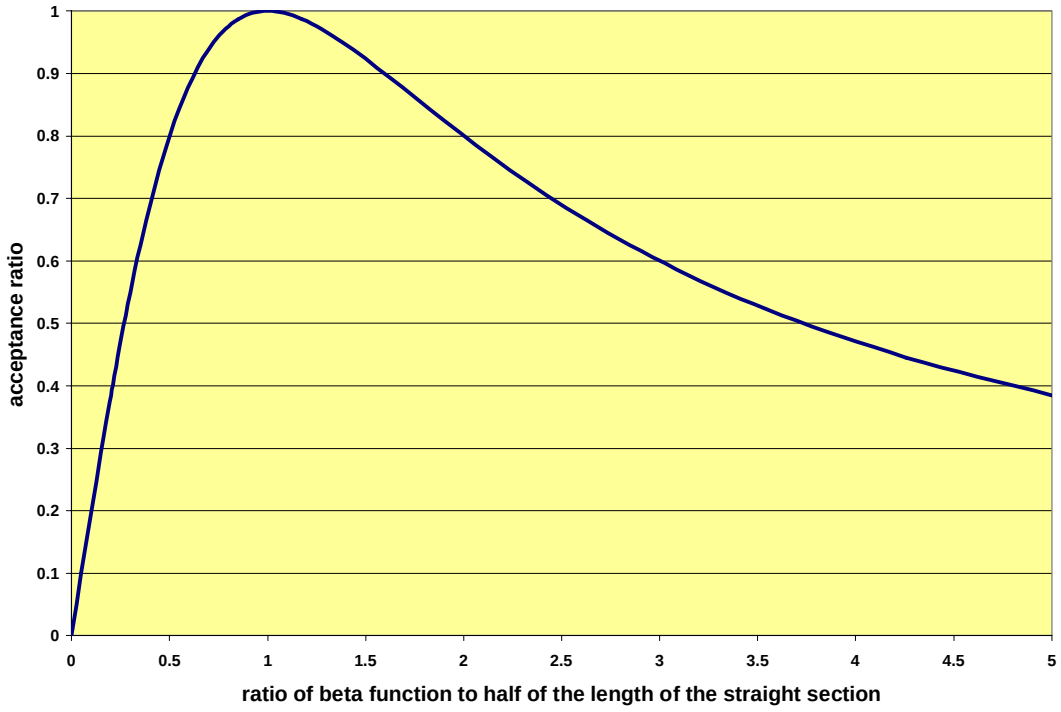

Figure 4-7 Ratio of total acceptance to optimum acceptance as function of the beta function

The variation of the acceptance around the maximum is rather flat. A factor 2 change on the beta function only reduces the acceptance by 20%. A factor 5, however, gives already a reduction of 62%.

It is also useful here to discuss again the Equation 2-12 and Equation 2-13 for the maximum position and angle as function of s.
For the optimum acceptance they become:

$$z_{\max}(s) = d\sqrt{\frac{\beta^2(0)+s^2}{\beta^2(0)+D^2}} = \frac{d}{\sqrt{2}}\sqrt{1+\frac{s^2}{D^2}}$$

Equation 4-8 Maximum electron position for optimised beta function

$$z'_{\max}(s) = \frac{d}{D}\sqrt{\frac{D^2}{\beta^2(0)+D^2}} = \frac{1}{\sqrt{2}}\frac{d}{D}$$

Equation 4-9 Maximum electron angle for optimised beta function

In the middle of the straight section (s=0) the maximum position becomes

$$z_{\max}(s=0) = d\sqrt{\frac{\beta^2(0)}{\beta^2(0)+D^2}} = \frac{d}{\sqrt{2}}$$

Equation 4-10 Maximum acceptable position in the middle of the straight section

4.2.3 Position and angular acceptances

It is useful to have a look to the position and the angular acceptances within a straight section vacuum vessel. They depend on the chamber geometry and the beta function and are related to the total acceptance.

The ellipse A_p that represents the position acceptance touches the frame in the maximum position corner and can be calculated to be:

$$A_p(z=d, z'=0) = \frac{z_{\max}^{\ 2}}{\beta(0)} = \frac{d^2}{\beta(0)}$$

Equation 4-11 acceptance ellipse for electron position

The ellipse A_a that represents the angular acceptance touches the frame at the maximum angle corner and can be calculated to be:

$$A_a(z=0, z'=\frac{d}{D}) = \beta(0)\cdot z'^2_{\max} = \frac{d^2}{D^2}\beta(0)$$

Equation 4-12 acceptance ellipse for electron angle

Both ellipses can be related to the total acceptance via:

$$A_p = A_t\left(1+\frac{D^2}{\beta^2(0)}\right)$$

$$A_a = A_t\left(1+\frac{\beta^2(0)}{D^2}\right)$$

$$\frac{1}{A_t} = \frac{1}{A_p} + \frac{1}{A_a}$$

Equation 4-13 Relations between position acceptance, angle acceptance and total acceptance

After the presentation of the different equations it is useful to reflect on some of outcomes of them.

The optimum beta function is only determined by the length of straight section (Equation 4-3). This means that the optimisation can be done independent of the vacuum chamber aperture. Also the ratio of the total acceptance with respect to the optimum acceptance which is given by Equation 4-7 is independent of the chamber aperture.

The total acceptance depends quadratically on the chamber aperture as can be seen in Equation 2-11. This leads to a variation of the vertical elastic gas scattering in a quadratic manner and therefore rather rapidly limits the minimum gap. The minimum required vertical acceptance is considered to be $A_z \approx 1\cdot10^{-6}$ m rad[61].

The beta function at the entrance and the exit a straight section vacuum vessel can only be lowered to the length of the straight section (Equation 4-4).
The only way to reach larger acceptances for a given ID gap is to provide focusing along the Insertion Device length to reach smaller beta functions (Equation 2-11). Whether this focusing will be provided between several Insertion devices or by means of including quadrupole fields into the Insertion Device has to be studied in detail. For very small beta functions, however, the focusing has to be included in the Insertion Devices.

Setting the beta function in the middle of the straight section to its optimum results in equal angular and position acceptances: $A_a=A_p=d^2/D=2A_t$ (Equation 4-11, Equation 4-12).
Raising the beta function reduces the position acceptance as can be seen from Equation 4-11. Above a three times the optimum beta function the total acceptance can be approximated by the position acceptance with less than 10% error: $A_t \Rightarrow A_p=d^2/\beta(0)$ (Equation 4-13).
Reducing the beta function reduces on the other hand the angle acceptance as can be seen from Equation 4-12. Below one third of the optimum beta function the total acceptance can be approximated by the angle acceptance with less than 10% error:
$A_t \Rightarrow A_a=d^2\,\beta(0)/\,D^2$ (Equation 4-13).

The phase advance along the straight section (Equation 4-6) reaches 90 degrees for the optimum beta function. The exit of the vacuum chamber therefore probes a completely different region of the phase space that the entrance. This gives a large probability to find as many electrons lost at the exit as at the entrance.

4.2.4 The normalised phase space

It is useful to use normalised coordinates to transform the acceptance ellipses into circles in the normalised phase space. For this specific case of a extremum of the beta function (α=0) one can choose

$$w = z \Big/ \sqrt{\beta}$$
$$w' = z' \cdot \sqrt{\beta}$$

Equation 4-14 Normalised coordinates

This transforms the acceptance ellipse in the centre of the straight section:

$$A(z,z') = \frac{z^2}{\beta(0)} + \beta(0)z'^2 \Rightarrow A(w,w') = w^2 + w'^2$$

Equation 4-15 Normalised phase space

The equations for the acceptance presented above remain valid since they do not explicitly contain the position and the angle. The maximum electron positions and angles of the acceptance ellipse, however, have to be transformed in the following manner:

$$w_{\max}(s)=\frac{1}{\sqrt{\beta(s)}}\cdot z_{\max}(s)=\frac{1}{\sqrt{\beta(s)}}\cdot\sqrt{A(\beta(0))\cdot\beta(s)}=\sqrt{A(\beta(0))}$$

$$w'_{\max}(s)=\sqrt{\beta(s)}\cdot z'_{\max}(s)=\sqrt{\beta(s)}\cdot\sqrt{\frac{A(\beta(0))}{\beta(0)}}=\sqrt{\frac{\beta(s)}{\beta(0)}}\sqrt{A(\beta(0))}$$

$$w'_{\max}(0)=\sqrt{A(\beta(0))}$$

Equation 4-16 Maximum normalised coordinates for the acceptance ellipse

The maximum electron position and angle allowing passing by the vacuum chamber (Equation 4-1) transform to:

$$w_{\max}=\frac{z_{\max}}{\sqrt{\beta(0)}}=\frac{d}{\sqrt{\beta(0)}}$$

$$w_{\min}=\frac{z_{\min}}{\sqrt{\beta(0)}}=-\frac{d}{\sqrt{\beta(0)}}$$

$$w'_{\max}=\sqrt{\beta(0)}\cdot z'_{\max}=\sqrt{\beta(0)}\cdot\frac{d}{D}$$

$$w'_{\min}=\sqrt{\beta(0)}\cdot z'_{\min}=-\sqrt{\beta(0)}\cdot\frac{d}{D}$$

Equation 4-17 Extreme normalised positions and angles to pass a straight section vacuum vessel.

The line for the frame coming from the vacuum chamber acceptance therefore become:

$$w'_1(w)=\frac{\beta(0)}{D}\left(w-d\Big/\sqrt{\beta(0)}\right)$$

$$w'_2(w)=\frac{\beta(0)}{D}\left(w+d\Big/\sqrt{\beta(0)}\right)$$

$$w'_3(w)=-\frac{\beta(0)}{D}\left(w-d\Big/\sqrt{\beta(0)}\right)$$

$$w'_4(w)=-\frac{\beta(0)}{D}\left(w+d\Big/\sqrt{\beta(0)}\right)$$

Equation 4-18 Lines limiting the chamber acceptance in the normalised phase space

The normalised phase space is drawn in Figure 4-9 and Figure 4-8 for a low beta and a high beta straight section in the 4 nm optic and for a 5m long 11 mm vertical aperture vacuum vessel. The same scaling for w and w' is applied in both figures.

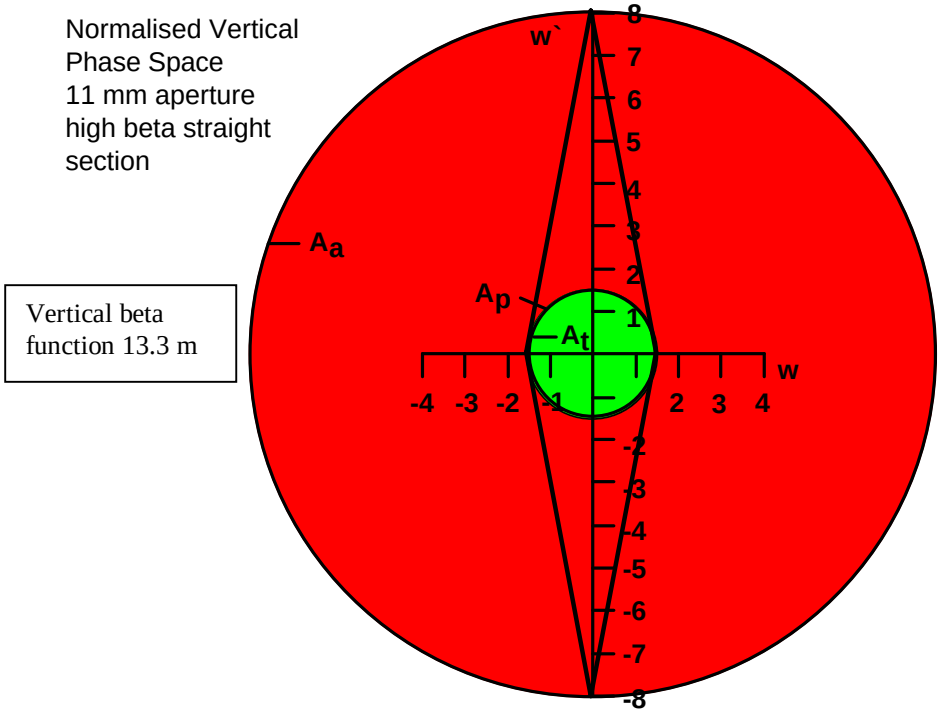

Figure 4-8 Normalised phase space in a high beta straight section

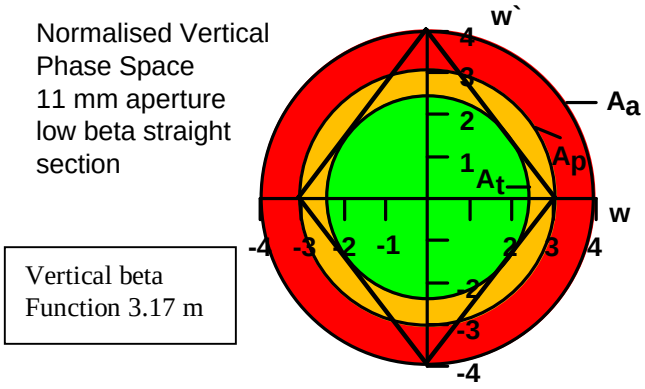

Figure 4-9 Normalised phase space in a low beta straight section

The figures contain the frame given by the vacuum chamber as well as the circles for the total acceptance A_t, the position acceptance A_p and the angle acceptance A_a. The frame given from the vacuum chamber is a rhombus. For a beta function close to the optimum as it is the case for the low beta straight section the frame is close to a square. For the case of a beta function much larger than the optimum as it is the case for the high beta straight section one can see that the position acceptance becomes much smaller than the angle acceptance. It is so close to the total acceptance that the difference between them can not be distinguished in the graph.

4.2.5 Fraction of phase space probing

Looking to Figure 4-9 and Figure 4-8 it is possible to estimate the percentage of electrons intercepted from geometrical considerations. This was done for the case of larger angle acceptances than position acceptances coming from a beta function larger than optimum. The case of smaller beta functions can be treated in the same manner but is of no interest for the ESRF.
Assuming that the electrons with the same probing acceptance A are distributed equally on the circumference of the corresponding circle one can estimate the fraction of electrons intercepted to be equal to the fraction of the circumference which is outside the frame.
There are four cases that have to be discussed:

1. $A \leq A_t$ all electrons pass
2. $A_t \leq A \leq A_p$ a fraction of electrons is intercepted
3. $A_p \leq A \leq A_a$ a fraction of electrons is intercepted

$A_a \leq A$ all electrons are intercepted

Due to the symmetry it is sufficient to concentrate on one quarter of the phase space. One has to calculate the angles where the acceptance circumference crosses the frame given by the vacuum chamber acceptance. This is illustrated in Figure 4-10

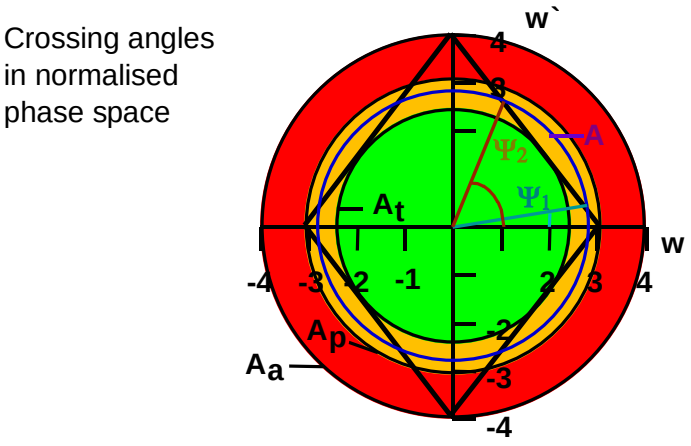

Figure 4-10 crossing angles of acceptance circumference with the vacuum chamber acceptance

For the case 2 there are two crossing points whereas for case 3 there is only one remaining. The fraction f of the electrons which is intercepted can therefore be calculated to be

Case 2: $f = \dfrac{\psi_2 - \psi_1}{\pi/2}$

Case 3: $f = \frac{\psi_2}{\pi/2}$

Equation 4-19 fraction of electrons intercepted by the vacuum chamber

The angles ψ_1 and ψ_2 can be calculated as follows:

$$A = w'^2 + w^2 \text{ and } w' = -\frac{\beta}{D}\left(w - \frac{d}{\sqrt{\beta}}\right) = -\frac{\sqrt{A_a}}{\sqrt{A_p}}\left(w - \sqrt{A_p}\right)$$

=>

$$w_{1,2} = \frac{\sqrt{A_p}}{A_a + A_p}\left(A_a \pm \sqrt{A\left(A_a + A_p\right) - A_a A_p}\right)$$

$$w'_{1,2} = \frac{\sqrt{A_a}}{A_a + A_p}\left(A_p \mp \sqrt{A\left(A_a + A_p\right) - A_a A_p}\right)$$

The corresponding angles are

$$\tan\left(\psi_{1,2}\right) = \frac{w'_{1,2}}{w_{1,2}} = \frac{\sqrt{A_a}}{\sqrt{A_p}} \frac{\left(A_p \mp \sqrt{A\left(A_a + A_p\right) - A_a A_p}\right)}{\left(A_a \pm \sqrt{A\left(A_a + A_p\right) - A_a A_p}\right)}$$

Equation 4-20 angles for crossing the frame

It is useful to look to the cases where A is a the border of the above mentioned cases:

1. $A = A_t = \frac{A_a A_p}{A_a + A_p} = \frac{d^2 \beta(0)}{D^2 + \beta(0)}$

=> $\psi_1 = \psi_2 = \arctan(\frac{\sqrt{A_p}}{\sqrt{A_a}}) = \arctan(\frac{D}{\beta(0)})$

2. $A = A_p = \frac{d^2}{\beta(0)}$

=> $\psi_1 = 0$

and $\psi_2 = \arctan(2\frac{\sqrt{A_a A_p}}{A_a - A_p}) = 2\arctan(\frac{\sqrt{A_p}}{\sqrt{A_a}}) = 2\arctan(\frac{D}{\beta(0)})$

3. $A = A_a = \dfrac{d^2\beta(0)}{D^2}$

=> $\psi_2 = \pi/2$

The fraction f of the electrons which is intercepted is drawn in the Figure 4-11 for the low beta and the high beta case:

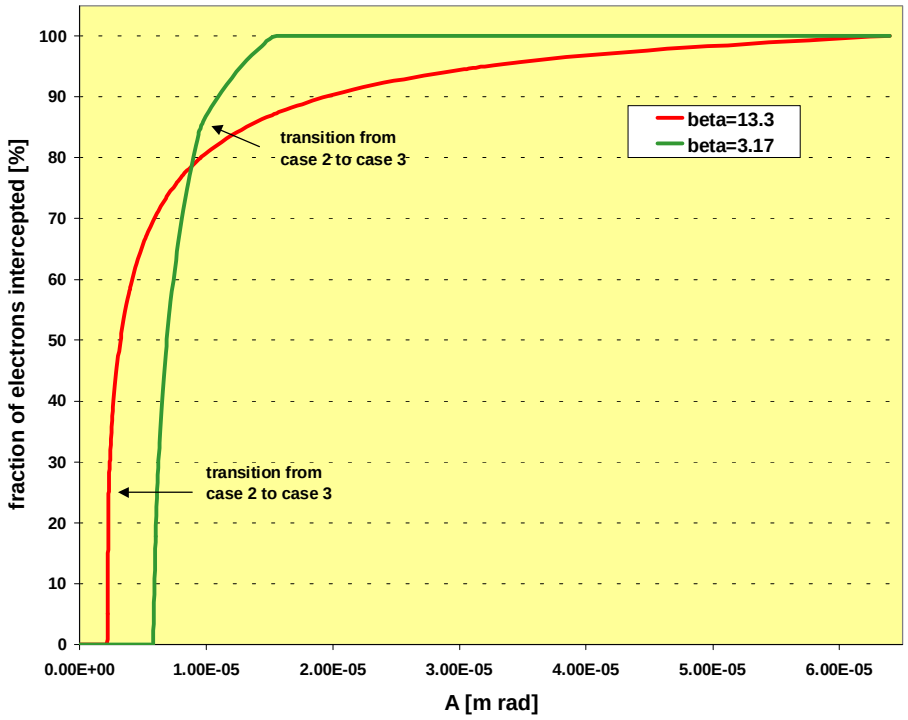

Figure 4-11 Fraction of the electrons intercepted in a low beta straight section as a function of the probing acceptance A

When A reaches the total acceptance there is a steep increase of the fraction of electrons intercepted starting at zero. Since the total acceptance is smaller in the high beta straight sections the losses start earlier.
When A reaches the position acceptance the steepness of the curve goes down. This point is reached early in the high beta straight section since the position acceptance is close to the total acceptance.
When A reaches the angle acceptance all electrons are intercepted. Contrary to the position acceptance the angle acceptance is very large in the high beta straight section.

The acceptance range over which a partial electron interception takes place is from the total acceptance to the angular acceptance for optics with a beta functions as least as large as the optimum beta function. In the case of the optimum beta function the angle acceptance is only twice the total acceptance. In the case of the high beta straight sections the angular acceptance is 29 times the total acceptance as can be calculated from Equation 4-13.

It can be stated that increasing the beta function with respect to the optimum beta extends the zone over which the electrons are only partially intercepted by a vacuum chamber. Consequently the losses will be more distributed between the different vacuum chambers.

Coming back to the discussion of paragraph 4.1 one can now estimate the fraction of electrons which is intercepted in a high beta straight section in the 4nm optic by an 11 mm inner aperture vacuum chamber to about 60% at $A=4\cdot10^{-6}$ m rad. This means a significant increase of losses on ID14, ID16 and ID18 with respect to a 100% interception of the electrons by the ID12 vessel. The losses on ID12 on the other hand are significantly reduced with respect to a full electron interception.

4.3 Loss positions for the different effects

4.3.1 Vertical elastic gas scattering

Electron losses due to vertical gas scattering take place on the vertical aperture limiting points. As an example one can discuss again the situation shown in Figure 2-15 for the vacuum chamber situation in November 1996.
In the 4nm optic the main losses will take place on ID12, ID14, ID16, ID18, ID22, ID26 and ID30. To estimate for each chamber the losses of electrons with oscillation amplitudes exceeding the vertical acceptance one can define two extreme scenarios. The first assumes that the phase space probing of each chamber is rather small so that the losses are randomly distributed between the vessel therefore resulting in an equal distribution. The opposite scenario is the full interception of all electrons which arrive at the vacuum chamber neglecting that due to the phase advance they might pass by. Both scenarios define the range for the fraction of electrons which is intercepted by each chamber. For a homogenous pressure distribution around the ring one can expect the following order:

1. ID12: 14 cells probed

=> 14% (equal distribution) to 44% (full interception) of losses

2. ID22, ID26, ID30: 4 cells probed

=> 13% (full interception) to 14% (equal distribution) of losses

3. ID14, ID16, ID18: 2 cells probed

=> 6% (full interception) to 14% (equal distribution) of losses

Assuming an average interception fraction of 30% between $A=2\cdot10^{-6}$ m rad and $A=4\cdot10^{-6}$ m rad from Figure 4-11 and an equal distribution of the other losses this is modified to:

$$\text{ID12: } 30\% \cdot \frac{14}{32} + 70\% \cdot \frac{1}{7} = 23\%$$

$$\text{ID22, ID26, ID30: } 30\% \cdot \frac{4}{32} + 70\% \cdot \frac{1}{7} = 14\%$$

$$\text{ID14, ID16, ID18: } 30\% \cdot \frac{2}{32} + 70\% \cdot \frac{1}{7} = 12\%$$

For a non-uniform pressure distribution the interception will depend on the phase advance and has to be looked in detail.

Since there is only a small phase advance in the high beta straight sections most of the collisions with the vacuum chamber wall will happen at the vacuum chamber entrance.

The same calculation can be done for the recent situation shown in Figure 2-16. This time losses are concentrated on ID8, ID11, ID13, ID23 and ID31.
From the number of cells probed one gets the estimation of the distribution to be:
ID23:
1. ID23: 10 cells probed
=> 20% (equal distribution) to 31% (full interception) of losses
2. ID8: 9 cells probed
=> 20% (equal distribution) to 28% (full interception) of losses
3. ID31: 8 cells probed
=> 20% (equal distribution) to 25% (full interception) of losses
4. ID11: 3 cells probed
=> 9% (full interception) to 20% (equal distribution) of losses
5. ID13: 2 cells probed
=> 6% (full interception) to 20% (equal distribution) of losses

The fraction of electrons intercepted reaches 97% at $A=6\cdot10^{-6}$ m rad and one can therefore estimate the average interception fraction to 50%. This gives the following estimations:

$$\text{ID23: } 50\% \cdot \frac{10}{32} + 50\% \cdot \frac{1}{5} = 26\%$$

$$\text{ID8: } 50\% \cdot \frac{9}{32} + 50\% \cdot \frac{1}{5} = 24\%$$

$$\text{ID31: } 50\% \cdot \frac{8}{32} + 50\% \cdot \frac{1}{5} = 23\%$$

$$\text{ID11: } 50\% \cdot \frac{3}{32} + 50\% \cdot \frac{1}{5} = 15\%$$

$$\text{ID13: } 50\% \cdot \frac{2}{32} + 50\% \cdot \frac{1}{5} = 13\%$$

In this case the phase advance is large along the straight section so that electron collisions can be expected to be about the same in number at the entrance of the straight sections vessels as at the exit.
In both examples there is about a factor 2 of differences in electron collisions between the different chambers for distributed source points. Apart from the fact that the vertical acceptance should be chosen as large as possible it helps to have many vacuum chambers of the minimum aperture at the same time.

4.3.2 Vertical injection mismatch

The losses due to a wrong steering or wrong focusing in the vertical plane of the injected beam are characterised by the well-defined source point and pure vertical betatron oscillations. It is not possible to predict any clear phase space distribution of the injected electrons since practically all combinations of angle and position are possible. The losses on the different chambers can, however, be estimated by plotting

the different frames for each straight section vessel into the phase space at the injection point. The zones in the phase space where the electrons are lost on a specific chamber depend on the order of straight sections.
The following figure shows the normalised vertical phase at the injection location for the Initial situation with the vacuum chamber situation of November 1996. The outer circle is the dipole acceptance and the inner circle is the acceptance defined by the 11 mm inner aperture vessels in the high beta straight sections. The phase space region probed by the vacuum chambers in cells 6,8,10,12,14,16 and 18 are marked with the corresponding number.

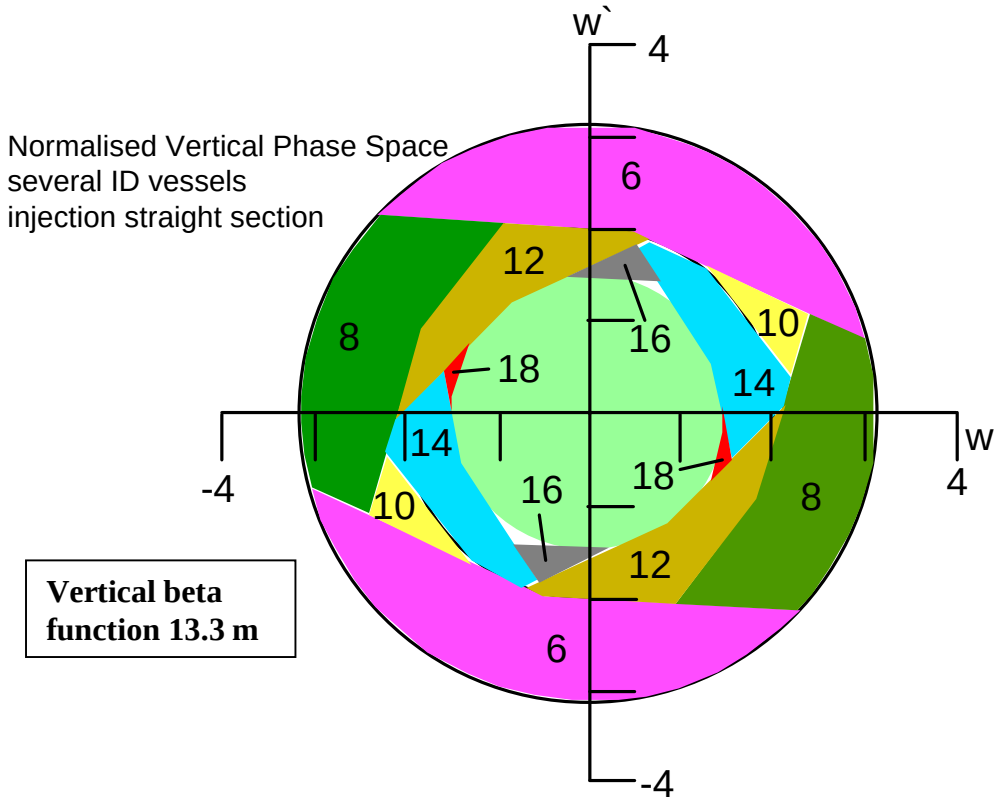

Figure 4-12 Loss positions following vertical injection mismatch in the Initial Situation

Electrons with $4.1 \cdot 10^{-6}$ m rad < A < $9.9 \cdot 10^{-6}$ m rad are practically all intercepted in the straight sections ID6, ID8 and ID10. The corresponding phase space is the outer ring formed by the three cells.
Electrons with $2.2 \cdot 10^{-6}$ m rad < A < $4.1 \cdot 10^{-6}$ m rad are practically all intercepted in the straight sections ID12, ID14, ID16 and ID18. The corresponding phase space is the inner ring formed by these cells. There is only little phase space left in this acceptance range to pass by ID18. Consequently vertical injection losses will only occur between ID4 and ID18.
If the electrons coming from the injection are equally distributed in the phase space the percentage of electrons intercepted by the different chambers is equal to the ratio of the surface in the phase space with respect to the total phase space surface. However, the injected beam has only an emittance of less than$\cdot 10^{-7}$ m rad. Losses in the vertical plane will therefore mainly come from missteering. In this case the losses are

concentrated on one or two points depending on the combination of angle and position at the exit of the septum.

The same graph is drawn in Figure 4-13 for the Recent Situation.

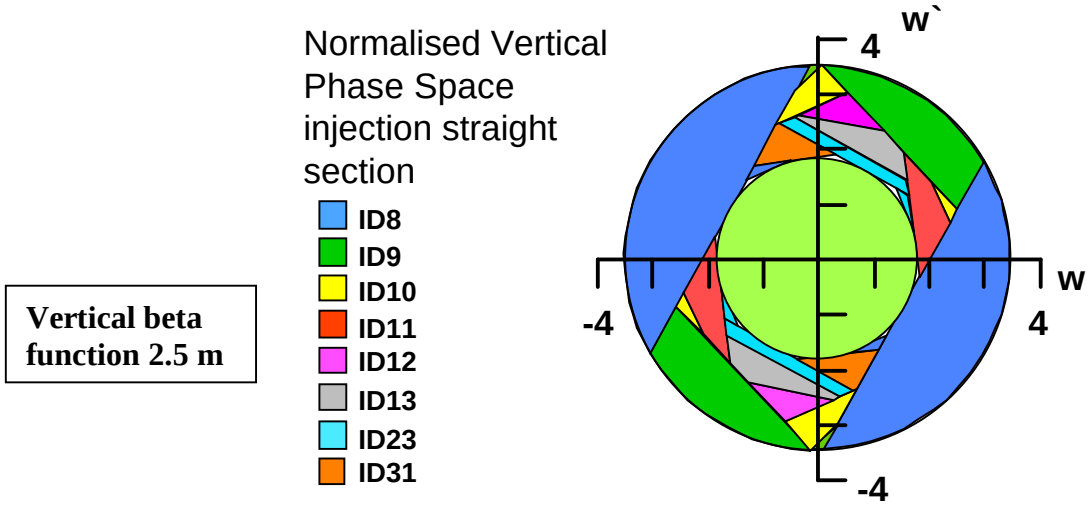

Figure 4-13 Loss positions following vertical injection mismatch in the Recent Situation

The first limiting point is ID8 where there is only a 2 m long 8 mm vertical aperture vessel. ID9, ID10 and ID12 are 5 m long 11 mm inner aperture vessels. The limitation in ID11 is the In-vacuum undulator that is shown at value of 8 mm. ID13 contains a 5 m long 9 mm inner aperture vessel. ID23 and ID31 have 5 m long 8 mm inner vertical aperture vessels installed.

All of these chambers can receive electrons from vertical injection mismatch. The losses on the 11 mm chambers can occur up to ID12. The 8 mm vessels can still intercept electrons in the second turn. In the graph the corresponding parts are drawn for the ID8 and the ID23 vessel.

Looking in detail into the phase advances one finds that the losses on ID12, ID13, ID23 and ID31 only appear at the exit. Electrons that would fall on the ID12, ID13 and ID23 entrance are already intercepted on ID8. The In-Vacuum undulator prevents from losses on the entrance of ID31. This prediction is in line with the fact that the radiation at the exit of the ID23 vacuum chamber is measured to be higher than at the entrance.

4.3.3 Horizontal elastic gas scattering

In the horizontal plane the main aperture limitation is coming from the septum S3. The next limitation is coming from the standard vacuum chamber in the QF7 magnets where the horizontal beta function reaches its maximum. All electrons with $7 \cdot 10^{-6}$ m rad < A < $23 \cdot 10^{-6}$ m rad are intercepted by the septum sheet in the Initial situation. Electrons with larger betatron amplitudes are due to the symmetry well distributed around the ring.

4.3.4 Horizontal injection mismatch

The horizontal injection mismatch can be treated in the same way as in the vertical case. The phase space at the septum point is drawn in the next figure

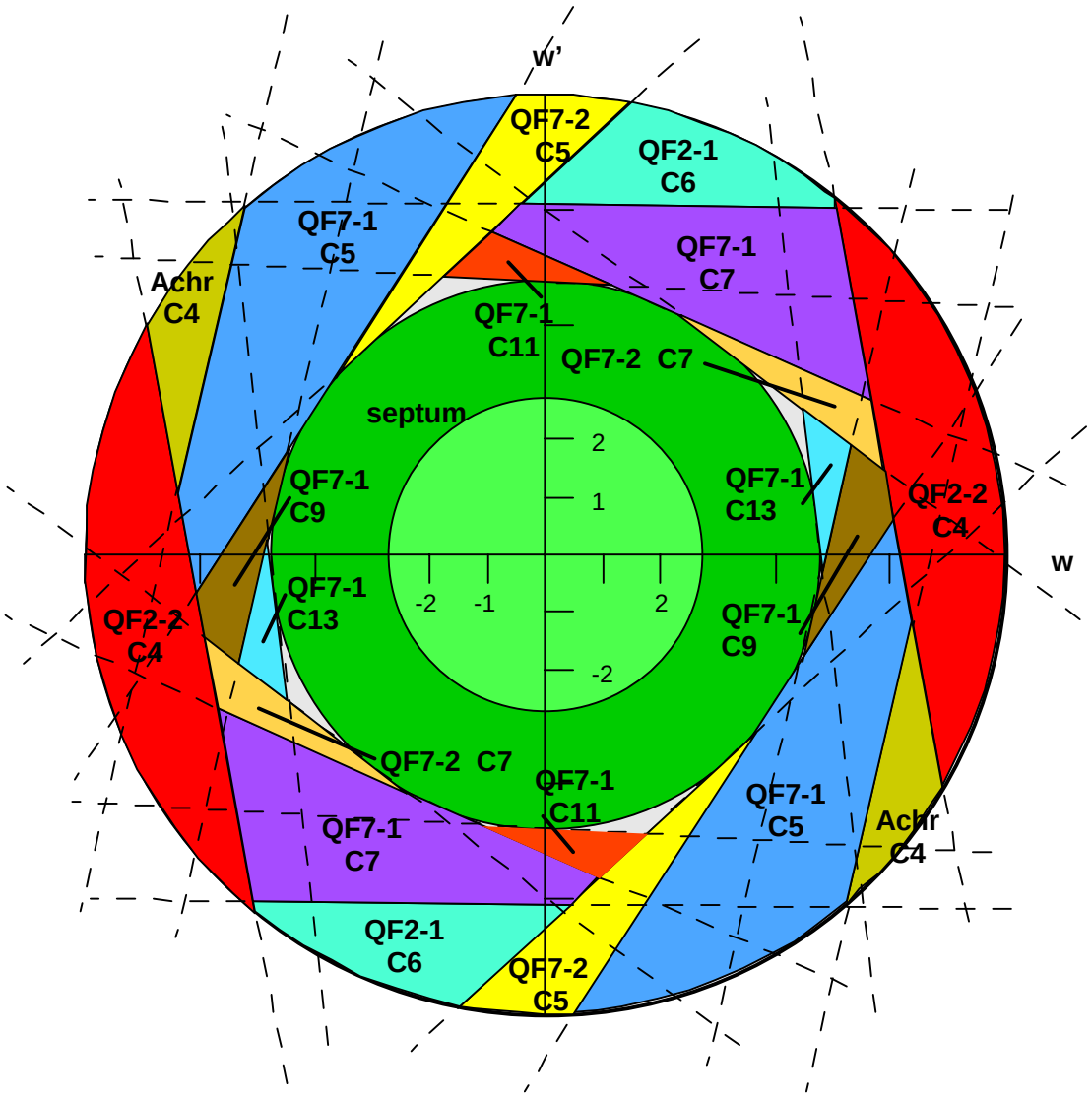

Figure 4-14 Loss positions due to horizontal injection mismatch

The scaling is the same as for the vertical phase space. This represents the fact that the horizontal acceptances are much larger than the vertical ones. It has, however, to be kept in mind that the injection process requires some phase space volume for the injected beam to oscillate around the stored beam.

For A > $23 \cdot 10^{-6}$ m rad the electron collisions points are drawn up to cell 13. Afterwards there is little space left for electrons to pass through.

All electrons with $7 \cdot 10^{-6}$ m rad < A < $23 \cdot 10^{-6}$ m rad are lost on the septum sheet. It depends on the initial position and angle whether this takes place after one turn or several turns. The inner circle is the septum acceptance of the Initial Situation.

4.3.5 Longitudinal capturing during injection

If injected electrons are outside the longitudinal acceptance they will continuously loose energy. The question is whether they are reaching the physical horizontal aperture before they go on a resonance. This largely depends on the remaining betatron oscillation due to the injection process.
If the physical aperture is reached first all electrons will collide with the septum sheet.
If the electrons are reaching a resonance the collision point depends on the kind of the resonance. In the case of a horizontal resonance the electrons will again be lost on the septum again.
In the case of a vertical resonance they will hit a small vertical aperture vessel. With several chambers of the same aperture there will be one which has the smallest acceptance due to chamber misalignment, beta function beat or closed orbit error. The betatron amplitude gain per turn depends on the strength of the resonance. The electrons therefore preferably hit the vessel with the smallest acceptance but might also reach others of about the same acceptance.

4.3.6 Scattering with energy losses

For scattering processes with resulting energy loss of the electrons such as inelastic gas scattering and Touschek scattering there is always a combination of betatron oscillations and energy loss. The same considerations as for electrons outside the longitudinal acceptance are therefore valid.
If the scattering takes place in a high beta straight section it is, however, clear from the discussion of the energy acceptance that the electrons will hit a resonance first.
Depending on the machine tuning there are several special cases:
- The energy loss jumps the electron to a betatron tune outside the RF acceptance but still within the energy acceptance due to the physical aperture and dynamic aperture. This is identical to an electron outside the longitudinal acceptance and was discussed before.
- The energy loss jumps the electron to a betatron tune below the integer resonance but still within the energy acceptance due to the physical aperture and RF voltage. The electron then starts synchrotron oscillations. The energy of the electron will increase until the resonance is reached.
- The energy loss jumps the electron to a betatron tune below the corresponding integer resonance, outside the RF acceptance but still within the energy acceptance due to the physical aperture. The energy will continue to decrease until a resonance or the vacuum chamber is reached.

4.3.7 Summary of loss positions

From the above-developed scenarios it can therefore be expected to have losses on the following vacuum vessels:

1. **The vertical aperture limiting points** due to
- vertical missteering of the injected beam. The amount of losses decreases as the distance from the injection point becomes greater.

- vertical elastic gas scattering. The loss distribution depends on the source point and aperture distribution as well as the optics tuning.
- Resonance losses from inelastic gas scattering, Touschek scattering, GRAAL and injection losses due to longitudinal mismatch. This is especially the case in high intensity per bunch operation with large vertical chromaticity. The distribution depends on the resonance strength as well as the machine imperfections in case of several points of about the same aperture.

2. **The septum sheet** resulting from
- horizontal elastic gas scattering
- horizontal injection mismatch
- energy losses outside the high beta straight sections due to the limitation of the energy acceptance by the horizontal physical aperture
- direct losses on the septum sheet from a mismatch at the end of the transfer line

3. **The cells downstream the injection** due to
- Horizontal injection missteering down to cell 13
- Vertical injection missteering down to cell 7

4. **After the second dipole of cell 7** due to
- Energy losses due to scattering on laser photons beyond the energy acceptance of the physical aperture of the achromat

5. **All other cells** due to
- Inelastic gas scattering and Touschek scattering leading to energy losses beyond the energy acceptance due the physical aperture of the achromats
- Elastic gas scattering leading to betatron oscillations larger than the acceptances of the standard vacuum vessels

5. Radiation creation and detection

An Electron entering into the wall of a straight section vacuum chamber interacts with the chamber material. The interaction changes the electron energy and trajectory and creates radiation. This chapter deals with the consequences on the scraper and the use of the created radiation for beam loss detection.
The basic interactions will be presented in paragraph 5.1. As a special point the heating of the material discussed.
Paragraph 5.2 will focus on the changes provoked on the incoming electron. The for ESRF important case of secondary losses due to incident scattering of electrons on the chamber material will be discussed in this context. This will be done for scattering on a scraper jaw and on an Insertion Device vacuum chamber.
Paragraph 5.3 will introduce the use of the created radiation for beam loss detection. The various beam loss detection systems will be presented and some important examples given.

5.1 Interactions of electrons with the chamber material

A detailed discussion of the relevant scattering effects at the ESRF was performed to become compliant with the new dose limits becoming valid in May 2000[28]. To simulate the scattering process the code GEANT, developed at CERN for detector design purposes, was used. A description of the code can be found in [62]. This code was also used at DELTA to simulate the shower evolution of electron losses on the DELTA vacuum chamber[63].

5.1.1 Longitudinal shower properties

A detailed description of all the relevant parameter of this paragraph is given in[64]. The dominant inelastic scattering process of high energy electrons in matter is bremsstrahlung. The created photons interact again with the chamber material by creating in most of the cases an electron-positron pair. As a consequence a cascade of photons, electrons and positrons is appearing which is called the electromagnetic shower. The shower develops until the particle energy decreases to the point where the radiation cross section is about the cross section for collisions and ionisation losses. The corresponding critical energy ε is 550 MeV/Z with Z as atomic number. From that point on Compton scattering will dominate for the photons and ionisation for electrons.
The most important parameter for the shower evolution is the **radiation length X_0** that can be calculated by:

$$\frac{1}{X_0} = \frac{1}{A} \cdot \left(4\alpha N_A Z (Z+1) r_e^2 \rho \log\left(183 Z^{-1/3} \right) \right)$$

Equation 5-1 Radiation length

with α as fine structure constant, N_A as Avogadro's number, Z as atomic number, A as the atomic weight, r_e as the classical electron radius and ρ as the density of the material. This is a material constant.

Table 5-1 shows some properties of materials used in the ESRF vacuum system:

Property	Iron	Copper	Aluminium	Tantalum
Atomic number Z	26	29	13	73
Atomic weight A	56	64	27	181
Density ρ [g/cm^3]	7.9	9.0	2.8	16.7
Radiation length X_0	17.6 mm	14.3 mm	89 mm	4.1 mm
Specific heat capacity C_p [J/gºC]	0.44	0.38	0.9	0.14
Melting point	1535 ºC	1083 ºC	660 ºC	2996 ºC

Table 5-1 Properties of some materials used in the ESRF vacuum system.

The energy loss per length of the electron coming from the bremsstrahlung can then be expressed by

$$-\frac{dE}{dx} = \frac{E}{X_0}$$

Equation 5-2 Energy loss due to bremsstrahlung

leading to an exponential behaviour of the electron energy:

$$E(x) = E_0 \cdot e^{-x/X_0}$$

Equation 5-3 Average electron energy as a function of material thickness

The material thickness for a given average energy loss of the electron can be calculated by

$$x = -X_0 \cdot \ln\left(1 + \frac{\Delta E}{E}\right)$$

Equation 5-4 material thickness for an average energy loss

Some examples are given in the following table:

ΔE/E	X/X_0	x in iron [mm]	x in copper [mm]	x in aluminium [mm]	x in tantalum [mm]
-0.01	0.01	0.18 mm	0.14 mm	0.89 mm	0.04 mm
-0.02	0.02	0.35 mm	0.28 mm	1.8 mm	0.08 mm
-0.03	0.03	0.53 mm	0.43 mm	2.7 mm	0.12 mm
-0.04	0.04	0.70 mm	0.57 mm	3.6 mm	0.16 mm
-0.10	0.105	1.9 mm	1.5 mm	9.4 mm	0.43 mm
-0.90	2.30	40.5 mm	32.9 mm	205 mm	9.4 mm
-0.99	4.61	81.1 mm	65.9 mm	410 mm	18.9 mm
-0.999	6.91	122 mm	98.8 mm	615 mm	28.3 mm

Table 5-2 material thickness for given average energy loss of the electron

It can be seen that in average a very small fraction of a radiation length is sufficient to throw the incoming electron out of the energy acceptance. In average one tenth of a

radiation length causes an energy loss on the electron which prevents it from passing by the following achromat.

One can also calculate where the shower reaches its maximum:

$$x_{\max} = \left(\log\left(\frac{E}{\varepsilon} \right) - 1 \right) X_0 \cong \left(\log(11 \cdot Z) - 1 \right) X_0$$

Equation 5-5 Depth of maximum electromagnetic shower

For the materials mentioned above this gives the following values

Property	Iron	Copper	Aluminium	Tantalum
Atomic number Z	26	29	13	73
Radiation length X_0	17.6 mm	14.3 mm	89 mm	4.1 mm
x_{max} [X_0]	1.46	1.50	1.16	1.90
x_{max} [mm]	25.7	21.5	103	7.8

Table 5-3 Depth of maximum electromagnetic shower

The depth of maximum electromagnetic shower is important since it indicates the material depth where the maximum of energy will be deposited. The power deposit in the longitudinal direction can be approximated by:

$$\frac{dE}{dx} = k \cdot X_0 \cdot \left(\frac{x}{X_0} \right)^{x_{\max}/2X_0} \cdot e^{-x/2X_0}$$

Equation 5-6 Energy deposit in an electromagnetic shower

with the normalisation factor $k = E \Big/ \left[2^{\left(x_{\max}/2X_0 + 1\right)} \Gamma\left(x_{\max}/2X_0 + 1\right) \right]$

$\Gamma(x)$ is the Gammafunction. For $x<x_{max}$ most of the energy is used for particle production. For $x>x_{max}$ the number of particles is decreasing and therefore also the total energy deposited by them.

For radiation protection reasons it is also useful to know the length over which 95% of the shower is absorbed. This can be calculated as follows:

$$x_{95\%} = x_{\max} + (0.08 \cdot Z + 9.6) X_0$$

Equation 5-7 Depth of 95% shower containment

Again a table can be given for different materials

Property	Iron	Copper	Aluminium	Tantalum
Atomic number Z	26	29	13	73
Radiation length X_0	17.6 mm	14.3 mm	89 mm	4.1 mm
$x_{95\%}$ [X_0]	13.1	13.4	11.8	17.3
$x_{95\%}$ [mm]	231	192	1050	71

Table 5-4 Depth of 95% shower containment

5.1.2 Transverse shower properties

Whereas the bremsstrahlung is the dominant inelastic scattering process for the electrons the multiple scattering is the dominant elastic scattering process. Multiple scattering is multiple Coulomb scattering with small angles. It deviates the initial electron trajectory and broadens up the electromagnetic shower.
The average angle of the initial electron after the material thickness x can be approximated by

$$\theta_{rms}^2 = \frac{x}{2p^4\beta^2 X_0}\left(\left(21\,MeV\right)^2\left(m^2+p^2\right)\left(1+0.038\log\left(x/X_0\right)\right)^2\right)$$

with m as mass, p as momentum and β as velocity of the particle. For up to a 5 radiation lengths the equation can be approximated with less then a 5 % error by

$$\theta_{rms}^2 = \frac{x\left(21\,MeV\right)^2\left(m^2+p^2\right)}{2p^4\beta^2 X_0}$$

Equation 5-8 rms angle due to multiple scattering of the initial photon

For relativistic electrons it further reduces to

$$\theta_{rms}^2 = \frac{1}{2}\cdot\frac{x}{X_0}\cdot\left(\frac{21\,MeV}{p}\right)^2 \quad \text{and finally}$$

$$\theta_{rms} = \sqrt{\frac{1}{2}}\cdot\left(\frac{21\,MeV}{p}\right)\cdot\sqrt{\frac{x}{X_0}}$$

For the ESRF electron energy one can further simplify the equation to:

$$\theta_{rms} \approx 0.0025\cdot\sqrt{\frac{x}{X_0}}$$

Equation 5-9 rms multiple scattering angle for 6 GeV electrons

Some values are given in the following table

Θ_{rms} [mrad]	x [X_0]	x in iron [mm]	x in copper [mm]	x in aluminium [mm]	x in tantalum [mm]
0.25	0.01	0.14	0.17	0.89	0.04
0.5	0.04	0.57	0.69	3.6	0.16
0.75	0.09	1.3	1.6	8.0	0.37
1.0	0.16	2.3	2.8	14	0.66
1.25	0.25	3.6	4.3	22	1.0
1.5	0.36	5.1	6.2	32	1.5
1.75	0.49	7.0	8.5	44	2.0
2.0	0.64	9.2	11	57	2.6
2.25	0.81	12	14	72	3.3
2.5	1.0	14	17	89	4.1

Table 5-5 rms multiple scattering angles for 6 GeV electrons in different materials

The angles can be compared for example to the maximum angle allowed in an 8 mm aperture vacuum chamber: $z'_{max} = d/D = 4mm/2.5m = 1.6$ mrad. In average a fraction of a radiation length is therefore sufficient to deviate the electron trajectory beyond the angle acceptance of the vacuum chambers. The fact that the rms angle depends on the square root of the depth gives rather large angles for very small material thickness. 1% of a radiation length therefore leads to already 0.25 mrad angle. **This results in a high probability for the electrons to escape the material in the case of scattering at grazing angle.** This case will be discussed in paragraph 5.2.

The last quantity to discuss is the transverse dimension of the electromagnetic shower that as was already mentioned is also determined by the multiple scattering. The corresponding material constant is the **Moliere Radius R_M**:

$$R_M = 0.0265 \cdot (Z + 1.2) \cdot X_0$$

Equation 5-10 Moliere Radius

The Moliere Radius is the radius in which 90% of the initial electron energy is deposited. It is listed for the different material in the following table:

Property	Iron	Copper	Aluminium	Tantalum
Atomic number Z	26	29	13	73
Radiation length X_0	17.6 mm	14.3 mm	89 mm	4.1 mm
R_M [X_0]	0.72	0.80	0.38	1.97
R_M	12.7 mm	11.4 mm	33.8 mm	8.1 mm

Table 5-6 The Moliere Radius for different materials

5.1.3 Photo-Nuclear Reactions

Although the bremsstrahlung photons mainly react with the material to create electron-positron pairs a significant part of them undergo photo-nuclear reactions[28].

- At photon energies from a few MeV up to 30 MeV the dominating processes are giant resonances[65]. The photon field forces the protons to one side of the nucleus.
- Between 30 MeV and 140 MeV quasi deuterons are created. The photon is creating a proton-neutron pair in the nucleus.
- Above 140 MeV the photons can liberate pions.

These processes create free neutrons immediately after the reaction. Since the neutrons carry no charge their interaction length in matter is much longer than that of electrons, positrons and photons. Despite their small production rate with respect to the bremsstrahlung they are responsible for a significant part of the dose rate outside the tunnel wall and the tunnel roof.

A significant fraction of the photons also undergo nuclear reactions by exciting the core. This activates the material. For the stainless steel vacuum chambers used at the ESRF more than 10 isotopes of the chemical elements between Kalium and Cobalt are found. The decay time of the elements varies from a few hours in the case of ^{56}Mn to 5.26 years in the case of ^{60}Co. Following a beam loss on a vacuum chamber the activated material will decay. The radiation will first be dominated by the isotopes with small decay times since they usually have a higher specific activity. **Generally one can say that the radiation at a given time t after the activation of the material is dominated by the isotopes with decay times in the range of this time t**. For an

example the radiation during intervention in MDT after beam loss intensive studies will be dominated by isotopes with the decay time of one hour.
The case of continuous beam losses of the material is different. Starting from not activated material the activation will rise for every isotope until equilibrium activation is reached where the creation of the isotopes equals their decay. For a production rate of P and a decay time T one can calculate the number N of isotopes and their variation to be:

$$\frac{dN}{dt} = P - \frac{N}{T} \text{ and } N(t) = PT\left(1 - e^{-t/T}\right)$$

Equation 5-11 number of isotopes for permanent production

The time to reach this equilibrium is in the range of decay time of the isotope. The equilibrium value N=PT is higher for isotopes with long decay times. If the activation is stopped after the time t it will again be the isotopes with a corresponding decay time, which dominate the radiation. **The typical decay time of a vacuum chamber activation is therefore similar to the time during which the chamber was activated**.
Since the activation of the vacuum chambers is a consequence of the beam losses the production rate varies a lot.
Within a week range it is the beam loss difference between the MDT and the USM that creates the variation.
Looking over the range of a few months it is the change between runs and shutdowns, which creates the variation.
The evolution of the machine operation and the vacuum chamber installation prevent the activation to remain stable even when looking to a period of several years.
Some examples will be given in paragraph 5.3.1.

5.1.4 Heating up of a scraper following electron interception

One of the first attempts to investigate the problem of losses on the Insertion Device vessels was to reduce the vertical aperture at a given location and to measure the difference in the loss distribution. The element used for that was the scraper device that is located in ID6 about 1 m upstream from the middle of the straight section. The exact geometry of a scraper jaw is presented in the appendix, The scraper device contains four individually motorised jaws: one upper, one lower, one internal and one external. These devices were originally installed as a diagnostic tool to measure, for example, the transverse quantum lifetime to calculate the emittances. From spring 96 on they were intensively used for beam loss studies since one can stop the electrons with them. The use of the scrapers to intercept electrons avoiding beam losses on the Insertion Device vacuum chambers will be presented in chapter 6. The effect of incident scattering on a scraper jaw will be described later on in this chapter.
From Table 5-4 one can see that the 20 mm thickness of the scraper jaws is not sufficient to completely stop the electromagnetic shower. In the contrary the fact that the scraper is only 1.4 radiation lengths thick leads to the shower maximum close to the exit of the scraper jaw. As a consequence there is a lot of radiation escaping the scraper, which is a problem for the radiation protection. It was therefore decided to build another scraper out of tantalum with approximately 150 mm jaw thickness to overcome this problem. This scraper will be mounted in cell 30 for test purpose at the end of the year.

During vacuum interventions in cell 6 the scraper jaws were found damaged. Very thin grooves were engraved on the material. Investigation in detailed revealed a melting of the copper to be at the origin. Overheating due to synchrotron radiation was excluded since the traces appear on all scraper jaws and the water cooling of the scraper jaws is designed to prevent from this. The only possible explanation is therefore the overheating of the material following a full beam loss. The loss has to be fast to overcome the water cooling. Active beam kills with the scraper and beam losses following RF trips or interlocks are the only processes that are fast enough in this respect. Following the damage it is useful to estimate the temperature rise of the copper. Iron and aluminium are also interesting to discuss since the beam losses take place on the vacuum chambers when the scraper jaws are fully removed from the beam. Tantalum is the last material that is studied since it will be used for the new scraper.

From the equations presented in paragraph 5.1.1 one can estimate the temperature increase of the material following electron losses in a very short time period. The total temperature increase can be calculated by

$$\Delta T[^\circ C] = \frac{Q_t[J]}{C_p[J/kg^\circ C]\cdot \rho[kg/m^3]\cdot V_t[m^3]}$$

Equation 5-12 Temperature increase due to particle loss

for the total energy deposit Q_t in the volume V_t of material with the density ρ and the specific heat capacity C_p.

One estimation can be made supposing that 90% x 95%=86% of the total power will be deposit in the cylindric volume $V_t = \pi \cdot R_M^2 \cdot x_{95\%}$

The energy stored in the beam can be calculated by

$$Q_t[J] = I[A]\cdot E[eV]\cdot T_0[s]$$

Equation 5-13 Total beam energy

with T_0 as the revolution period. For the ESRF one gets $Q_t \approx 3.4\text{kJ}$.

A calculation for the temperature rise was done for the different elements and is listed in the following table:

Property	Iron	Copper	Aluminium	Tantalum
86 % of Q_t [kJ]	2.9	2.9	2.9	2.9
Specific heat capacity C_p [J/g°C]	0.44	0.38	0.9	0.14
Density ρ [g/cm^3]	7.9	9.0	2.8	16.7
C_p ρ [J/ g cm^3]	3.5	3.4	2.5	2.3
R_M [mm]	12.7	11.4	33.8	8.1
$x_{95\%}$ [mm]	231	192	1050	71
V_t [cm^3]	117	78	3769	14.7
86 % of Q_t [J]/ V_t [cm^3]	25	37	0.8	197
ΔT [°C]	7	11	0.3	84

Equation 5-14 Temperature increase due to electron losses for different materials

The temperature increase in Tantalum is much higher than in copper or iron due to the smaller volume where the power is deposited since the heat capacity per volume is roughly the same for all the materials. Simulations of the energy deposit of 6 GeV

electrons in a Tantalum target reveal that the above made estimation of the temperature rise is very optimistic. Close to the shower maximum local energy densities of a 200 kJ per cm^3 can be reached in the inner cylinder of 0.1 mm radius[66]. To get a realistic estimation one has to take the beam dimensions into account. Vertically the beam size is smaller than 0.1 mm. Horizontally the beam size that contains 99% of the electrons or σ_x is about 2 mm. This gives a reduction factor of about 20 leading to 10 kJ per cm^3 energy deposit. Using Equation 5-14 gives a temperature rise in tantalum of 3550 ºC thus melting the tantalum.

To avoid melting the material for full beam losses in a short time one has several solutions:

1. Limiting the energy acceptance by vertical resonances. The losses take then place in the vertical plane where one takes advantage of the larger effective transverse dimensions for the energy deposit.
2. Restricting the material thickness to a fraction of the radiation length in order to leave the material before the electromagnetic shower has build up to its maximum. 0.2 radiation lengths would for example lead in average to 18 % energy loss and 1.1 mrad trajectory deviation. This is sufficient to prevent the electrons from escaping into the following cells. The maximum energy deposit in copper for example can be calculated by Equation 5-6 to be at 0.2 radiation lengths only 42% of the energy deposit at x_{max}.
3. Using a low Z material as aluminium or titanium. The disadvantage is that to stop the electrons a large material depth has to be used.
4. Avoiding energy deposition at the scraper surface. If the melting does not appear at the scraper surface there will be no surface destruction. The melting in the bulk material will, however, create fatigue of the material. One can avoid full beam losses on the scraper surface by firing a kicker magnet at every interlock that kicks the beam deep into the scraper material. The action has, however, to take place at latest a fraction of a ms after the RF is switched off. This is rather difficult in case of a failure on the RF system.

5.2 Changes of electron energy and trajectory

5.2.1 Scattering on a scraper jaw

For the beam loss studies the main interest is to know whether the electrons which hit the scraper are really stopped by it. To validate this a particle tracking was done for a head on collision on the upper scraper jaw[67]. The conditions were that the electrons hit the scraper jaw 1 mm above the edge of the 20 mm long copper end of the jaw. The interactions with the material would result in more than 10 % energy loss for more than 99 % of the electrons. In other words less than 1 % of the electrons would succeed in arriving in the following cells. The scraper can indeed be considered as a beam stopper. From the former chapter it is, however, clear that with a material thickness of only 1.4 radiation length the electromagnetic shower will be close to its maximum at the end of the scraper thus leading to a lot of radiation escaping the scraper.

Things are significantly different when the electrons arrive in a grazing incident configuration. In this case there is a high probability that they leave the copper block due to a small angle scattering before losing a lot of energy. This situation was also simulated for the upper jaw[68].

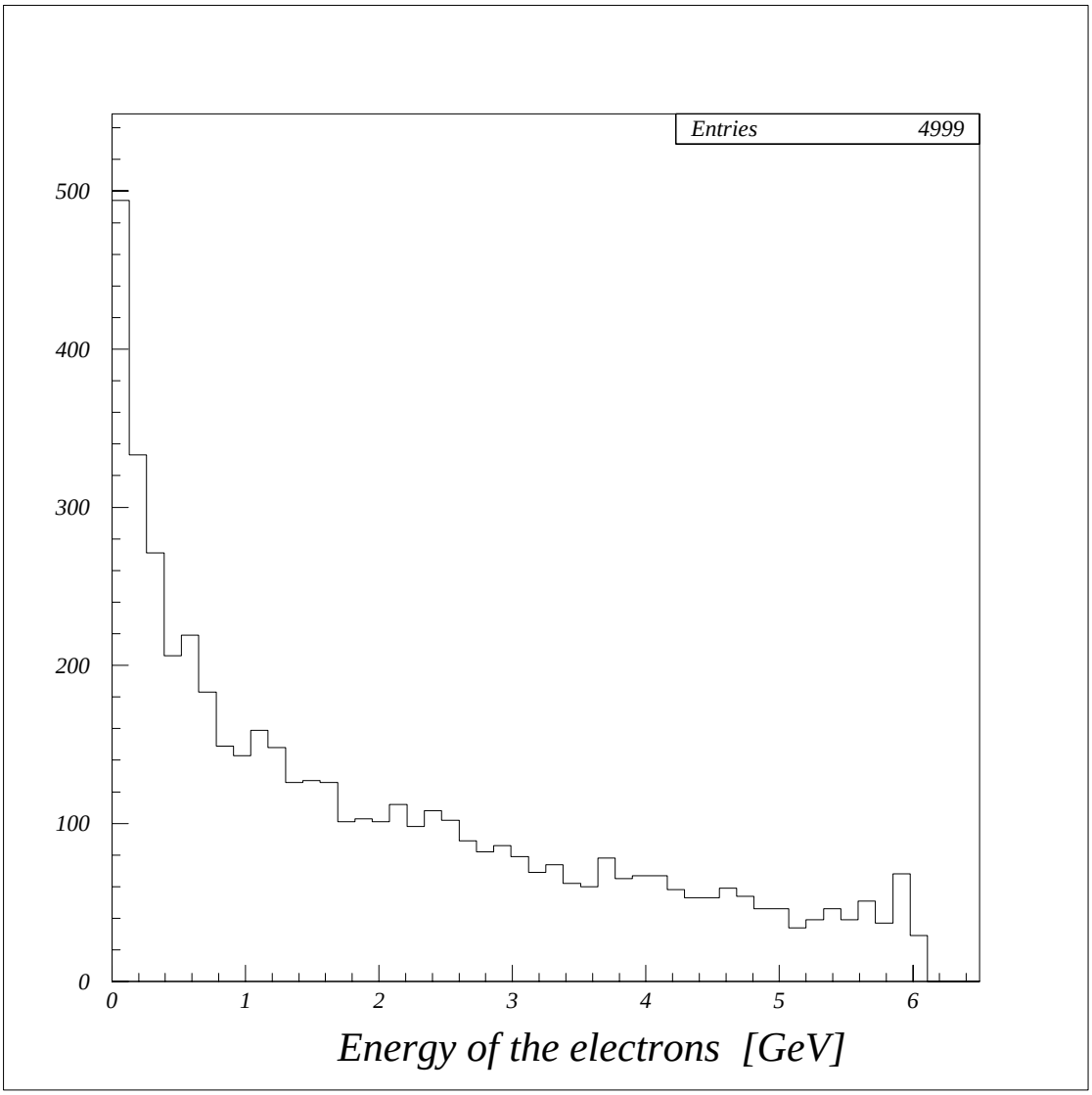

Figure 5-1 Energy distribution of electrons following a grazing incident scattering on a scraper jaw.

The simulation was done for zero angle and position of the electrons with respect to the scraper jaw. About 5 % of the electrons would still have less than the 10% energy loss and therefore a potential to pass by the achromat and be lost in other straight sections. On top of that they will get significant angles from the scattering processes. Figure 5-2 shows that practically all particles will remain within a 20 mrad angular deviation. In the vertical plane positive angles are significantly suppressed by the presence of the scraper jaw itself whereas the distribution of negative angles reveals to be the same as in the horizontal direction.

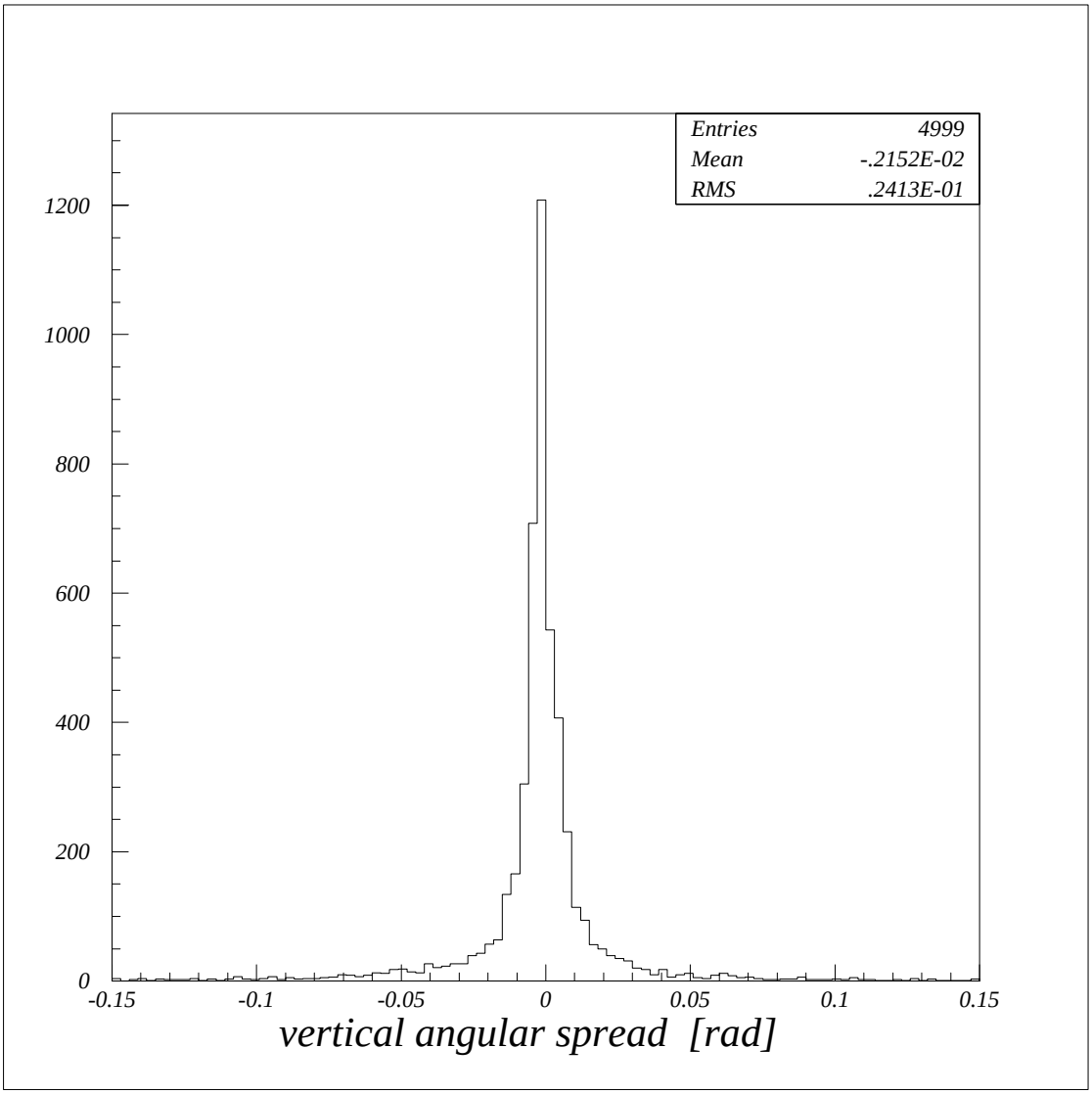

Figure 5-2 angular distribution of the electrons following a grazing incident scattering on a scraper jaw.

The question is which of both scenarios (incident or head-on collision) better describes the reality. To validate this we can use the above-developed beam loss scenarios.
Incident scattering on a vertical aperture limiting scraper jaw will appear in the case where the amplitude of the betatron is slowly increasing from turn to turn. This mainly concerns losses on the vertical integer resonance. The other possibility is when the lifetime is deliberately reduced with the scraper, i.e. moving the scraper jaw towards the beam axis. In all other cases the number of electrons undergoing incident scattering should be rather small.
Since resonance losses are very likely for stable stored beam losses this effect has to be considered when using the scrapers for radiation protection purpose.

5.2.2 Scattering effects on an Insertion Device vessel

With the knowledge of the insertion device chamber geometry and the beta functions it is possible to simulate the scattering of electrons on an insertion device vessel. It is

important to know where along the chamber the electrons are lost and with which vertical position and vertical angle they penetrate the chamber wall.
Although the beta function and the chamber are symmetric with respect to the middle of the straight section the electron losses are not since the electron beam direction tends to create more losses on the chamber entrance then on the exit.

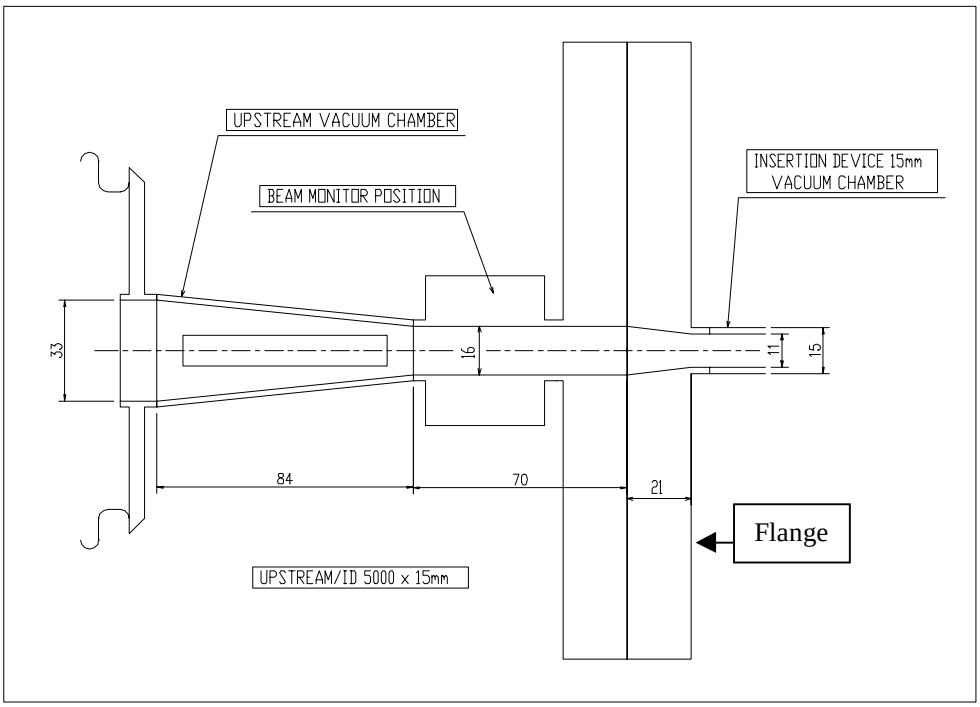

Figure 5-3 Vertical aperture reduction at the entrance of an 11 mm Insertion Device vacuum chamber

The reduction of the vertical aperture upstream of the vessels is done in two steps over a total length of 17.5 cm. The first reduction is from 33 mm down to 16 mm over a length of 8.4 cm and is common to all insertion device vessels. The second step down to 11 mm is then done within the 21 mm thickness of the flange of the 5 m long vessel over the total length of 2.1 cm.

It is helpful to look to the vertical phase space at the entrance of a 11 mm aperture vessel in a high beta straight section in the 4 nm optic.

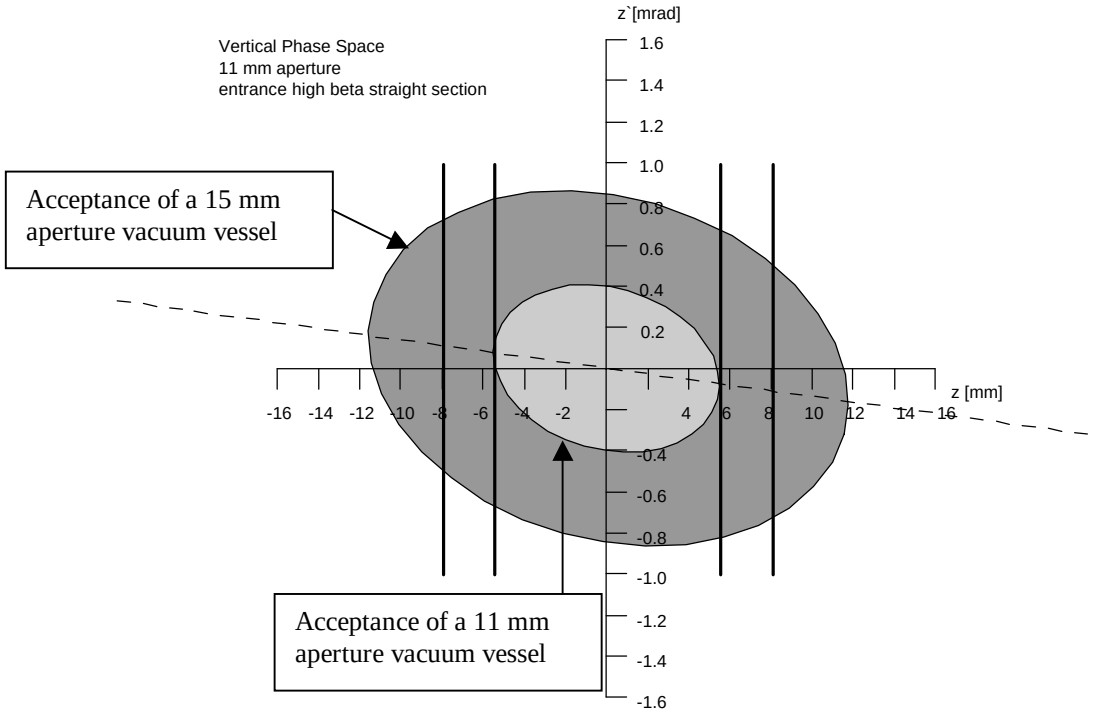

Figure 5-4 Phase space at the entrance of an 11 mm inner vertical aperture vacuum chamber

The acceptances drawn are the total acceptances of the 11 mm and 15 mm inner vertical aperture vacuum vessels in the high beta straight sections.

The vertical lines represent the vertical position range where the electrons hit the chamber flange. The dashed line indicates the positions where, for a given betatron oscillation amplitude, the position is maximum. It can be calculated to be

$\frac{z'}{z} = \frac{-\alpha\sqrt{\frac{\varepsilon}{\beta}}}{\sqrt{\varepsilon\beta}} = -\frac{\alpha}{\beta}$ which becomes $\frac{z'}{z} = -\frac{s/\beta\ (0)}{\beta(0) + s^2/\beta(0)} = \frac{s}{\beta(0)^2 + s^2}$ at the position s in a straight section with minimum beta function $\beta(0)$ in the middle.
At the entrance of the straight section vessel s=-D this gives:

$$\frac{z'}{z} = -\frac{D}{\beta(0)^2 + D^2}$$

Equation 5-15 Most likely angle for electrons at the Insertion Device vacuum chamber entrance.

For the most likely collision point (z = 5.5 mm) the most likely angle is z'= -0.08 mrad in a high beta straight sections and –1.1 mrad for the optimum beta function of 2.5 m. For larger betatron amplitudes or larger positions there are also different collision angles possible. However, on average the dashed line is still followed. The maximum and minimum angles z'_m for a given z and A can be calculated from the electron emittance equation $A = \gamma z^2 + 2\alpha z z' + \beta z'^2$ to be

$$z'_m = -\frac{\alpha}{\beta} \pm \sqrt{\frac{A}{\beta} - \frac{z^2}{\beta^2}} = \frac{1}{\beta^2(0)+s^2}\left(sz \pm \sqrt{A\beta(0)\left(\beta^2(0)+s^2\right) - \beta^2(0)z^2}\right)$$

Equation 5-16 Extreme angles for a given acceptance

One can for example calculate the range of angles electrons at d_{11}= 5.5 mm can have when they just pass by the 15 mm inner aperture vessels (A=A_t(d_{15}=7.5 mm)).
At the chamber entrance s=-D the result is

$$z'_m = \frac{1}{\beta^2(0)+D^2}\left(-Dd_{11} \pm \beta(0)\sqrt{d_{15}^2 - {d_{11}}^2}\right)$$

Equation 5-17 Extreme angles at the at an 11 mm vacuum vessel.

For D=2.5 m one gets the following numbers for the different beta functions:

Beta function β(0)	Minimum angle	Average angle	Maximum angle
2.5	-2.1 mrad	-1.1 mrad	-0.1 mrad
2.7	-2.0 mrad	-1.0 mrad	0 mrad
3.1	-1.9 mrad	-0.9 mrad	0.1 mrad
13.3	-0.45 mrad	-0.08 mrad	0.29 mrad

Table 5-7 Average and extreme electron angles at the vacuum chamber entrance

The material thickness the electrons have to traverse depends on the position and the angle at the chamber entrance. For electrons with negative angle at positive position the thickness is larger for large z and small angles. The length can be calculated from $z' \cong \tan(z') = \frac{\Delta z}{L} = \frac{d_{11}-z}{L}$ to be:

$$L(z,z') = \frac{z-d_{11}}{-z'}$$

Equation 5-18 effective material thickness for an electron hitting a vacuum chamber

There is one limit to set for Equation 5-18.
First of all the vacuum chamber wall is only 2 mm thick. From $|z-d_{11}| \leq 2$ mm one gets:

$$L(z,z') \leq \frac{2\ mm}{-z'}$$

For angles of up to 2.1 mrad, however, this still gives an effective length of more than 0.95m or the equivalent of fifty radiation lengths.

Another limit comes from the multiple scattering. One can estimate that the average electron angle will grow with the multiple scattering angle thus enabling the electron to escape the chamber wall. One can set:

$$L \leq \frac{2\ mm}{\Theta_{rms}}$$

This can be transformed for steel to

$$L \leq \sqrt[3]{0.64m^2 \cdot X_0} = 0.22m$$

Equation 5-19 maximum effective material thickness following multiple scattering.

This is close to $x_{95\%}$=0.23m - another value which can be used to estimate the upper limit of the effective thickness. One can therefore use as total upper limit L=0.22 m.
The effective length as a function of angle and position of the incoming electron is shown in the following graph. The electron position is varied from 5.5 to 6 mm whereas the electron angle is varied from –2.3 mrad to 0.1 mrad.

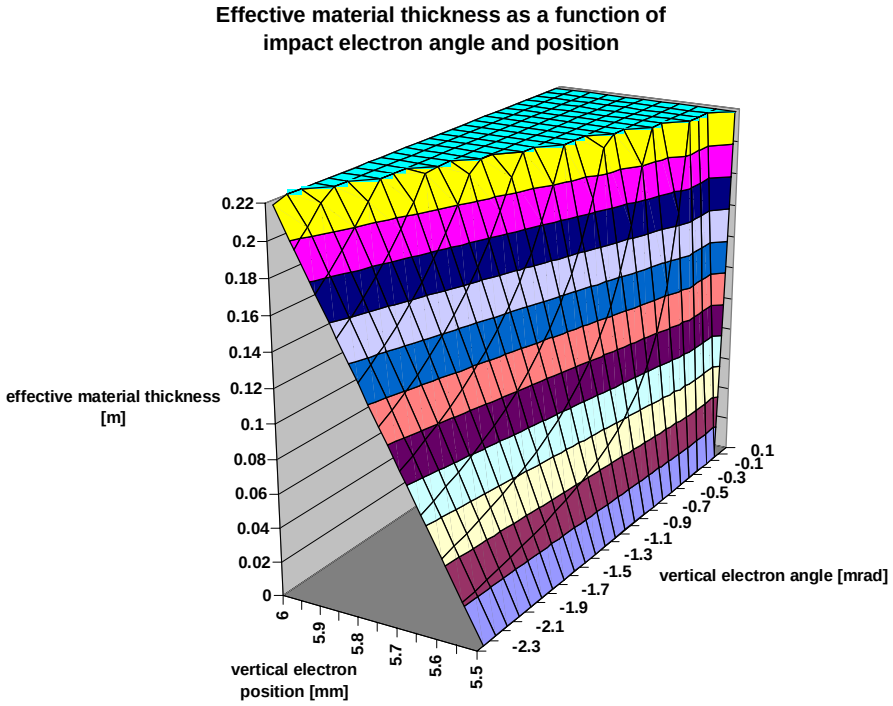

Figure 5-5 Effective material thickness for scattering on an ID vacuum chamber

Electrons with impact positions larger than 6 mm have always sufficient path length to fully develop the electromagnetic shower. Electrons close to the chamber edge on the other hand experience only a very small effective thickness as long as the angle is negative. One can also draw the effective material thickness for the most likely combination of angle and position taking the average angle from Table 5-7:

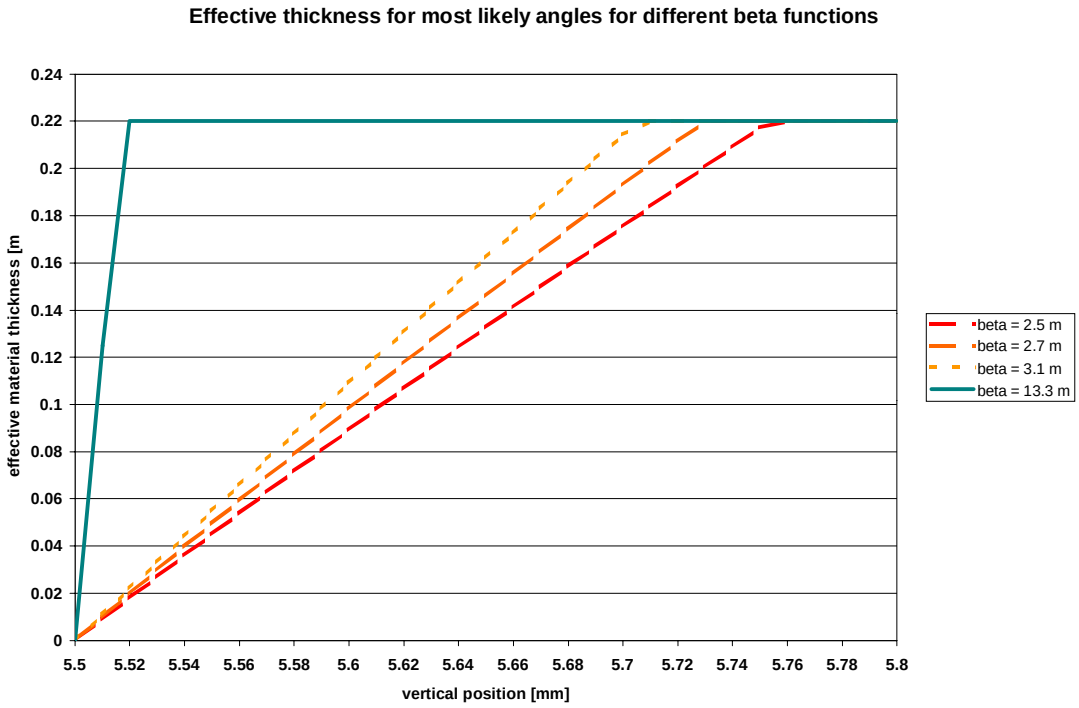

Figure 5-6 effective material thickness for most likely angles

A large beta function in the middle of a straight section results in small electron angles at the vacuum chamber entrance. Consequently the effective material thickness grows rapidly with increasing distance from the edge of the chamber wall. One can therefore expect fewer electrons escaping the vacuum chamber wall without significant energy loss than for small beta functions. Given the average electron angle of about 1 mrad for small beta functions one gets about one radiation length material thickness for only 18 micrometer distance from the chamber wall edge. Even for small beta functions one can therefore say that electrons would hardly traverse a vacuum chamber wall without any effect.

Even for small beta functions one can say that from 250 µm impact depth on, the electrons develop the full shower properties. For values smaller than this one has to expect secondary losses due to electrons escaping the chamber wall without significant energy loss.

5.3 Radiation Detection

This paragraph is dedicated to the different kinds of radiation detection, which are used at the ESRF. Some characteristic examples are given and discussed.

5.3.1 Vacuum chamber activation measurements

Measuring the vacuum chamber activation of many vacuum chambers is only possible during a shutdown. This measurement is therefore an offline measurement and can not be used as a diagnostic for beam loss studies during MDT or USM. Given its integrative character its is, however, an ideal diagnostic to judge the effect of radiation protection measures such as scraper closure or optic changes.

The measurements were performed with a dosemeter that is used by the operators to control the radiation level in the tunnel during interventions. They were always done at the end of the shutdown to minimise the influence of short decay time isotopes. Since the chamber geometry is the same for all 11 mm aperture vessels the results can be directly compared between the different cells.
As an example the activation measurements over a 4 year period of the ID12, ID18 and ID22 vacuum chambers are given in Figure 5-7.

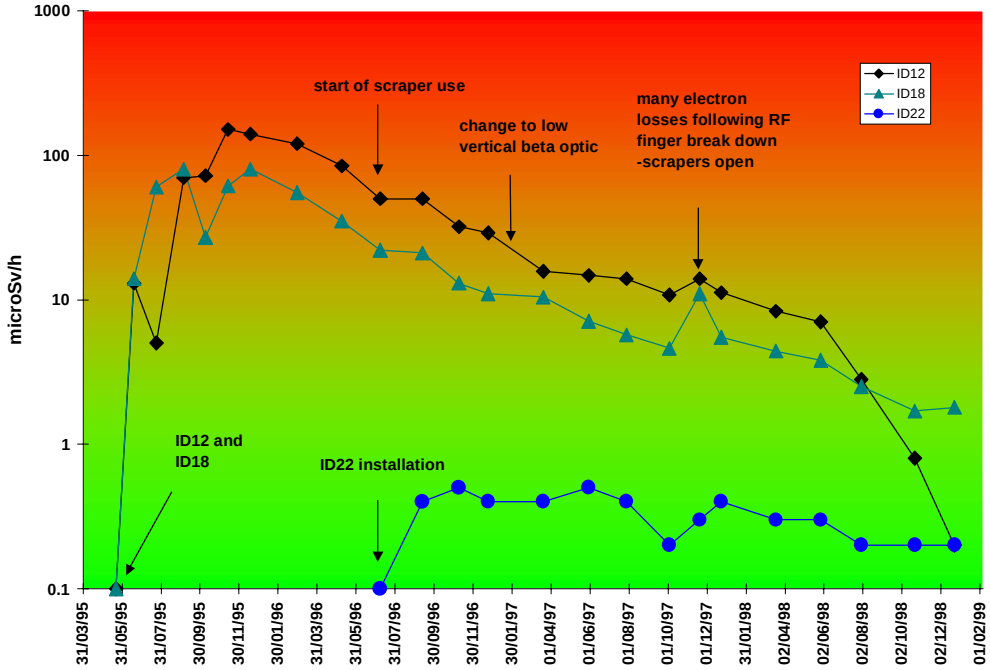

Figure 5-7 Activation of the ID12, ID18 and ID22 vacuum chambers

All three vessels have 11 mm inner aperture. The ID12 and ID18 chambers were installed at the same time and the ID22 vessel one year later. During that time the 4nm optic was still used. As one can see that the ID12 and ID18 activation increased over several runs. The activation of the ID12 chamber was about two times higher than the one of ID18. This can be explained by the fact that ID12 is closer to the injection and that it probes a larger fraction of the storage ring. Then the value decreased due to the installation of more 11 mm vacuum vessels around the ring. **The activation was found to be very concentrated on the first 10 cm of the vacuum chambers. The activation found is therefore in line with the remark made before that the small phase advance in the high beta straight section will only lead to activation at the chamber entrance.** From June 96 on the scrapers were systematically closed during USM to intercept the electrons. **As a consequence practically no losses took place anymore on the 11 mm vacuum chambers. This can be best seen by looking to ID22 activation level that remains constant at a very low level.** The ID12 and ID18 activation levels are still decreasing. The rapid decay of ID12 during the last measurement remains, however, unexplained.
In November 97 a RF finger break down place. Due to overheating and an installation error one of the upper RF fingers in a bellow bend towards the beam axis and killed the beam. It was tried during several shifts to find ways to store beam before the decision was taken to stop the run. During these shifts the injection was running permanently

and the scrapers were kept open. As consequence a lot of activation was created on the vacuum chambers up to ID21. The effect can be clearly seen in Figure 5-7. **This also proved the assumption that the transverse injection losses are completely stopped within one turn.**

The activation of the 8 mm inner aperture vessels is quite different**. The vacuum chambers are activated all along their length with a maximum at the entrance and the exit**. The difference is that these chambers were only installed after the switch to the low vertical beat optic. This gives a large vertical phase advance along the straight section. **The measurements are therefore in line with the theoretical predictions.**

5.3.2 Beam Loss Detectors

A beam loss detection system was put into operation in early 1996 in order to have an on-line diagnostic facility for beam losses at a reasonable cost. It consisted of

- 32 slow beam loss detectors aimed to measure lifetime losses precisely.
- 96 fast beam loss detectors aimed to measure injection losses and full beam losses.

The following were common to both systems

- shielding with 3 mm thick lead to suppress the synchrotron radiation background
- the use of a scintillator as sensitive detector material
- the installation of the detector around the chamber at the entrance of each insertion device vacuum vessel.
- the remote readout and the registration in a historical database

The fast beam loss detectors were also installed downstream of each of the 64 dipoles around the vacuum vessels. The scintillator material is an optical fibre that is read out via a photo diode.
The slow beam loss detectors used Perspex as scintillator material with a photo multiplier at the end to obtain sufficiently large signals.

The beam loss detectors proved to work well on several occasions, however, they revealed severe problems with the long term reliability as well as with the comparisons between different locations.
The following problems were identified:

1. The installation at the entrance of the Insertion Device vacuum vessels resulted in significant changes and even damage after each vacuum intervention in the corresponding zone.
2. Being very close to the beam loss source point made the signal sensitive to a small local displacement of the detector material.
3. The vacuum chamber set-up differs so much from cell to cell that no comparison can be made with the detectors located at the entrance of the vessels.
4. The shielding against synchrotron radiation revealed to be insufficient as synchrotron radiation dose rate is about six orders of magnitude higher in the tunnel than radiation produced from the electron losses.

As a result of these problems an upgraded version of the slow beam loss detectors was developed and installed[69], the characteristics of which are:

- 1cm thick lead synchrotron radiation-proof shielding
- the fixation of the detectors on the inner tunnel wall at the end of each straight section
- an increased scintillator volume
- a bigger and more sensitive photo multiplier

This system proved to work reliably. It is not sensitive to synchrotron radiation and has sufficient sensitivity to measure moderate beam losses in stable stored beam conditions.

A comparison of the initial system set up with the present system set up is shown the following figure:

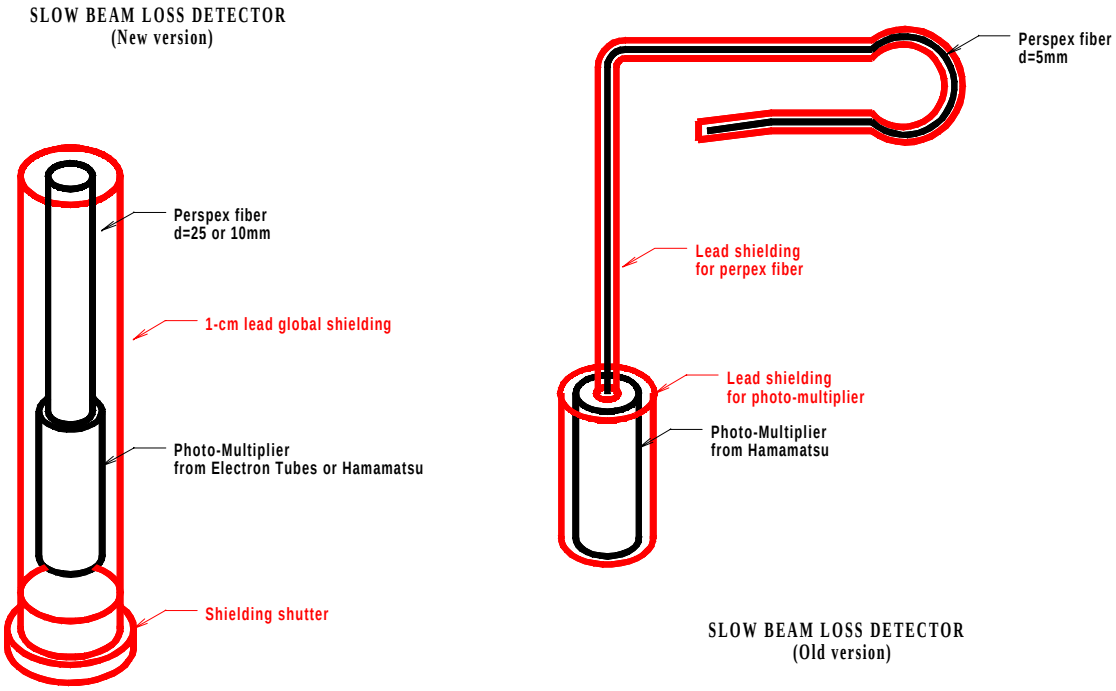

Figure 5-8 Comparison of beam loss detector set up

The beam loss detection system is used at many occasions. Some major uses are

- steering of the injected beam through the septa by minimising the losses. This can be done with less than 0.01 mA booster intensity.
- Minimisation of In-vacuum undulator position offset
- Detection of leak development
- Verification of scraper effectiveness
- Correlating the beam loss locations to the beam loss origin

For example the leak in the achromat of cell 4 which was shown in Figure 3-3 was found during the verification of the beam loss detector readings. The correlation with the pressure can be seen in Figure 5-9.

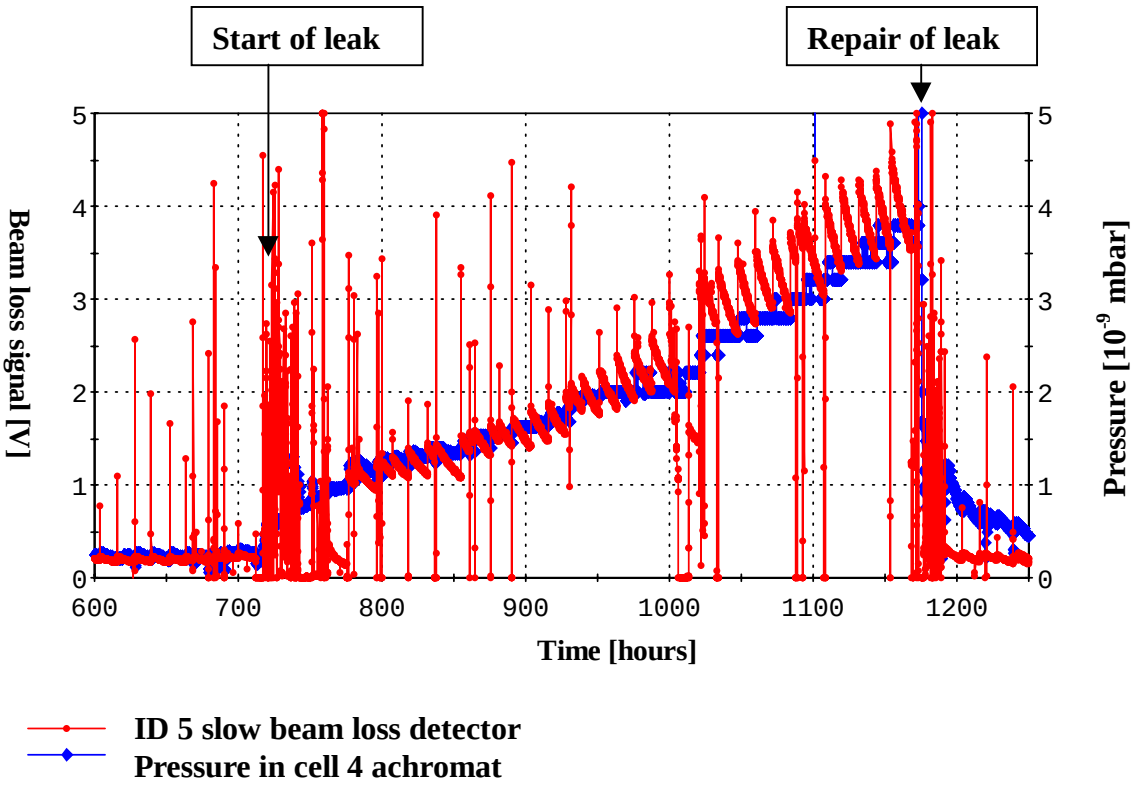

Figure 5-9 detection of a leak in the cell 4 achromat with the ID5 beam loss detector

There is perfect correlation of the beam loss detection signal in the ID5 straight section and the vacuum pressure in the cell 4 achromat during the development of the leak. The saw teeth behaviour of the beam loss detector signal results from the beam intensity variation.

The vacuum conditioning which was presented in Figure 3-2 can also be followed up with the beam loss detectors**.** The correlation of the ID18 detector reading with the average pressure reading is shown in the following graph:

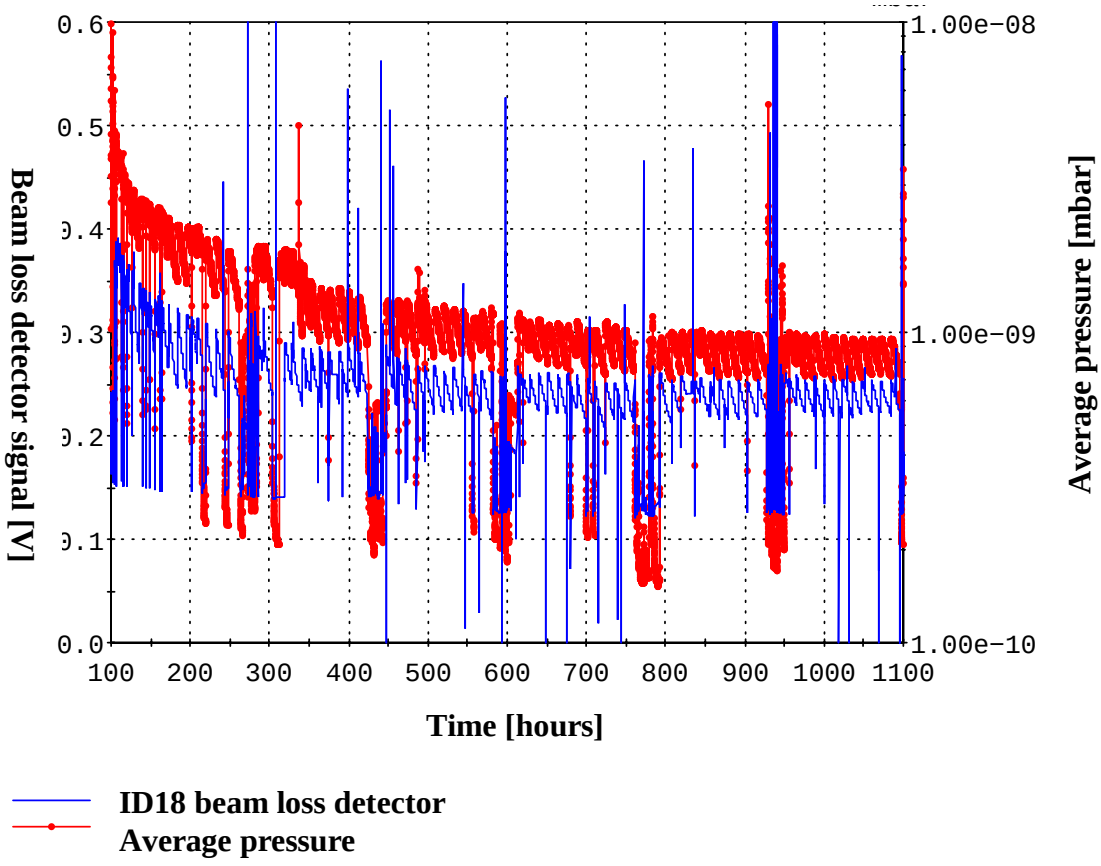

Figure 5-10 Beam losses during vacuum conditioning

During the shutdown the cell 17 was vented to exchange a vacuum chamber.

In both examples the beam loss detector showing the maximum response was the one located in the next straight section. The same behaviour was seen for many of such events. This proves that following a gas scattering event a large fraction of the electrons is hitting the vacuum chamber only a small distance downstream. This is due to the energy acceptance limitation by the physical aperture, following inelastic gas scattering.

The fact that energy losses lead to significant losses just downstream, can also be proven for the GRAAL losses. The correlation of the losses in the ID8 straight section with the GRAAL operation is shown in Figure 5-11:

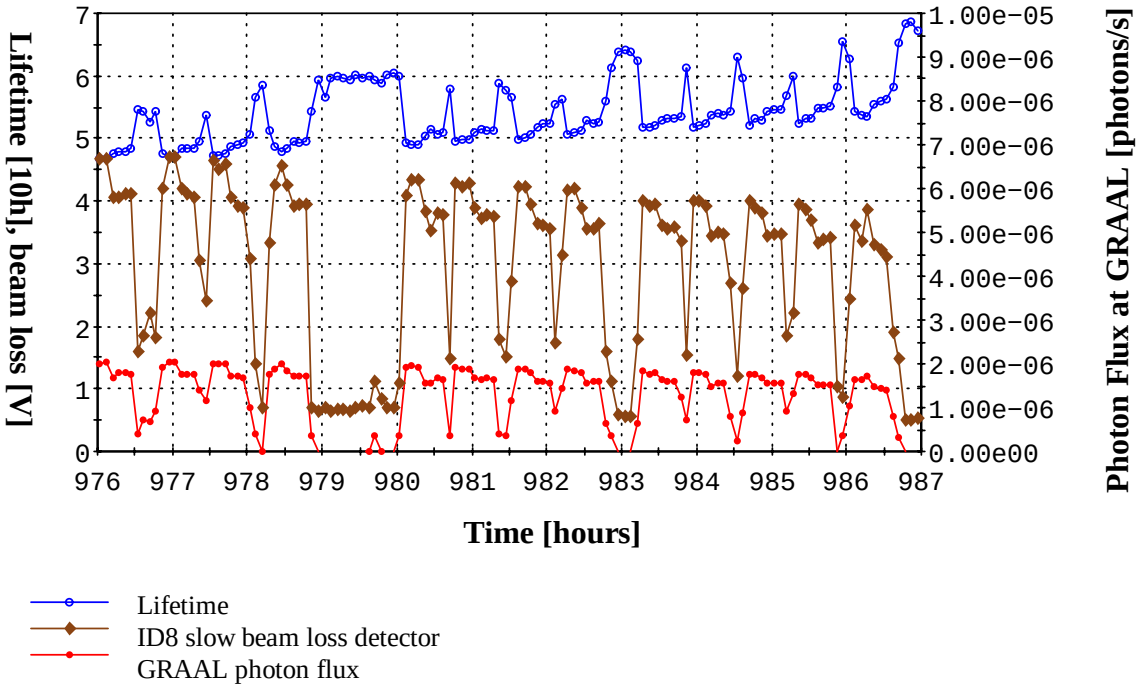

Figure 5-11 Detection of GRAAL losses with the ID8 beam loss detector

The lifetime, the ID8 beam loss detector readout and the photon flux measured on the GRAAL experiment are shown for the duration of 11 hours between two refills. The upper curve is the lifetime, the middle on the beam loss detector reading and the lower one the photon flux at the GRAAL experiment. To validate the impact on the lifetime the experiment is requested to stop the laser for a short time every hour. At the beginning of the decay GRAAL is reducing the lifetime from about 55 hours to about 46 hours, i.e. by 16%. At the end the reduction is from about 70 hours to 55 hours, i.e. 21 %. The experiment is therefore within its 20% lifetime reduction specification. The corresponding GRAAL lifetime over the decay from the two values above is 264 hours ± 7 hours.

One can see that each time the laser is operating the signal of the ID8 beam loss detector increases by roughly a factor 8. This is not the case for all the other beam loss detectors. **One can therefore conclude that the major part of the photon scattered electrons is lost in the cell 7**.

5.3.3 Ionisation chambers

Another method to measure beam losses precisely consists in using ionisation chambers. These are known to work reliably and to have a high dynamic range. The disadvantage is the price of the system. For this reason they were not considered from the beginning. The new European Directive[27], however, made an upgrade of the ESRF radiation protection system necessary since the personal dosimeters can not detect so small dose rates. For this reason a set of 32 ionisation chambers was bought[70]. The problem is that the permitted doses will only be slightly higher than the natural radiation background. It was decided to install the ionisation chambers in the tunnel and to apply a scaling factor to determine the radiation level outside the tunnel.

The used ionisation chamber will have 10 l Argon pressurised at 5 bar as the detector volume and are connected to UNIDOS electrometers. One unit per cell is installed at the outer part of the storage ring on the floor, below the first dipole magnet of the achromat. This is due to the missing space in the free way at the inner side of the ring. A user-friendly control similar to the beam loss detector readout is being developed. The ionisation chambers have the big advantage with respect to the beam loss detectors of measuring absolute values that can easily be compared between different cells. Additionally they have a larger dynamic range and can be used for stable stored beam losses as well as full beam losses without major modifications. They, however, revealed to be less sensitive detectors to some kind of losses than the beam loss detectors. This can be explained by the fact that energy losses due to the limitation of the horizontal physical aperture result in electrons hitting the inner part of the vacuum chamber. This creates bremsstrahlung that is also directed to the inner part of the storage ring. The positioning therefore leads to a small detection efficiency of the ionisation chambers in that respect.

With the ionisation chambers it is also possible to correlate the beam loss locations with the beam loss origin. For example one can clearly identify the beam loss locations following Touschek scattering by simply changing the coupling. This is shown in Figure 5-12.

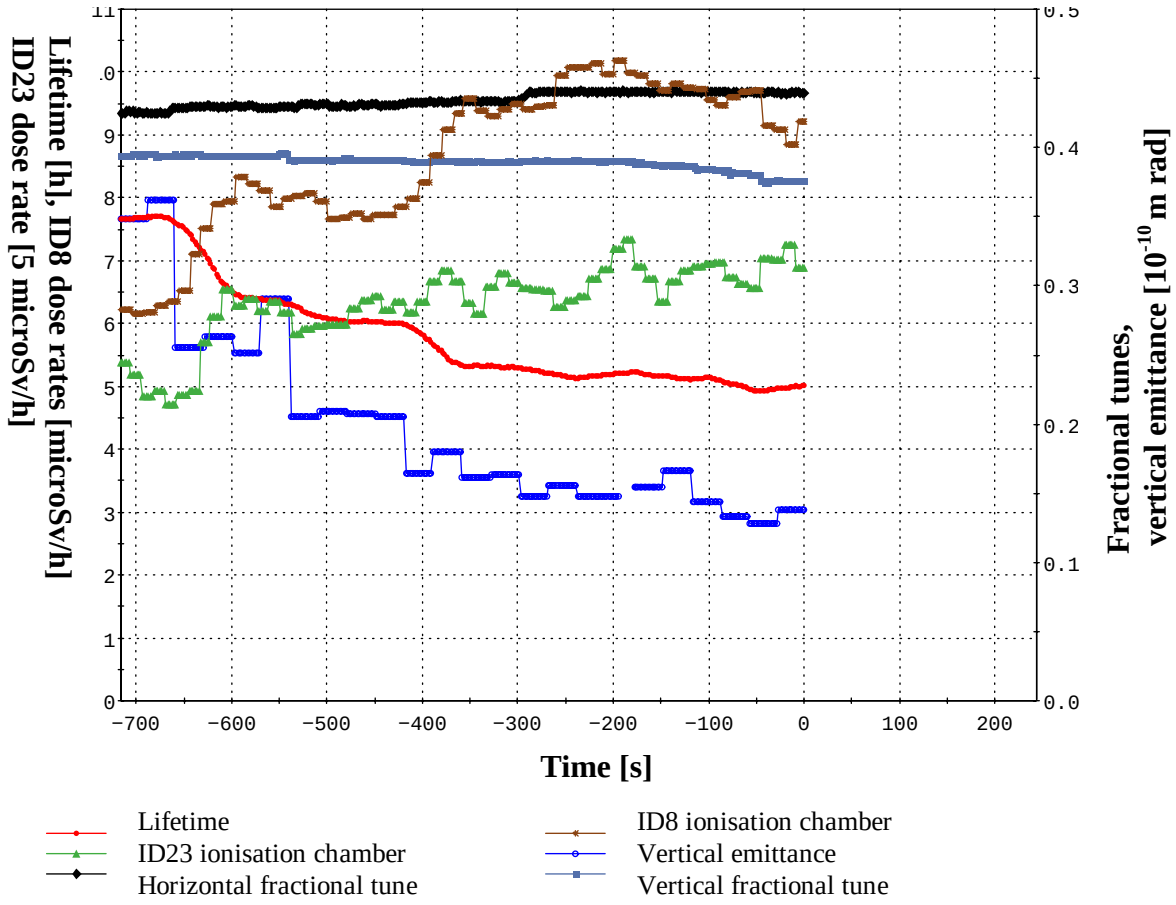

Figure 5-12 Touschek losses identification by variation of the coupling.

The measurement was done with a 16 bunch filling at 30 mA. The coupling was reduced in steps by separation of the horizontal and the vertical tune. The vertical emittance was measured to decrease from about 35 pm to 14 pm. As the consequence the lifetime decreases from 7.6 hours to 5 hours due to the increase of the Touschek scattering. One can see the dose rate measured by the ionisation chambers of ID8 and ID23 increasing. Since Touschek scattering only creates horizontal oscillations and the losses on ID8 and ID23 are vertical losses this is a prove of the coupling from horizontal betatron motion into the vertical plane. In the discussion of the beam loss positions this was explained to come from the energy acceptance limitation due to the vertical integer resonance.

5.3.4 Neutron detectors

To assure the dose rate limitations neutron detectors will be used at the ESRF[28]. There are two neutron detectors per cell installed on the tunnel roof. The detectors are superheated drop detectors with a sensitivity of seven bubbles per μSv[71]. There is no problem with the natural radiation background.

As soon as 2 μSv per fixed four-hour period will be detected by one neutron detector the LINAC will be interlocked until the next four-hour period starts.

The neutron detectors can not be used as online diagnostic due to the poor resolution of 0.14 μSv per bubble. As integrating diagnostic they are, however, very useful to validate changes of the overall losses, the loss distribution and the radiation protection. They are the key measurement for radiation during MDT where no Front Ends are open.

5.3.5 Measurements on beam lines

For some specific measurements it was possible to perform radiation measurements directly on beam lines. One straight section was dedicated to radiation measurements by the safety group over the last two years – ID27 in the beginning and then ID31. This allowed a direct measurement of the bremsstrahlung in the first hutch. Any new vacuum chamber was therefore first installed on ID31. The radiation was then measured during the run to follow up the vacuum conditioning. Once conditioned the chamber was then installed on the straight section of an operating beam line.

The safety group could also do some measurements before a new beam line went into operation. With this measurement the effect of scraper closure could be demonstrated in the 4 nm optic on the 11 mm vertical aperture chamber installed in ID14[72]. When closing the scrapers the radiation level was decreasing by a factor 3 to 4. On the same time the centre of the radiation was shifted by about 5mm. The measurements can be explained when supposing four times more bremsstrahlung coming from the electron losses on the chamber than from the inelastic gas scattering along the full straight section. The offset can be explained by the fact that the electrons are hitting the vacuum chamber about 5.5mm apart from the beam axis.

The safety group also carries out radiation measurements on the outside of the optics hutches. This is especially true for new hutches being constructed and after the installation of a new vacuum chamber. These measurements are the key measurements in USM when the Front Ends are open. The disadvantage of these measurements for beam loss studies is that they are sensitive to the gas bremsstrahlung, strongly dependent on the shielding of the optics hutch and the material inside the optics hutch.

6. Beam loss reduction and scraper use

The most efficient way to limit the consequences of beam losses is to reduce the amount of losses. Even if this is quite clear in principle it is not evident to achieve on a machine in operation. Some performance optimisation of the machine as for example an increase of the brilliance via a coupling reduction might even increase the losses due to, in this case, a reduction of the Touschek lifetime. The first paragraph of this chapter will deal with the different ways to reduce the total amount of beam losses. Not all improvements are noted here since it goes without saying that for operation reasons all efforts are made to keep the failure rate as low as possible and the injection efficiency as high as possible.

Radiation problems develop with the small gap vacuum vessels due to the limited vertical aperture resulting in collecting electrons with large vertical betatron amplitudes. One widely used approach in this case is to limit the aperture at other locations in order to collect the electrons there. This was done at the ESRF by using scrapers. The second part of the chapter therefore deals with all the different aspects of scraper use.
First of all the general strategy is discussed. In a second step general solutions are developed for the different kinds of beam losses including protection against secondary losses. This is followed by some considerations about radiation aspects and the optimum choice of location. Afterwards a complete protection scenario is presented and specified for the ESRF. Finally some measurements are shown which demonstrate the scraper effectiveness to intercept the lost electrons.

6.1 Actions taken to reduce the total amount of beam losses

Some major actions that reduced the total amount of losses were already presented before. This was especially the case for

- The monitoring and limitation of the amount of electrons available for a given time period (paragraph 2.9.3)
- The switch to the low vertical beta optic (paragraph 2.1)
- The increase of the longitudinal acceptance with the installation of a third transmitter unit (paragraph 2.7.1)
- The displacement of the septum sheet further away from the beam axis (paragraph 2.5). This increased the energy acceptance due to horizontal physical aperture limitations.
- The change of the standard filling pattern from 1/3-filling to 2/3-filling to increase the Touschek lifetime (paragraph 2.6.1)
- The change of the hybrid mode refill procedure to avoid beam kill at each injection (paragraph 2.6.1)
- The optimisation of the RF voltage for the different filling patterns (paragraph 2.7.1). Lowering the RF voltage to 8 MV instead of 12 MV allows reducing the chromaticities. This results in an increased energy acceptance due to dynamic aperture. It also increase the bunch length, which is beneficial to the Touschek lifetime.

There are some other changes that are worth to mention:

- To limit unnecessary acceleration of electrons a software "switch off" of the LINAC was implemented to act as soon as the storage ring injection is switched off. This greatly reduces the losses during MDT with very frequent injections.
- Several possibilities of killing the beam where tried until finally using the RF as the acting element was adopted. This proves to give the best loss distribution. A special application was made operational which performs a slow reduction of the RF voltage. Due to the reduction of the longitudinal acceptance the lifetime is decreasing until finally the beam is killed. This application verifies that all Front Ends are closed thereby preventing bremsstrahlung leaving the tunnel via an open Front End.
- At the end of the run 99-3 for the first time the chromaticity was reduced in steps during the decay of the single bunch filling in USM. This resulted in an increased overall lifetime during a decay.
- There are studies going on entirely NEG coated aluminium vacuum chambers. They are aimed to produce small gap Insertion Device vacuum vessels with shorter time required for vacuum conditioning and better conductivity than stainless steel.

6.2 General scraper strategy

The general strategy for scrapers is to close several scraper jaws until all electrons with high betatron amplitudes are lost on them. The number of scraper jaws to be used and the value to which they are closed depends largely on the kind of loss mechanism:

In the case of an increase of the betatron oscillation amplitude that is significantly slower than the revolution time, it is sufficient to use one scraper jaw per plane anywhere in the machine. The transverse acceptance needs to be slightly reduced below the vacuum chamber defined acceptance. In this scenario, however, there is a high probability that the electrons escape the scraper without a lot of energy loss due to the grazing incident scattering on the scraper jaw. It might be necessary in this case to place another scraper jaw downstream to collect such electrons.
Large angle scattering processes lead to electron losses at 90 degrees phase advance downstream the scattering point. One needs therefore scraper jaws at that location. If the machine has, however, a high betatron tune and distributed scattering points (for example elastic gas scattering) this will lead to a large amount of scraper jaws. In that case it might be more useful to foresee scrapers at optimum phase advance upstream the most critical points.
If the source point is well localised (for example injection zone) the best solution is to completely scrap the phase space at large amplitudes at a location shortly downstream from the source point. This, however, requires several scraper jaws distributed at different phases.

The more the scrapers are closed, the less is the probability of electrons to hit the low aperture vessel. On the other hand the reduction of the transverse acceptance will enlarge the total amount of electron losses: During injection the injection efficiency might suffer and during the stable stored beam the lifetime will be reduced due to the reduction of the transverse acceptance. **The optimum closure is found when a rather complete collection of the electrons on the scraper jaws takes place**

without increasing significantly the total amount of losses. How this is achieved at the ESRF will be explained at the end of the chapter.

6.2.1 ESRF scraper use

The scrapers are being used systematically since June 1996 to reduce the losses on the small gap insertion device vessels. The procedure is to close each scraper jaw until the lifetime is reduced by one hour in nominal working conditions. Then they are always kept at this level during USM. **This proved to be fully sufficient to suppress the losses on the 11 mm inner aperture vessels even with the optics still using high vertical beta functions in the high beta straight sections.** The beam loss reduction on the 8 mm vacuum chambers in the recent situation can be seen in the following figure:

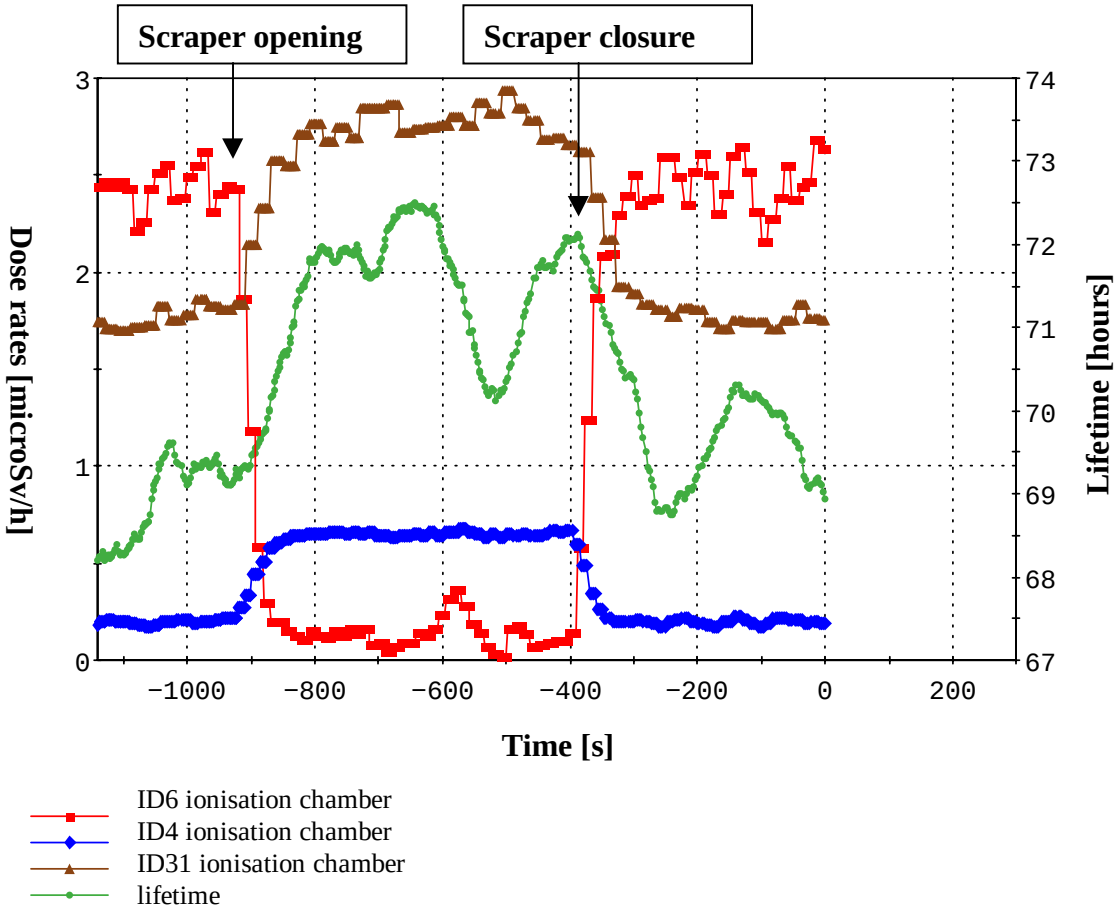

Figure 6-1 Effect of scraper closure on the lifetime and the beam losses in USM

The lifetime and the dose rates in cell 4, cell6 and cell 31 are shown over a time period over 20 minutes. The measurement was taken in the now standard operation mode of 2 x 1/3-filling. The action consisted in the opening of all scraper jaws and a switch back to operation values after 8.5 minutes. The action can at best be seen on the ID6 dose rate. As soon as the scrapers are opened the dose rate falls to a very low value and rises immediately when the scrapers are closed again. Due to the opening of the scraper the lifetime increases from 70 hours to 72 hours. One can also see that the losses on the septum sheet in cell 4 are reduced by more than a factor 2 by the scrapers

whereas the ID31 losses are only reduced by about one third**. This measurement proves that scrapers can be used to concentrate losses at less critical positions without affecting significantly the lifetime.**

An additional scraper use was implemented later which consists in closing each scraper jaw to the limit of an injection efficiency reduction at injection. The storage ring injection application is now managing to systematically switch the scraper positions from delivery values to injection values during injection and the opposite when passing to delivery. The effectiveness of scraper closure during injection is demonstrated in the following figure:

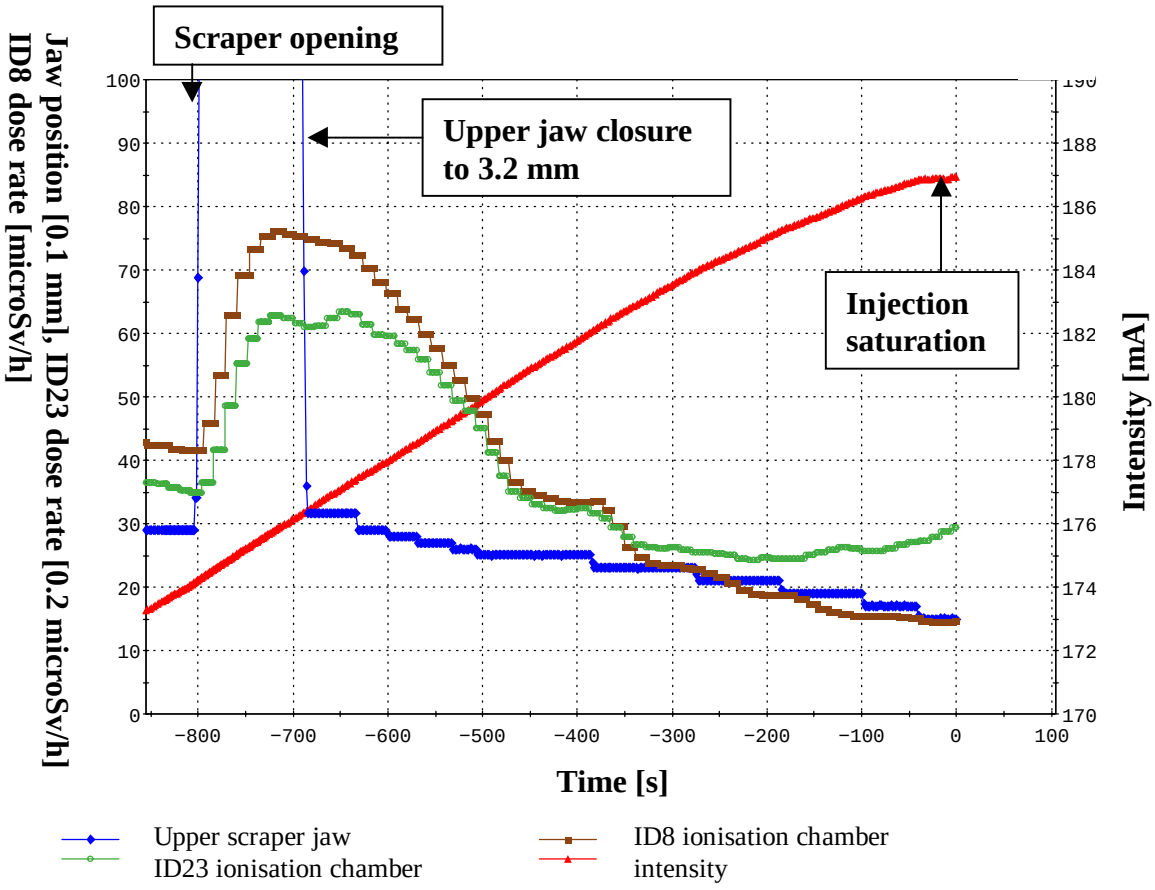

Figure 6-2 Effect of scraper closure on beam losses during injection

The measurement was performed during injection with a very small current in the booster. The injection rate was therefore about 1 mA per minute. On the graph one can see in addition the position of the upper scraper jaw as well as the ionisation chamber readings in ID8 and ID23. The measurement started with the scraper values at delivery settings. The dose rate in ID8 was about 42 µSv/h and 7 µSv/h on ID23.
Then all scraper jaws were opened. One can see the dose rates increase by close to a factor 2 following this action.
After that only the upper scraper jaw was closed. The first step was down to 3.1 mm and the last step was down to 1.5 mm. One can see the injection rate to be dropping from scraper jaw values below 2.5 mm. At 1.5 mm the injection stopped. **During the**

scraper jaw closure the losses on ID8 decreased until the end therefore proving the successful interception by the scraper jaw therefore proving the scraper protection. On ID23, however, the dose rate reached a minimum at 2.1 mm and then started to grow again. The explanation for this is the secondary scattering of the electrons intercepted on the upper jaw. **This proves the importance of secondary scattering on scraper jaws at the ESRF.**

6.3 Scraper solutions for different loss mechanisms

6.3.1 Losses with slowly increasing betatron amplitude

As already mentioned the first step is to insert a scraper jaw somewhere in the machine to slightly reduce the transverse acceptance. In the normalised phase space this will create the following figure:

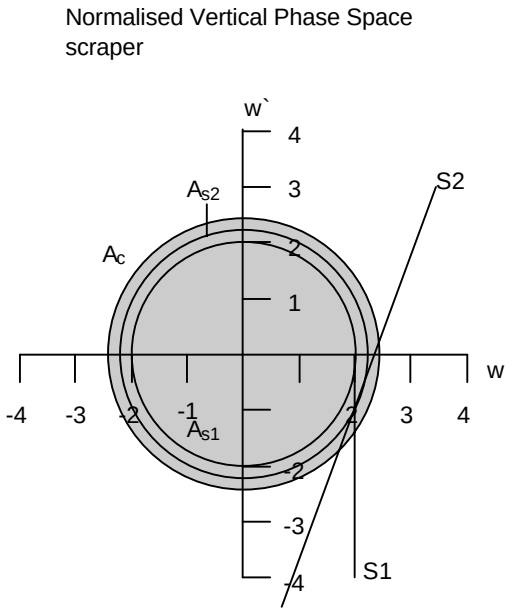

Figure 6-3 scraper protection against losses following slow betatron amplitude increase

The phase space is drawn at the location of the phase space limiting scraper with w = 2. The scraper is reducing the normalised phase space from the vacuum chambers A_c to the phase space A_{s1}. In the case of the vertical plane the figure represents a scraper jaw above the beam axis. The electrons will reach the scraper jaw and be intercepted by it. Due to the grazing incident configuration
the deflection from the multiple scattering will lead to some electrons escaping the scraper jaw without significant energy loss. Only electrons that are bend downwards can leave the scraper jaw. Since the position change is negligible they are distributed in phase space along the line S1.
It is very likely that the electrons with large angles will be lost on one of the small aperture insertion device vessels once having left the scraper.

To prevent from this a second scraper (S2) can be placed downstream. In this case a phase advance of 20 degrees is shown and the line S2 represents the scraper jaw. To be efficient the scraper S2 jaw closure should be close to the scraper S1 jaw closure. Care must be taken not to close the scraper jaw below the S1 value, as this would convert it to the main limitation and thereby rendering the arrangement useless.
There is some margin in the definition of the optimum position and closure. However, as the locations for installation are usually rather limited the choice is fairly restricted.
A complication arises from the fact that the electrons escaping the scraper jaw generally have a different angle in the other plane with no limitation in one direction. To intercept these electrons one can adapt the solution developed in the next section.

6.3.2 Scattering leading to large angles

The best way to cope with losses created by large angle scattering (for example elastic gas scattering) is to intercept the electrons when the large angle is transferred into a large position i.e. 90 degrees phase advance downstream the scattering point. The following figure shows the situation in the normalised phase space.

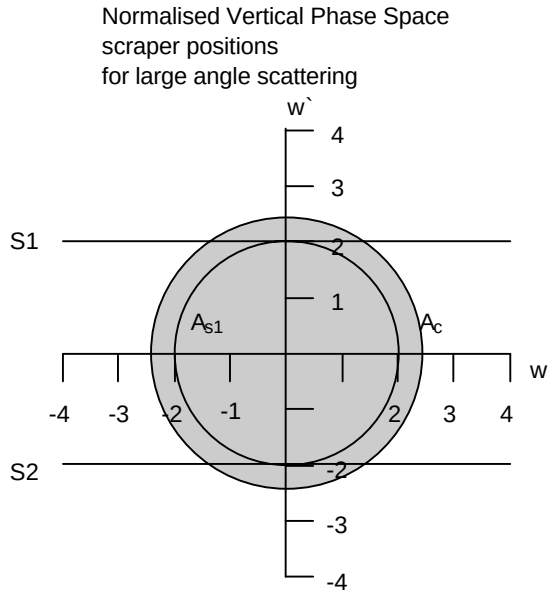

Figure 6-4 Scraper protections against large angle scattering losses

The phase space is drawn at the point of scattering. The scattering process itself will distribute the electrons along the w' axis since the position of the electron can not change instantaneously. In order to intercept the electrons with positive angles as well as those with negative angles two opposite scraper jaws S1 and S2 have to be placed 90 degrees downstream in phase.
Grazing incident scattering on the scraper jaws is very unlikely since the electrons receive the full angle in one event. Therefore no additional scraper jaws are needed to suppress secondary losses.

The scattering points are, however, in most of the cases distributed all around the ring. To obtain an efficient protection in this logic one should install about one scraper jaw

pair per 90 degrees phase advance. For the ESRF vertical tune of 11.39 or 14.39 this would result in about 100 scraper jaws which is impossible to install. This strategy is therefore not a useful approach for a high focusing machine.

In the case of a few small gap vacuum chamber vessels, the most logical approach is to intercept the electrons just upstream the small gap vessel without paying attention to where the scattering took place.
The obvious approach would be to install a scraper at the entrance of the straight section. In the case of a high beta function in the straight section this would work since the phase advance along the straight section is very small. The main problem in this case is to ensure that the electron loss on the scraper does not cause the same radiation problems around the beam line as the loss on the insertion device vacuum vessel – a problem that is not negligible.
In the case of a low beta straight section the situation is more complicated. The large phase advance along the straight section renders a single scraper at the entrance insufficient. A solution is shown in the following figure, again, using the normalised phase space.

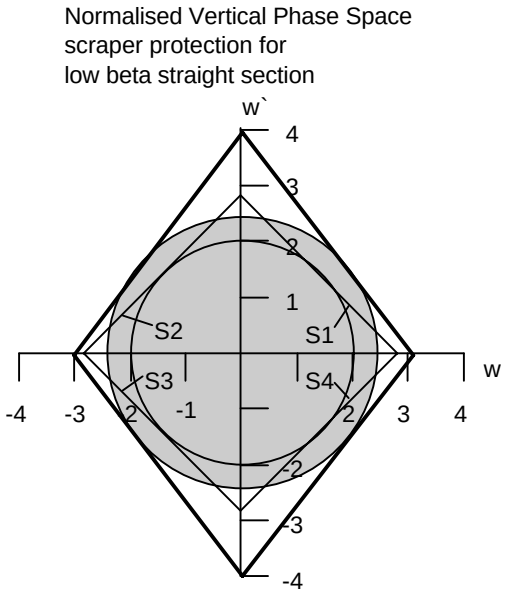

Figure 6-5 scraper protection for a vacuum chamber in a low beta straight section

The four scraper jaws S1, S2, S3 and S4 are positioned so that they suppress all losses on the vacuum vessel (represented by the outer frame). The optimum position for the jaws is approximately 90 degrees phase advance between each jaw. This can be reached with two pairs of opposite scraper jaws at two locations with a phase difference of 90 degrees. An additional constraint comes from the fact that the scraper jaws must have a phase difference to the vacuum chamber entrance of a multiple of 90 degrees. One solution would be to place one pair of scraper jaws just upstream the vessel and another pair about 90 degrees phase advance upstream.

For a given machine the question is if a distributed scraper solution is preferred with respect to specific protection of the small gap vacuum chambers. One must consider

the optics, the amount of small aperture vessels and the beam loss suppression factor required. The specific protection of the small gap vacuum chambers might be considered if their number remains small. At the ESRF this is, however, very unlikely for the 8 mm inner vertical aperture vessels since several 11 mm inner vertical aperture vessels are supposed to be replaced by them.
Fortunately the vertical elastic gas scattering losses only represent a small fraction of the beam losses at the ESRF and the losses are distributed. Therefore the ESRF can safely operate without protection against elastic gas scattering losses. For machines with a small elastic gas scattering lifetime and only few small gap Insertion Device vacuum chambers scraper protection should be considered.

6.3.3 Transverse injection losses

Injection losses coming from transverse mismatching of the injected beam with respect to stored beam conditions can be efficiently intercepted with scrapers. This can be done since the septum is the only source point. During injection the lifetime does not need to be considered, therefore the scraper jaws can be positioned much closer to the beam axis. The best way to intercept the injected electrons is to position a number of scraper jaws with the correct phase advance slightly downstream the injection point. One example is given in the following figure.

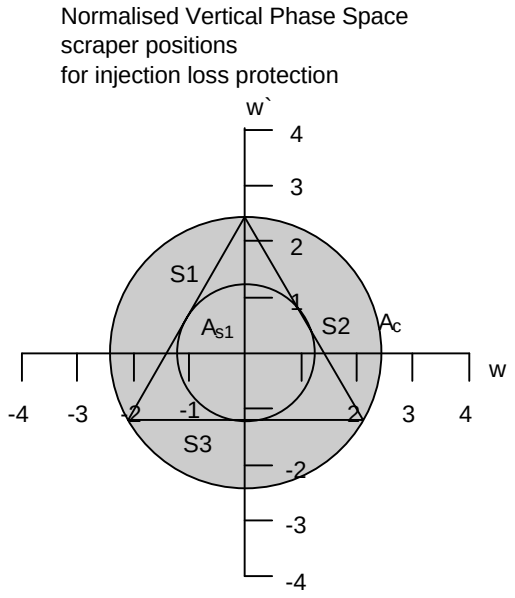

Figure 6-6 scraper protection for transverse injection losses

Scrapers S1, S2 and S3 are positioned at a 120 degrees phase advance closed to half of the aperture of the vacuum vessels A_c. The acceptance for the injected beam is then reduced to A_{s1}. This is a severe reduction that might reduce the injection efficiency.

Less acceptance reduction can be achieved by using more scraper jaws. One can calculate the acceptance A_{s1} as a function of the initial acceptance A_c and the number n of scraper jaws used. The basic relations can be derived from Figure 6-7. It shows the normalised phase space for the optimum four-scraper jaw assembly.

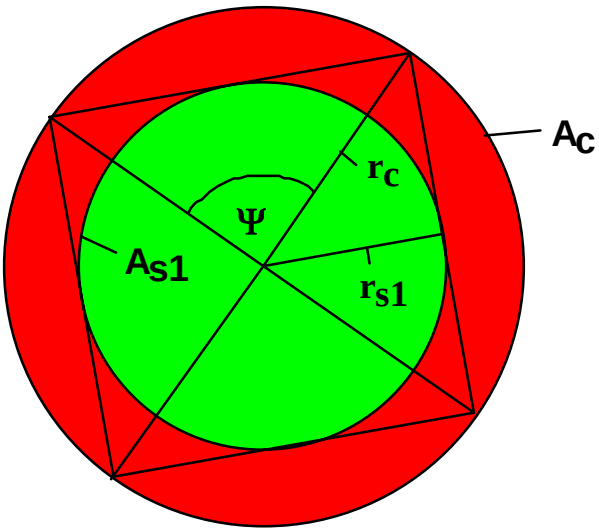

Figure 6-7 geometry of acceptance reduction due to scrapers

The following equations can be derived:

$$A_{s1} = \pi \cdot r_{s1}^2$$

$$A_c = \pi \cdot r_c^2$$

$$\cos\left(\frac{\psi}{2}\right) = \frac{r_{s1}}{r_c}$$

$$\psi = \frac{2 \cdot \pi}{n}$$

Equation 6-1 basic relations for acceptance reduction due to scraper protection

From this one can easily calculate

$$A_{s1} = \pi \cdot r_{s1}^2 = \pi \cdot r_c^2 \cdot \cos^2\left(\frac{\psi}{2}\right) = A_c \cdot \cos^2\left(\frac{\pi}{n}\right)$$

Equation 6-2 acceptance reduction as a function of number of scraper jaws used

The ratio of A_{s1} to A_c is shown in the following graph:

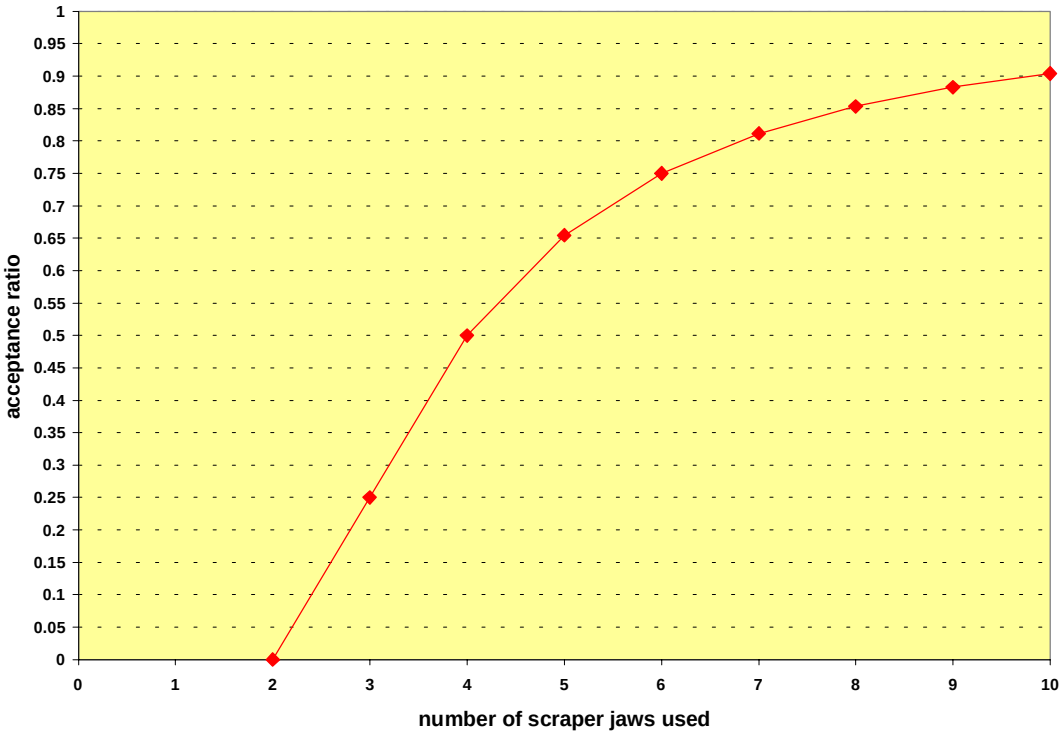

Figure 6-8 ratio of effective acceptance to initial acceptance as a function of the number of scraper jaws used

To make a choice for a real machine is not easy. One has to take into account the amount of possible scraper positions between the injection point and the vacuum vessels to protect and the acceptance required keeping the injection efficiency at a maximum. The choice becomes even more difficult if the working point of the machine is not fixed. Since the protection has to work in both planes, a full protection without reducing the injection efficiency is very difficult to achieve.

One way is to do part of the job already at the end of the transfer line. For a horizontal injection process, for example, installing small vertical apertures after the last vertical steering element in the transfer line will limit the amplitudes of the vertical mismatch. This is quite often naturally achieved by using small vertical gap septum vessels for the storage ring injection. At the ESRF there is about 5m length after the last vertical steerer with a vacuum vessel of 10 mm full inner vertical aperture. This is quite comparable to the chamber sizes of the small gap insertion device vessels.
For an optic with a high vertical beta function in the straight section the phase advance is low and the transfer line chamber therefore plays a role of a pair of opposite scraper jaws. Unfortunately at the ESRF the chamber gap of 10 mm is too large to protect sufficiently the 11 mm inner aperture vessels and the protection is even less for the 8 mm inner aperture vessels.
For an optic with a low vertical beta function in the straight section the transfer line chamber is equivalent to a frame in the phase space and probes all phase advances. It is equivalent to a four-scraper jaw protection. To have an effective protection one can calculate from Equation 6-2 the maximum aperture for the optimum phase advance of

90 degrees. An inner aperture of 7.7 mm is needed for the 11 mm inner aperture vessels and 5.7 mm is sufficient for the 8 mm inner aperture vessels.
The vertical septum vessel aperture of 10 mm also explains that no radiation problems occurred during injection with the first generation of insertion device vessels with 15 mm inner vertical aperture.

6.4 Radiation considerations and optimum scraper location

The aim of scrapers is to intercept electrons that would otherwise be lost on the small gap insertion device vessels. By using scrapers one creates localised losses which might lead to unacceptable dose rates in the scraper area. This requires an appropriate design of the scrapers including the surrounding shielding. The scrapers initially installed at the ESRF for diagnostic reasons are of copper, 20 mm in length with a surface thickness of only 5 mm. Since this is insufficient to stop the electromagnetic shower, high radiation and activation levels are measured downstream the scraper. For long-term use a new design is therefore being studied which will be optimised for radiation aspects. To stop the neutrons a reinforcement of the tunnel roof might be envisaged above the final scraper locations.

The bremsstrahlung created due to electron losses in a straight section has a large probability to enter into the open Front End of the corresponding beam line. Therefore it is advisable to not install scrapers in beam line straight sections. One should therefore preferably use other straight sections that are, for example, used for the cavities or injection. This can only be respected if one is dealing with a small amount of scrapers. The other solution is to install the scrapers in the achromat sections.

The material thickness seen by an electron hitting a scraper jaw can be smaller than the total jaw thickness. This is case if the electron is hitting the jaw at the jaw entrance close to the edge with an angle towards the beam axis. This is also true for electrons hitting the jaw surface with an angle away from the beam axis.
The effect becomes important if the most likely electron angles differ greatly from the surface angle of the scraper. Following Equation 5-15 the most likely impact angle for a given scraper jaw position is:

$$z' = -z_{scr} \cdot \frac{\alpha_z}{\beta_z}$$

Equation 6-3 most likely electron impact angle on a scraper jaw

The effect is enhanced when the scraper is positioned in a strong focusing region with a small beta function.
A typical case for this is the foreseen positioning of a horizontal scraper on a CV4 vessel at the ESRF, i.e. at the end of a straight section directly upstream from the dipole. Some number are given in the following table:

parameter	value
Horizontal beta function [m]	3
Horizontal alpha function	1.77
Typical scraper position [mm]	7
Most likely impact angle [mrad]	-4.13

Table 6-1 most likely electron impact angle on a CV4 upper jaw

The angle of 4 mrad is four times larger than the typical impact angle of the Insertion Device vacuum chambers that were given in Table 5-7. To avoid a reduction of the effective scraper thickness one can consider tapering of the scraper jaw with the average electron impact angle or specific alignment.

One can question what is the optimum beta function at the position of the scraper. A high beta function has the advantage of the possibility of keeping the scraper far from axis. This comes from the scaling of the transverse distance of the scraper to the beam axis with the square root of the beta function. Keeping the scraper far from the axis reduces the effect of mechanical positioning errors and eases the necessary tapering of the vacuum vessels upstream and downstream the scraper.

If one wants to minimise the betatron amplitude following secondary scattering one should choose, on the other hand, a location of a small vertical beta function. This is due to the fact that the betatron oscillation amplitude following an angle kick is proportional to the square root of the beta function at the location of the scattering point as it is expressed for the vertical in the following equations:

$$A = \beta(s_0) \cdot z_0'^2$$

$$z(s) = \sqrt{A \cdot \beta(s)} \cdot \cos\left(\Psi(s - s_0)\right) = z_0' \sqrt{\beta(s)\beta(s_0)} \cdot \cos\left(\Psi(s - s_0)\right)$$

Equation 6-4 betatron oscillation amplitude following an angular kick

Since the electron might receive an angle in both planes both beta functions have to be considered. If a good protection for secondary scattering effect is given or if incident scattering on the scraper jaw is very unlikely, a position with a large beta function is the optimum choice.

6.5 General scraper solution and specification for the ESRF

6.5.1 General solution

On real machines one cannot treat each beam loss mechanism separately. Scrapers should be used for many purposes. A solution is shown in the following figure:

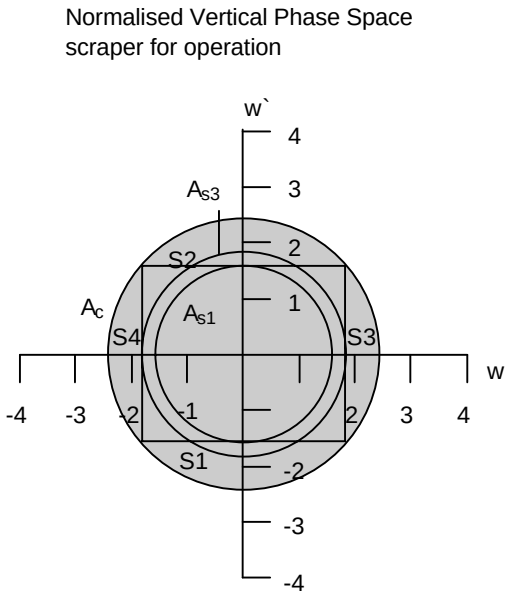

Figure 6-9 General scraper solution

A pair of opposite scraper jaws S1 and S2 is placed slightly downstream the septum with an opening of 65 % of the total aperture. A second pair of scraper jaws S3 and S4 is placed 90 degrees downstream in phase with an opening of 75 % of the total aperture.

In this configuration the phase space is well shielded against for example transverse injection losses. Additionally electrons with slow rising betatron amplitude will fall on S1 or S2 with secondary scattering protection by S3 and S4. The aperture reduction down to 65 % is only slightly smaller than 70.7 % percent of optimum value with four jaws. Several combinations of the S1(S2) aperture p_1 and the S3(S4) aperture p_2 can be chosen as long as one respects the following conditions:

- $p_1 < p_2$ to intercept the electrons on S1 or S2
- $p_1^2 + p_2^2 \leq d^2$ to fully protect the vacuum chamber

with d as half aperture of the minimum gap vacuum vessel.

The proposed solution requires four scraper jaws per plane, however, in the vertical plane two scraper jaws might be replaced by an aperture reduction at the end of the transfer line. It should also be mentioned that in the horizontal plane the septum might be used as the aperture limiting point or as replacement of a scraper jaw. In this case it is, however, useful to have the possibility of displacing it as it is the case at the ESRF, where the septum position can be changed remotely.

Following Equation 6-4 treating the secondary scattering at optimum would require the first scraper jaws to be placed at a location with small beta functions (at best in the middle of a low beta straight section without beam line use). A second pair of scrapers in each plane should follow at 90 degrees downstream at a high beta location.

6.5.2 Optimum scraper scenario for the ESRF

When trying to develop scraper protection scenarios for the ESRF for the recent situation one must first take into account the transverse phase advances between the different locations where scrapers could be implemented. This is done in the following table where the fraction of betatron oscillations with respect to the middle of a high beta straight section is given. The values are given in fractions of 360 degree for two cells, which represents one superperiod.

location	Horizontal phase	Hor. phase difference between two points	Vertical phase	Ver. phase difference
Middle high beta straight	0		0	
Before first dipole	0.054	0.054	0.189	0.189
Before second dipole	0.505	0.452	0.244	0.055
Middle low beta straight	1.139	0.634	0.450	0.205
Before first dipole	1.393	0.255	0.639	0.190
Before second dipole	1.858	0.465	0.694	0.055
Middle high beta straight	2.278	0.420	0.899	0.205

Table 6-2 Phase advances in the low vertical beta optic

Looking to Table 6-2 two solutions could be found for the ESRF:
- A four jaw scraper in the middle of ID5
one internal and one external jaw just upstream the first dipole of cell 5
one upper and one lower jaw just upstream the second dipole of cell 5
The advantages are the full interception of injection losses before cell 6, the positioning of the four jaw scraper at a location of small beta functions and the scraper installation in a straight section without beam line use (cavities 1 and 2).
The great disadvantage is that the cavities have to be moved to gain space between them.

– An upper and lower jaw scraper in the middle of the ID4 straight section
- An upper and lower jaw at the end of the transfer line from the booster to the storage ring
An upper and lower jaw just upstream the second dipole of cell 4
An internal and external jaw scraper at the exit of the ID4 straight section

An internal and external jaw scraper at the entrance of the ID6 straight section

The advantage would be the installation of the first vertical jaws at a location of a small vertical beta function, the interception of the injected electrons until the ID6 straight section and the installation of the first scraper jaws at locations without beam line use.

The disadvantages would be the scraper installation in a straight section with a beam line (ID6) and the positioning of the first horizontal scraper within the kicker bump. Scrapers within the kicker bump would give an additional diagnostic during injection but would render the horizontal protection less efficient during injection.

A decision of the final scraper positioning was not yet taken since the scraper design and its surrounding shielding have first to be assessed.

7. Conclusion and Outlook

7.1 Conclusion

The constant pursuit for higher brilliance of third generation light sources has led to a continuous reduction of the vertical gap of insertion devices. This resulted in both the development of in-vacuum undulators (Spring 8 approach) or straight section vacuum vessels of small vertical size (BESSY 2 and APS approach). The ESRF, as one of the first third generation light sources, started with Insertion Device vacuum chambers with a safe inner vertical aperture of 15 mm. This aperture was then reduced first to 11 mm and later on to 8 mm. During the same period important modifications of the machine optic, of the RF system and of the machine tuning for the different filling patterns took place. A part of this work was driven by the results of beam loss studies.

When the first 11mm aperture chambers were installed in high beta straight sections radiation problems arose on the corresponding beam lines and tunnel roof position. It was rapidly understood that the problem was coming from electron losses on the insertion device vacuum chambers. The radiation problem on the beam lines is only existing during USM with the Front End of the beam line open. High radiation doses on the tunnel roof are, on the other hand, mainly accumulated during injection and MDT – times during which the Front Ends are closed.

A quantitative analysis of the different beam loss origins was carried out. The total beam losses due to equipment failures and the Touschek scattering were identified to be the major contributions to the losses in USM. The limitations of the Touschek lifetime were discussed. The reduction of the total amount of Touschek losses following the machine development was shown. It was also explained that large vertical chromaticities lead to vertical betatron oscillations following Touschek scattering and inelastic gas scattering.
The main action to reduce the integrated dose rates on the tunnel roof was to limit the amount of electrons per 4-hour period available for injection. This reduced significantly the losses in MDT during injection intensive studies.

The link between the different beam loss origins and the final collision point with the vacuum chamber was established. The optimum beta function in the middle of the straight section was proved to be half of the length of the straight section. It was also shown that large beta functions tend to distribute the losses between the different vacuum chambers. It was explained why in a high beta straight section the electrons collide only at the entrance of the straight section vessel whereas in the low beta case also losses at the exit of the straight section take place. An overview of the most likely collision points for the different beam loss origins was developed.

The interaction of electrons in matter was investigated to establish the link between the electron losses and the dose rates measured outside the tunnel. The heating up of a scraper to its melting point following a full beam loss was calculated for the ESRF example. The large probability of electrons escaping the chamber material following incident scattering

was highlighted. The origin of the vacuum chamber activation and its behaviour with time was analysed. Different beam loss detection systems at the ESRF were installed and used to validate the predictions from the beam loss model.

Together with a variety of actions to reduce the total amount of losses one major point was the use of scrapers to intercept the electrons. Permanently used in USM and during injection they proved to suppress all losses on the 11 mm vacuum chambers. Their beneficial effect for the 8 mm vessels was also shown. General solutions were developed for the different kind of beam losses. The acceptance reduction as the function of the number of scraper jaws was shown. Finally the optimum scraper solution for the ESRF was worked out.

To summarise one can say that most of the beam loss mechanisms were understood and quantified. Reliable beam loss detection systems were made operational and the existing beam loss protection using scrapers is being upgraded to an even higher degree of efficiency. The work resulted in the complete suppression of losses on the 11 mm inner vertical aperture vessels. The losses on the 8 mm inner aperture vessels are kept on an acceptable level. This was confirmed by several independent measurements. The ESRF is ready to respect the reduced dose rates for the Experimental Hall that will become valid in the year 2000.

The ESRF's experience with beam losses has been used for the design of new synchrotron light sources. For example, optimising the vertical beta functions in the straight sections was done for APS and for the SOLEIL design. Another example is the specific shielding of the tapering of the APS insertion device vessels downstream the injection. For the SOLEIL project a distributed solution of scrapers has been foreseen. Moreover, the APS beam line shielding was greatly reinforced with respect to the initial ESRF design.

7.2 Outlook

Recently the future of ring based synchrotron light sources was discussed at the ICFA Workshop for Future Light Sources in Argonne, USA[52]. As an example for future light source the following possible scenario was developed by the working group on ring based sources:

- a machine of 1.5 to 2 km length
- an electron energy of 3 GeV
- vertical and horizontal emittance in the range of 50 pm
- the extensive use of damping wigglers
- more than 1 A beam current
- use of in-vacuum undulators at 5 mm gap to achieve undulator radiation up to 20 keV

Especially the use of in-vacuum undulators or small gap vacuum chambers is common to all new projects and upgrades of existing light sources. Therefore sooner or later all machines will be confronted to electron losses on these devices[73]. This will be reinforced by the fact that the large electron densities for future light sources will enhance the

Touschek scattering. The ESRF studies significantly contributed and still contribute to this field. At the ESRF the ongoing upgrade of the scraper based protection and the exploration of the potential of the in-vacuum undulator technology will further push the limits of what can be achieved as minimum Insertion Device gap in routine operation.

Low energy studies are also performed at the ESRF in order to explore the low emittance limits. Some of the scaling laws were already discussed in this respect. Beam loss and radiation measurements in these conditions will allow extrapolating the problems encountered at 6 GeV to lower energies.

Another tendency on modern ring based light sources is to permanently top up the storage ring intensity to overcome the Touschek lifetime limitation. This mode of operation requires injecting while the Front Ends are open. This is therefore a beam loss and radiation protection issue and will be considered for future light sources also.

The best way to avoid radiation problems outside the tunnel is to implement the proper shielding. It is very difficult to avoid bremsstrahlung from electron losses or inelastic gas scattering to penetrate through an open Front End into an optics hutch. Consequently optic hutches should not only be radiation shielded against synchrotron radiation but also against bremsstrahlung. This is easier to achieve and more acceptable to a beam line than trying to separate the bremsstrahlung from the synchrotron radiation inside the tunnel with an optical arrangement[74]. With an appropriate concrete shielding around the optic hutches future synchrotron light sources would be able to accept higher vacuum pressure within straight sections as well as electron losses on small vertical aperture vessels without radiation problems. This would also allow a topping up operation of the storage ring without complicated safety procedures.

Acknowledgements

This thesis work was carried out at the ESRF taking profit from the machine performance, diagnostic and availability. First of all I want therefore to thank everybody who contributed or still contributes to this. It is impossible to list all the help I got in performing the work but I would like to express some particular thanks.

First of all I want to thank Prof. Dr. Klaus Wille for the thesis supervision at the University of Dortmund. His explanations why this work is important to the whole synchrotron radiation accelerator community helped me to develop a general view beyond the ESRF needs.

Many thanks to Dr. Jean-Marc Filhol who as my ESRF supervisor assured all the necessary tools for the thesis work to be rapidly made operational. It is mainly due to him that the acquired knowledge during the studies was transferred into operation changes on the machine. The fruitful discussion with him and his advice were essential to develop the understanding of the matter.

I would like to express my gratitude to Dr. Thomas Günzel for several simulations for the thesis and many helpful discussions on the subject.

Many thanks to the diagnostic group and especially Dr. Graham Naylor and Benoit Joly for the installation, maintenance and upgrade of the beam loss detector system as well as for their participation in the analysis of the beam loss detector signals.

The different kinds of radiation measurements Dr. Paul Berkvens and Patrick Colomp performed during the time of the thesis were necessary to direct the studies in the good direction. Their knowledge was essential for the upgrade of the beam loss detection system and the scrapers. Additionally they set up the ionisation chamber system and the neutron detection system as well as the limitation of the integrated intensity in TL2.

I am very pleased to be a member of the operation group – especially due to the excellent human relations within the group. The group members sustained the fact that due to the thesis work I could attribute less time to the other group responsibilities. I am particularly thankful to Laurent Hardy who took many extra work load in this respect.

I want to thank Dr. Jörn Jacob, Dr. Laurent Farvacque, Dr. Ryutaro Nagaoka, Dr. Jean-Luc Revol and Dr. Annick Ropert for a lot of help in understanding the physics behind the problems and the reviewing of a draft of this document. They have also played a major role in the machine improvements during the last years.

I also want to thank Karen Clugnet for the English correction of the thesis.

Many thanks to Dr. Jean-Louis Laclare who gave me the responsibility for this subject and to Prof. Dr. Gottfried Mülhaupt who had the idea of making a thesis out of this.

[1] *Protection against beam losses*, chapter 9 of the Design study of the Large Hadron Collider (LHC),CERN91-03
[2] K.Wille , *private communication concerning the use of a superconducting wiggler at DELTA*, August 1997
[3] M.W.Poole , *Effect of Small ID Gaps*, Presentation to the 4 th Annual Workshop of European Synchrotron Light Sources, November 1996
[4] L. Farvacque, J.L. Laclare, C. Limborg, A. Ropert, *The Low Emittance Lattice*, ESRF Newsletter, June 95
[5] U. Weinrich, *Optimum vertical beta function in the straight sections with respect to the vertical elastic gas scattering lifetime*, ESRF technical note 5-96/Theory, May 96
[6] A. Ropert, *The low β_z optic*, ESRF technical note 3-97/Theory, March 97
[7] K. Wille, *Bewegungsgleichung im Wiggler oder Undulator*, chapter 8.2, Physik der Teilchenbeschleuniger und Synchrotronstrahlungsquellen, Teubner Studienbücher
[8] K. Wille, *Undulatorstrahlung*, chapter 8.3, Physik der Teilchenbeschleuniger und Synchrotronstrahlungsquellen, Teubner Studienbücher
[9] *ESRF Foundation Phase Report*, February 1987
[10] R.Walker, *Undulators and Wigglers*, CERN Accelerator school on Synchrotron Radiation and Free Electron Lasers, Grenoble, April 1996
[11] J.Bahrdt, *Conclusion of working group 4*, ICFA workshop on future light sources, Argonne, April 1999
[12] M.W. Poole, Introduc*tion of the work shop*, workshop on Realisation of Small Gap Insertion Devices in third generation light sources, Daresbury, Mai 1999
[13] K. Wille, *Transformation der Betafunktion durch die Magnetstruktur*, chapter 3.10, Physik der Teilchenbeschleuniger und Synchrotronstrahlungsquellen, Teubner Studienbücher
[14] U. Weinrich, *Aperture limitation due to injection*, ICFA workshop on 4th generation light sources, Grenoble, January 1996
[15] U. Weinrich, *Injection bump closure and general optimisation*, ESRF technical report 76-96/MDT
[16] L. Farvacque, A. Ropert, *Storage Ring Injection Parameters*, ESRF internal report, November 1988
[17] http;//www.esrf.fr/machine/myweb/MODES.html, ESRF web pages on operation modes
[18] J. Jacob et al., *Experimental and Theoretical Studies of the Transverse Single Bunch Instabilities at the ESRF*, Presentation to the EPAC98, Stockholm, June 1998
[19] C. David et al., *Construction of a third RF Acceleration Unit for the ESRF Storage Ring*, Presentation to the EPAC 96, Sitges, June 1996
[20] G. Besnier et al., *Experimental and Theoretical Studies of Transverse Single Bunch Instabilities*, Presentation to the EPAC 98, Stockholm, June1998
[21] J. Jacob, O. Naumann, *Landau Damping of Longitudinal Instabilities for the Operation of the ESRF Storage Ring*, EPAC 98, June 98
[22] K. Wille, p. 201, Physik der Teilchenbeschleuniger und Synchrotronstrahlungsquellen, Teubner Studienbücher
[23] H. Wiedemann, *Longitudinal particle motion*, Chapter 8.1, Particle Accelerator Physics, Springer Verlag
[24] H. Wiedemann, *Collective Phenomena*, Chapter 12, Particle Accelerator Physics, Springer Verlag

[25] P. Berkvens et al., *Radiation Safety around the ESRF beamlines*, Presentation to the EPAC 96, Sitges, June 1996
[26] P.Berkvens, F. Bidault, *The ESRF Beamline Personnel Safety System*, Presentation to the EPAC 96, Sitges, June 1996
[27] *Council Directive 96/29/EURATOM*, 13/05/96
[28] P. Colomp, *Application de la directive Euratom 96/29 a l'ESRF*, Memoire presented to the Centre Regional Associe de Montpellier de la CNAM, May 1999
[29] P.K.Job, H.J.Moe, *Dose Rate Estimates in the First Optical Enclosure due to Particle Beam Loss in the Insertion Device Transition Region during Injection*, APS LS Note 243, May 1995

[30] J.A.Clarke, H.L.Owen, *Operation of the Daresbury Synchrotron Radiation Source with reduced vertical aperture*, Poster Presentation at the EPAC96
[31] L.Farvacque, U.Weinrich, *Beam Stay Clear*, Presentation to the workshop on beam stay clear, magnet aperture and options for the vacuum system of SOLEIL, Orsay, November 1996
[32] U.Weinrich, *Aperture limitation due to injection*, Presentation to the 10th ICFA Beam Dynamics Panel Workshop on 4th Generation Light Sources, January 1996
[33] G.Chazot, U.Weinrich, *Injection optimisation for the low betaz lattice*, ESRF technical note 61-96/MDT, October 1996
[34] U.Weinrich, *Vertical aspects of the storage ring injection*, ESRF technical note 3-96/MDT, January 96
[35] G.Chazot, U.Weinrich, *Injection optimisation for the low betaz lattice*, ESRF technical note 61-96/MDT, October 1996
[36] H.Wiedemann, *Charged Particle Acceleration*, chapter 8 of Particle Accelerator Physics, 1993
[37] K.Wille, *Phasenstabiler Bereich*, chapter 5.7, Physik der Teilchenbeschleuniger und Synchrotronstrahlungsquellen, Teubner Studienbücher
[38] I.Fladmark, U.Weinrich, *Injection studies for the new scraper settings*, ESRF technical note 43-96/MDT, July 1996
[39] B.Ledrappier, U.Weinrich, *Injection optimisation and scraper settings for the low betaz lattice*, ESRF technical note 72-96/MDT, November 1996.
[40] Helmut Wiedemann , *Beam Life Time*, chapter 11 of Particle Accelerator Physics, 1993
[41] A.Wrulich, *Single-beam lifetime*, CERN Accelerator School 94-01
[42] L.Farvacque, *Beam Life-Time*, ESRF technical note
[43] H.M.Bizek, *The extended touschek lifetime*, Presentation at PAC97
[44] A.Nadji, G.Flynn, J.L.Laclare, M.P.Level, P.Nghiem, J.Payet, *Energy Acceptance and Touschek Lifetime Calculations for the SOLEIL Project*, Presentation at PAC97
[45] A.Streun, *Momentum Acceptance Optimisation at SLS*, Presentation at the 4th Annual Workshop on European Synchrotron Radiation Light Sources in Trieste, November 1996
[46] H.Burkhardt, *Monte Carlo Simulation of Scattering of Beam Particles and Thermal Photons*, CERN SL Note 93-73, July 1993.
[47] I.Fladmark, J.M.Koch, P.Roussely, U.Weinrich, *SR injection and lifetime studies followed by USM preparation*, ESRF technical note 26-96/MDT
[48] A.Ropert, *Lifetime Studies and Modelling*, ESRF technical note 08-97/MDT, February 1997
[49] D. Schmied, private communication
[50] H.W. Koch and J.W.Motz, *Bremsstrahlung Cross-Section Formulas and Related Data*, Review of Modern Physics, Volume 31, Number 4
[51] R. Nagaoka, *Coupling Corrections on the basis of Response Matrix Modelling*, Presentation to the 1999 ESRF Machine Related Activities Report, Sassenage, February 1999
[52] V. Litvinenko, *Ring Based Sources Overview*, Plenary talk to the ICFA Workshop on Future Light Sources, Argonne, April 1999
[53] M.Zisman, S.Chattopadhyay, J.J.Bisognano, *ZAP USER'S MANUA*L, Lawrence Berkeley Laboratory, December 1986
[54] J.L.Laclare, A.Ropert, U.Weinrich, *ESRF Approach to Fourth Generation Light Sources*, Presentation to the Workshop on 4th Generation Light Sources in Grenoble, January 1996

[55] Helmut Wiedemann, *Momentum Acceptance*, chapter 8.2 of Particle Accelerator Physics, 1993
[56] O.Naumann, J.Jacob, *Fractional Filling Induced Landau Damping of Longitudinal Instabilites at the ESRF*, Presentation to the PAC97, May 97
[57] T. Günzel, *Estimation of the impedance of ID-chambers*, ESRF internal technical note 9-97/Theory
[58] U. Weinrich, *Beam Loss Measurements for different sextupole tunings*, ESRF internal report 27-99/MDT, June 1999
[59] P. Kernel, Private communication
[60] A. Ropert, *Lifetime Issues for Third Generation Light Sources*, Presentation to EPAC98, Stockholm, June 1998

[61] Agreement in the Beam Physics Workgroup, Workshop on Realising Small Gap Insertion Devices in 3rd Generation Light Sources, Daresbury, May 1999
[62] *GEANT3 - Detector Description and Simulation Tool*, CERN Program Library Long Writeup W5013, Geneva, 1994
[63] B.Keil, *Bau und Test eines Strahlverlustmonitor-Systems für Elektronenspeicherringe*, chapter 3.2, Diploma thesis, Dortmund, March 1996
[64] R.K.Bock, A.Vasilescu, *The Particle Detector BriefBook*, Springer Verlag
[65] P.J.Gollon, *Production of Radioactivity by particle accelerators*, IEEE Transactions on Nuclear Science, Vol.NS-23, No.4, August 1976
[66] P.Berkvens, *Power deposit in a tantalum target*, ESRF internal memo, May 1999
[67] T.Günzel, U.Weinrich, *Effect of the Scraper on Beam Electrons in Head-on Collisions*, ESRF technical note 7-96/Theory, June 1996
[68] T.Günzel, *Behaviour of the Beam in Incident Collisions with the Scraper*, ESRF technical note 10-96/Theory, July 1996.
[69] B. Joly, G. Naylor, U. Weinrich, *Beam Loss Monitors at the ESRF*, presentation to the DIPAC 99, Daresbury
[70] P.Berkvens, P.Colomp, *New Radiation Monitoring System for the ESRF*, EPAC 98, p.2295
[71] User's Manual, model REMbrandt AP 2001, Apfel Enterprises, New Haven, USA
[72] P. Berkvens, *Machine related safety*, presentation to the 1997 annual workshop on machine related activities, Sassenage, 27th January 1997
[73] A. Wrulich, Future directions in the storage ring development for Light Sources, chapter2.2, presentation to the PAC99, New York, March 1999
[74] Summary of an ESRF internal meeting on future machine developments, September 1999